

NORTHWESTERN UNIVERSITY

Synthetic Elucidation of Design Principles for Molecular Qubits

A DISSERTATION

SUBMITTED TO THE GRADUATE SCHOOL
IN PARTIAL FULFILLMENT OF THE REQUIREMENTS

for the degree

DOCTOR OF PHILOSOPHY

Field of Chemistry

By

Michael James Graham

EVANSTON, ILLINOIS

September 2017

© Copyright by Michael James Graham 2017, except where otherwise noted.

All Rights Reserved

ABSTRACT

Synthetic Elucidation of Design Principles for Molecular Qubits

Michael James Graham

Quantum information processing (QIP) is an emerging computational paradigm with the potential to enable a vast increase in computational power, fundamentally transforming fields from structural biology to finance. QIP employs qubits, or quantum bits, as its fundamental units of information, which can exist in not just the classical states of 0 or 1, but in a superposition of the two. In order to successfully perform QIP, this superposition state must be sufficiently long-lived.

One promising paradigm for the implementation of QIP involves employing unpaired electrons in coordination complexes as qubits. This architecture is highly tunable and scalable, however coordination complexes frequently suffer from short superposition lifetimes, or T_2 . In order to capitalize on the promise of molecular qubits, it is necessary to develop a set of design principles that allow the rational synthesis of complexes with sufficiently long values of T_2 .

In this dissertation, I report efforts to use the synthesis of series of complexes to elucidate design principles for molecular qubits. Chapter 1 details previous work by our group and others in the field. Chapter 2 details the first efforts of our group to determine the impact of varying spin and spin-orbit coupling on T_2 . Chapter 3 examines the effect of removing nuclear spins on coherence time, and reports a series of vanadyl bis(dithiolene) complexes which exhibit extremely long coherence lifetimes, in excess of the 100 μs threshold for qubit viability. Chapters 4 and 5 form two complimentary halves of a study to determine the exact relationship between electronic spin–nuclear spin distance and the effect of the nuclear spins on T_2 . Finally, chapter 6 suggests next directions for the field as a whole, including the potential for work in this field to impact the

development of other technologies as diverse as quantum sensors and magnetic resonance imaging contrast agents.

ACKNOWLEDGEMENTS

Writing an acknowledgements section which even begins to adequately thank all of the people who have contributed to my Ph.D. is an impossible task. I will nonetheless attempt to do so.

First and foremost, I owe a deep debt of gratitude to my advisor, Prof. Danna Freedman. I was fortunate enough to be one of the first students Danna accepted into the lab, and she has spent the past five years managing me with patience and good humor, despite my persistence in testing both. I further need to thank Prof. T. David Harris, a member of my committee, who was a source of reassurance during a particularly rough patch, and a source of good beer advice and late-night camaraderie at all other times. I also owe thanks to Prof. Elad Harel, the third member of my thesis committee, and Prof. Brian Hoffman, a member of my qualifying exam committee, for their interest in and constructive criticism of my work throughout the years.

Additional thanks go out to all of my scientific collaborators. During my tenure at Northwestern I've had the good fortune to work with many first-class physicists and spectroscopists who helped me to fill in the gaps in my knowledge. In particular, I thank Prof. Stephen Hill, Dr. Muhandis Shiddiq, Dr. Matthew Krzyaniak, Dr. Likai Song, Dr. Johan van Tol, Dr. Mark Nilges, and Dr. Alexei Bylinskii for their patient instruction. I've also been fortunate to work with a number of talented chemist collaborators, including Dr. Brittany Johnson at the University of Illinois, Chicago and Prof. John Anderson at the University of Chicago. I owe special thanks to the other members of the quantum information subgroup (aka Camp Qubit) – Raymond Yu, Prof. Joseph Zadrozny, and Majed Fataftah. My work would have gone nowhere without their scientific feedback and the many, many discussions of spin physics I've shared with them, and I am profoundly grateful for their contribution to my intellectual growth.

On a more personal level, I am deeply indebted to the friends who kept me (barely) sane

throughout my graduate career. I would have had a much rougher time had I not taken annual trips to New York to visit Lynne Rey, Suveg Pandey, Ariel Mahler, Raymond Fadel, Esq., and Andrew Brownjohn. Their humor, wit, intelligence, warmth, ambition, perceptiveness, and perspective grounded me, and I never failed to come back from those trips feeling refreshed and motivated. Closer to home, I had the company of fellow climbers Joe Accardo, Ruby Krueger, Tom Purcell, Laura Lilley, Scott Coste, and Arash Banisifar to accompany me whenever I felt the urge to "indoor spiderman." Outside of the gym, I was lucky enough to be able to spend time wandering the city with the wonderful Natalia Powers-Riggs, who never fails to make me smile.

I would not be where I am today without the unwavering love and support of my parents, Richard and Berney Graham. They have supported me in all of my crazy endeavors since I can remember, and I haven't made it particularly easy for them. (Imagine hearing your son tell you he's leaving college for a semester to walk 2000+ miles in the woods by himself.) Their encouragement, both verbal and in cookie form, was instrumental in keeping my spirits up and my mind focused on the task at hand during my doctoral studies, and I cannot thank them enough for being the most wonderful set of parents anyone could ever ask for.

Finally, I owe probably the greatest debt for helping me survive the past five years to my colleagues in the Freedman/Harris collective, in particular Raymond Yu, Tyler Pearson, Ryan Klein, Scott Coste, Samantha Clarke, Majed Fataftah, Kelly Powderly, Prof. Joseph Zadrozny, Dr. James Paul Slater Walsh, Audrey Gallagher, Alexandra Gaudette, Kang Du, Jordan DeGayner, Arash Banisifar, Margaret Kelty, and Prof. John Anderson. From Sockem Bopper carnage, to (Tuesday) nights at the Deuce, to scaring the poor drive-thru employees at McDonalds (looking at you, Sam), the last half-decade with you clowns has resulted in a trove of fantastic, albeit hazy, memories, that I will cherish for a long time to come. Though I may not miss the grind of grad

school, I will miss you all immensely. Thank you for being my friends.

LIST OF ABBREVIATIONS

Acac	acetylacetoacetate
Br-mp	2-(bromomethyl)-2-(hydroxymethyl)-1,3-propanediol trianion
Btc	benzenetricarboxylate
cw-EPR	continuous-wave EPR
DCM	dichloromethane
DMF	dimethylformamide
DMSO	dimethyl sulfoxide
DNP-NMR	dynamic nuclear polarization nuclear magnetic resonance
dpm	dipivaloylmethane monoanion
ED-EPR	echo-detected electron paramagnetic resonance
ENDOR	electron-nuclear double resonance
EPR	electron paramagnetic resonance
ESEEM	electron spin echo envelope modulation
HYSORE	hyperfine sublevel correlation
ISC	intersystem crossing
MeCN	acetonitrile
mnt	maleonitrile-2,3-dithiolate
MRI	magnetic resonance imaging
MTHF	2-methyltetrahydrofuran
NMR	nuclear magnetic resonance
NVC	nitrogen-vacancy center
Pc	phthalocyanine dianion

Pc ^{Cl}	perchlorinated phthalocyanine dianion
piv	pivalate
PrCN	butyronitrile
py	pyridyl
tacn	1,4,7-triazacyclononane
trensai	2,2',2''-tris(salicylideneimino)trimethylamine trianion
SOC	spin-orbit coupling
SP-STM	spin-polarized surface tunneling microscopy
Tol	toluene
QIP	quantum information processing.
VS ₆	vanadium tris(dithiolene)

*To my parents, Richard and Berney,
and to Samwise, Jimbo, RAK-attack, Edmund, K-Pow, Ty-fighter, Hottie Scottie, Fatty, and Josie*

Table of Contents

List of Figures	14
List of Tables	17
Chapter One: Introduction	18
1.1 Background	19
1.2 Current state of the art.....	22
1.2.1 Functional properties of molecular qubits	22
1.2.2 Towards long T_2 parameters – the problem of nuclear spins.....	23
1.2.3 Intrinsic and extrinsic properties allow for tuning of T_1	28
1.2.4 Scaling to multi-qubit molecules and quantum gates	30
1.2.5 Deposition and manipulation of qubits on surfaces	33
Chapter Two: Influence of Electronic Spin and Spin-Orbit Coupling on Decoherence in Mononuclear Transition Metal Complexes	35
2.1 Introduction.....	36
2.2 Results and Discussion	37
2.3 Conclusion	42
Chapter Three: Long Coherence Times in Nuclear Spin-Free Vanadyl Qubits	43
3.1 Introduction.....	44
3.2 Results and Discussion	47
3.3 Conclusion	61
Chapter Four: Synthetic Approach to Determine the Effect of Nuclear Spin Distance on Electronic Spin Decoherence	63

	12
4.1 Introduction.....	64
4.2 Results and Discussion	66
4.3 Outlook	74
Chapter Five: Probing Nuclear Spin Effects on Electronic Spin Coherence via EPR Measurements of Vanadium (IV) Complexes.....	75
5.1 Introduction.....	76
5.2 Results and Discussion	78
5.3 Outlook	91
Chapter Six: Conclusion and Outlook	93
6.1 Scaling up requires proof-of-concept molecules and prototype arrays	94
6.2 Optical control of qubits is essential for matching the performance of defect systems	96
6.3 Magnetic resonance imaging probes require tuning of the same properties as molecular qubits.....	98
6.4 MOF-based qubits can serve as quantum sensors.....	99
6.5 Conclusion	101
References.....	103
References for Chapter One.....	104
References for Chapter Two	110
References for Chapter Three	113
References for Chapter Four.....	117
References for Chapter Five	121

References for Chapter Six	13
Curriculum vitae	125
	128

List of Figures

Figure 1.1 Schematic diagram depicting the contrast between a classical bit and a quantum bit (qubit).....	19
Figure 1.2 Schematic diagram of an array of surface qubits	22
Figure 1.3 Five factors which affect T_2	24
Figure 1.4 Plot illustrating the temperature-dependence of T_2 in a range of molecular qubit complexes, and the crystal structures of a selection of those complexes	25
Figure 1.5 Periodic table with elements highlighted according to the natural abundance of zero-spin isotopes.....	26
Figure 1.6 A switchable, two-qubit \sqrt{i} SWAP gate	31
Figure 2.1 Molecular structure and splitting of the M_S levels for $[\text{Cr}(\text{C}_2\text{O}_4)_3]^{3-}$	36
Figure 2.2 Depictions of the molecular structures and relevant properties of $[\text{Ru}(\text{C}_2\text{O}_4)_3]^{3-}$, $[\text{Cr}(\text{C}_2\text{O}_4)_3]^{3-}$, $[\text{Fe}(\text{C}_2\text{O}_4)_3]^{3-}$, $[\text{Fe}(\text{CN})_6]^{3-}$, $[\text{Ru}(\text{CN})_6]^{3-}$, and $[\text{Os}(\text{CN})_6]^{3-}$	38
Figure 2.3 Normalized echo decay curves for $[\text{Fe}(\text{C}_2\text{O}_4)_3]^{3-}$ in 1:1 H_2O /glycerol	39
Figure 2.4 Rabi oscillations and pulse sequence for a solution of $[\text{Ru}(\text{C}_2\text{O}_4)_3]^{3-}$	41
Figure 3.1 Molecular structures of $[\text{VO}(\text{C}_8\text{S}_8)_2]^{2-}$, $[\text{VO}(\beta\text{-C}_3\text{S}_5)_2]^{2-}$, $[\text{VO}(\alpha\text{-C}_3\text{S}_5)_2]^{2-}$, $[\text{VO}(\text{C}_3\text{S}_4\text{O})_2]^{2-}$, $[\text{V}(\text{C}_8\text{S}_8)_3]^{2-}$, $[\text{V}(\beta\text{-C}_3\text{S}_5)_3]^{2-}$, $[\text{V}(\alpha\text{-C}_3\text{S}_5)_3]^{2-}$, and $[\text{V}(\text{C}_3\text{S}_4\text{O})_3]^{2-}$	48
Figure 3.2 Continuous wave (CW) EPR spectra of $[\text{VO}(\text{C}_8\text{S}_8)_2]^{2-}$, $[\text{VO}(\beta\text{-C}_3\text{S}_5)_2]^{2-}$, $[\text{VO}(\alpha\text{-C}_3\text{S}_5)_2]^{2-}$, and $[\text{VO}(\text{C}_3\text{S}_4\text{O})_2]^{2-}$	49
Figure 3.3 Normalized Hahn echo decay curves of $[\text{VO}(\text{C}_8\text{S}_8)_2]^{2-}$, $[\text{VO}(\beta\text{-C}_3\text{S}_5)_2]^{2-}$, $[\text{VO}(\alpha\text{-C}_3\text{S}_5)_2]^{2-}$, and $[\text{VO}(\text{C}_3\text{S}_4\text{O})_2]^{2-}$ in SO_2 at 10 K	51
Figure 3.4 Nutation experiment performed on $[\text{VO}(\text{C}_8\text{S}_8)_2]^{2-}$ in 1:1 DMF- d_7 :Tol- d_8 showing Rabi oscillations.....	52
Figure 3.5 Spin-lattice relaxation rates ($1/T_1$) of $[\text{VO}(\text{C}_8\text{S}_8)_2]^{2-}$, $[\text{VO}(\beta\text{-C}_3\text{S}_5)_2]^{2-}$, $[\text{VO}(\alpha\text{-C}_3\text{S}_5)_2]^{2-}$, and $[\text{VO}(\text{C}_3\text{S}_4\text{O})_2]^{2-}$ as a function of temperature in 1:1 DMF:Tol	54
Figure 3.6 Variable-temperature spin-lattice relaxation rates ($1/T_1$) of $[\text{VO}(\text{C}_3\text{S}_4\text{O})_2]^{2-}$ measured in 4:1 DMF:DMSO, 1:1 DMF:Tol, 1:1 DCM:PrCN, and 1:1 MTHF:Tol	56
Figure 3.7 Decoherence times (T_2) as a function of temperature for four vanadyl bis(dithiolene) complexes in 1:1 DMF:Tol and 1:1 DMF- d_7 :Tol- d_8	58

- Figure 3.8** Proposed model of the spin diffusion barrier of $[\text{VO}(\text{C}_8\text{S}_8)_2]^{2-}$ and $[\text{V}(\text{C}_8\text{S}_8)_3]^{2-}$ in 1:1 DMF:Tol and 1:1 DMF- d_7 :Tol- d_860
- Figure 4.1** Crystal structures of $[\text{VO}(\text{C}_3\text{H}_6\text{S}_2)_2]^{2-}$, $[\text{VO}(\text{C}_5\text{H}_6\text{S}_4)_2]^{2-}$, $[\text{VO}(\text{C}_7\text{H}_6\text{S}_6)_2]^{2-}$, and $[\text{VO}(\text{C}_9\text{H}_6\text{S}_8)_2]^{2-}$ 67
- Figure 4.2** Schematic drawings of $[\text{VO}(\text{C}_3\text{H}_6\text{S}_2)_2]^{2-}$, $[\text{VO}(\text{C}_5\text{H}_6\text{S}_4)_2]^{2-}$, $[\text{VO}(\text{C}_7\text{H}_6\text{S}_6)_2]^{2-}$, and $[\text{VO}(\text{C}_9\text{H}_6\text{S}_8)_2]^{2-}$ 68
- Figure 4.3** Echo-detected EPR spectra for $[\text{VO}(\text{C}_3\text{H}_6\text{S}_2)_2]^{2-}$, $[\text{VO}(\text{C}_5\text{H}_6\text{S}_4)_2]^{2-}$, $[\text{VO}(\text{C}_7\text{H}_6\text{S}_6)_2]^{2-}$, and $[\text{VO}(\text{C}_9\text{H}_6\text{S}_8)_2]^{2-}$ in DMF- d_7 /toluene- d_869
- Figure 4.4** Temperature dependence of T_1^{-1} for $[\text{VO}(\text{C}_3\text{H}_6\text{S}_2)_2]^{2-}$, $[\text{VO}(\text{C}_5\text{H}_6\text{S}_4)_2]^{2-}$, $[\text{VO}(\text{C}_7\text{H}_6\text{S}_6)_2]^{2-}$, and $[\text{VO}(\text{C}_9\text{H}_6\text{S}_8)_2]^{2-}$ in DMF- d_7 /toluene- d_870
- Figure 4.5** Temperature dependence of T_2 for $[\text{VO}(\text{C}_3\text{H}_6\text{S}_2)_2]^{2-}$, $[\text{VO}(\text{C}_5\text{H}_6\text{S}_4)_2]^{2-}$, $[\text{VO}(\text{C}_7\text{H}_6\text{S}_6)_2]^{2-}$, and $[\text{VO}(\text{C}_9\text{H}_6\text{S}_8)_2]^{2-}$ in DMF- d_7 /toluene- d_871
- Figure 4.6** Depiction of a model for the diffusion barrier in $[\text{VO}(\text{C}_3\text{H}_6\text{S}_2)_2]^{2-}$, $[\text{VO}(\text{C}_5\text{H}_6\text{S}_4)_2]^{2-}$, $[\text{VO}(\text{C}_7\text{H}_6\text{S}_6)_2]^{2-}$, and $[\text{VO}(\text{C}_9\text{H}_6\text{S}_8)_2]^{2-}$71
- Figure 4.7** Plot of T_2 versus average V–H distance at 40 K for $[\text{VO}(\text{C}_3\text{H}_6\text{S}_2)_2]^{2-}$, $[\text{VO}(\text{C}_5\text{H}_6\text{S}_4)_2]^{2-}$, $[\text{VO}(\text{C}_7\text{H}_6\text{S}_6)_2]^{2-}$, and $[\text{VO}(\text{C}_9\text{H}_6\text{S}_8)_2]^{2-}$ in DMF- d_7 /toluene- d_872
- Figure 5.1** Crystal structures and schematic drawings of $[\text{V}(\text{C}_5\text{H}_6\text{S}_4)_3]^{2-}$, $[\text{V}(\text{C}_7\text{H}_6\text{S}_6)_3]^{2-}$, and $[\text{V}(\text{C}_9\text{H}_6\text{S}_8)_3]^{2-}$ 78
- Figure 5.2** Cw-EPR spectra of $[\text{V}(\text{C}_5\text{H}_6\text{S}_4)_3]^{2-}$, $[\text{V}(\text{C}_7\text{H}_6\text{S}_6)_3]^{2-}$, and $[\text{V}(\text{C}_9\text{H}_6\text{S}_8)_3]^{2-}$ in DMF- d_7 /toluene- d_880
- Figure 5.3** Mims ENDOR spectra of $[\text{V}(\text{C}_5\text{H}_6\text{S}_4)_3]^{2-}$, $[\text{V}(\text{C}_7\text{H}_6\text{S}_6)_3]^{2-}$, and $[\text{V}(\text{C}_9\text{H}_6\text{S}_8)_3]^{2-}$ 81
- Figure 5.4** Temperature dependence of T_1^{-1} for $[\text{V}(\text{C}_5\text{H}_6\text{S}_4)_3]^{2-}$, $[\text{V}(\text{C}_7\text{H}_6\text{S}_6)_3]^{2-}$, $[\text{V}(\text{C}_9\text{H}_6\text{S}_8)_3]^{2-}$, $[\text{VO}(\text{C}_5\text{H}_6\text{S}_4)_2]^{2-}$, $[\text{VO}(\text{C}_7\text{H}_6\text{S}_6)_2]^{2-}$, and $[\text{VO}(\text{C}_9\text{H}_6\text{S}_8)_2]^{2-}$ in DMF- d_7 /toluene- d_883
- Figure 5.5** Temperature dependence of T_2 for $[\text{V}(\text{C}_5\text{H}_6\text{S}_4)_3]^{2-}$, $[\text{V}(\text{C}_7\text{H}_6\text{S}_6)_3]^{2-}$, $[\text{V}(\text{C}_9\text{H}_6\text{S}_8)_3]^{2-}$, $[\text{VO}(\text{C}_5\text{H}_6\text{S}_4)_2]^{2-}$, $[\text{VO}(\text{C}_7\text{H}_6\text{S}_6)_2]^{2-}$, and $[\text{VO}(\text{C}_9\text{H}_6\text{S}_8)_2]^{2-}$ in DMF- d_7 /toluene- d_885
- Figure 5.6** Cw-EPR spectra for $[\text{V}(\text{C}_7\text{H}_6\text{S}_6)_3]^{2-}$ in MeCN- d_3 /toluene- d_8 , and echo-detected EPR spectra for $[\text{V}(\text{C}_5\text{H}_6\text{S}_4)_3]^{2-}$ and $[\text{V}(\text{C}_9\text{H}_6\text{S}_8)_3]^{2-}$ in MeCN- d_3 /toluene- d_8 87
- Figure 5.7** Temperature dependence of T_1^{-1} for $[\text{V}(\text{C}_5\text{H}_6\text{S}_4)_3]^{2-}$, $[\text{V}(\text{C}_7\text{H}_6\text{S}_6)_3]^{2-}$, and $[\text{V}(\text{C}_9\text{H}_6\text{S}_8)_3]^{2-}$ in MeCN- d_3 /toluene- d_8 88
- Figure 5.8** Temperature dependence of T_2 for $[\text{V}(\text{C}_5\text{H}_6\text{S}_4)_3]^{2-}$, $[\text{V}(\text{C}_7\text{H}_6\text{S}_6)_3]^{2-}$, and $[\text{V}(\text{C}_9\text{H}_6\text{S}_8)_3]^{2-}$ in MeCN- d_3 /toluene- d_8 (open symbols) and DMF- d_7 /toluene- d_888
- Figure 5.9** Scheme demonstrating the effect of charge-to-size ratio on methyl-promoted

decoherence.....	16
.....	90
Figure 6.1 Qubits (glowing components) can be installed in metal organic frameworks via selection of proper structural nodes or linking moieties.....	95
Figure 6.2 Illustration of the photopolarization pathway operative in nitrogen-vacancy centers.....	97
Figure 6.3 The nuclear spins of the molecule ^1H - ^2H in the pores of a $\text{Cu}_{2.97}\text{Zn}_{0.03}(\text{Btc})_2$ framework are detected by Cu^{2+} spin qubits.....	100
Figure 6.4 Depiction of clock transition and known spin qubits that exhibit them	101

List of Tables

Table 2.1 Magnetic parameters and T_2 values for $[\text{Ru}(\text{C}_2\text{O}_4)_3]^{3-}$, $[\text{Cr}(\text{C}_2\text{O}_4)_3]^{3-}$, $[\text{Fe}(\text{C}_2\text{O}_4)_3]^{3-}$, $[\text{Fe}(\text{CN})_6]^{3-}$, $[\text{Ru}(\text{CN})_6]^{3-}$, and $[\text{Os}(\text{CN})_6]^{3-}$ 39

Table 5.1 Best-fit simulation parameters from the ENDOR spectra of $[\text{V}(\text{C}_5\text{H}_6\text{S}_4)_3]^{2-}$, $[\text{V}(\text{C}_7\text{H}_6\text{S}_6)_3]^{2-}$, and $[\text{V}(\text{C}_9\text{H}_6\text{S}_8)_3]^{2-}$ in DMF- d_7 /toluene- d_8 82

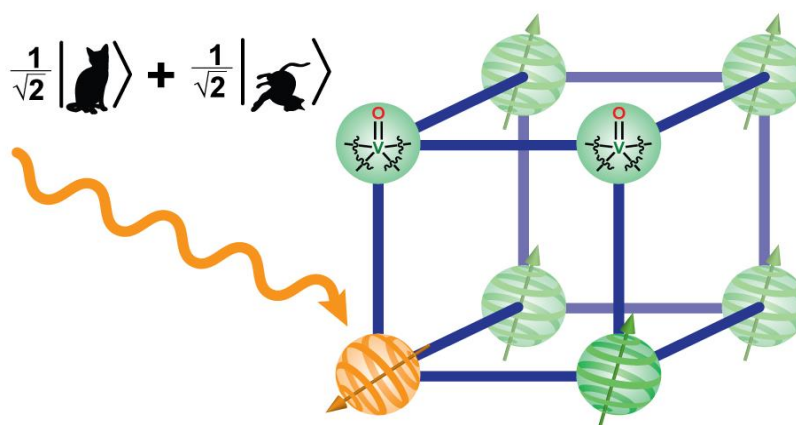
Chapter One: Introduction

Reprinted with permission from:

Graham, M. J.; Zadrozny, J. M.; Fataftah, M. S.; Freedman, D. E. *Chemistry of Materials* **2017**,
29, 1885–1897.

Copyright 2017 American Chemical Society.

This section was written in collaboration with the co-authors listed above.



1.1 Background

Quantum information processing (QIP) is an emerging computational paradigm with the potential to fundamentally transform the current digital landscape and usher in a second information age. QIP differs from its classical analogue due to its use of quantum bits, known as qubits. Classical bits, the basic units of conventional computation, exist in one of two states, 0 or 1, whereas qubits can be placed into a quantum superposition of their two constituent states, thereby simultaneously accessing multiple states (Figure 1.1).¹ The design of viable qubits and their subsequent assembly into a functioning quantum computer is one of the great scientific challenges of our time, as QIP could enable the solution of problems that would take the world's most powerful classical computers the age of the universe to solve.² Such immense computational power would afford insight into currently intractable problems in domains ranging from structural biology to finance.^{3,4}

The era of quantum computer development was formalized in 2000 with the publication of DiVincenzo's five criteria for the construction of a quantum computer.⁵ The five criteria – that qubits be well-characterized and scalable, be capable of initialization into a specific starting state, exhibit long coherence times (the lifetime of the superposition state), form universal gates, and be individually measurable – are both

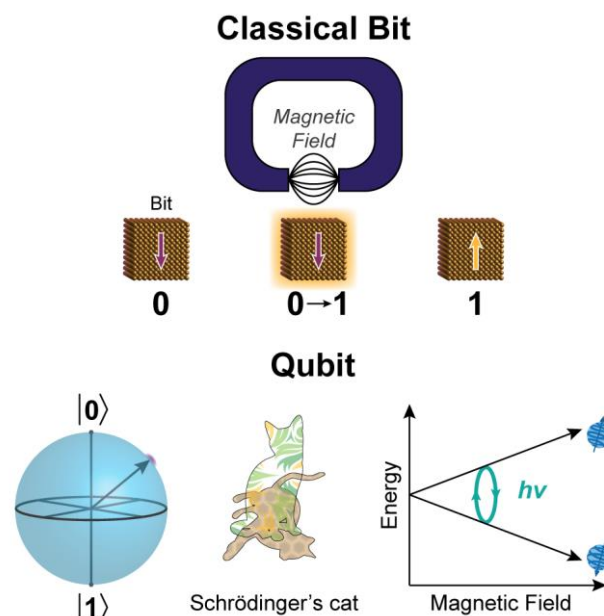


Figure 1.1 Schematic diagram depicting the contrast between a classical bit and a quantum bit (qubit). Top: a magnetic read-write head flipping the orientation of a macroscopic (classical) magnetic bit. Bottom: various representations of a qubit. Left: the Bloch sphere represents all possible qubit superposition states. Center: Schrödinger's cat serves as a common, albeit flawed analogy for the "dead and alive" nature of a qubit superposition. Right: electron spins in a magnetic field can be placed into a superposition between two spin sublevels via pulsed microwaves.

exhaustive and platform-independent, and therefore apply to all proposed implementations of QIP. Understanding what physical properties translate these requirements into candidate qubit systems is at the heart of quantum information science.

The publication of the DiVincenzo criteria instigated the development of test-scale implementations of QIP in multiple forms utilizing photons, nuclear spins, and trapped ions as qubits. One particular implementation that receives an enormous amount of attention is the use of electronic spins located at defect sites in solid-state materials. Electronic spins are particularly well-suited to serve as qubits. They can be readily manipulated on nanosecond timescales with pulsed microwave radiation and easily initialized with light or magnetic fields. A further advantage of electronic spin is the facile manner by which multiple electronic spin qubits are entangled, meaning that they comprise a single quantum mechanical system. This capability is vital for the assembly of qubits into quantum gates, and eventually into scalable systems. Electronic defect sites, in particular nitrogen-vacancy sites in diamond⁶ and double-vacancy sites in silicon carbide,⁷⁻⁹ exhibit many of these features, which are necessary for the implementation of QIP. One of the most important properties of these defect spin qubits is the ability to realize long coherence times. This last property is considerably challenging to achieve in electronic spin qubits, as interactions with the local environment induce rapid collapse of the fragile superposition state in a process known as decoherence.

There are two central challenges to implementing solid-state qubits. The first is a lack of spatial control over their location, which is a requirement for scaling to entangled arrays of qubits. Defect sites are prepared by either electron or ion bombardment, both of which create a random spatial distribution of defect sites in the host material.¹⁰ Although lithographic techniques can be employed to partially specify the locations of the defect sites,^{11,12} it is presently not feasible to

synthesize the consistently-spaced arrays necessary for large-scale quantum computation.¹³

Second, solid-state systems offer no form of synthetic control, meaning that for a given type of defect site, there is no mechanism to tune its electronic or magnetic properties to enable integration with a large-scale device. Surmounting these two obstacles would dramatically increase the suitability of solid-state qubits for incorporation in a future device.

A related approach that garners a large share of attention, especially within the chemical community, is the use of magnetic molecules as hosts for electron spin-based qubits.¹⁴ Electronic spins in magnetic molecules offer three advantages over solid-state systems: reproducible fabrication of qubits via chemical synthesis, extraordinary tunability of the spins by chemical design, and ability of the qubit monomers to form large-scale ordered arrays (e.g. 2D and 3D lattices). These properties inspired a plethora of studies examining the impact of various synthetic parameters on qubit properties, notably yielding a two-order of magnitude increase in the coherence time over the past decade.¹⁵ However, the studies largely neglected to exploit the potential for array formation in these complexes, despite it being the most crucial of the advantages of molecular species. Instead, researchers examined the species of interest in dilute matrices, by dissolving them in solution or by cocrystallization with a diamagnetic analogue. These two approaches only allow measurements to be performed in bulk, on ensembles of spins. A future device requires the *individual* addressing of spins that are coupled to neighboring qubits. Thus, while molecules demonstrate great promise as isolated qubits, considerable challenges stand to implementing them in an actual computing platform.

In this Perspective, we highlight a pathway forward that merges the two paradigms, effectively harnessing the design principles forged through the bulk measurement of magnetic molecules to design solid-state 2D and 3D arrays of spin centers. This approach exploits the potential for

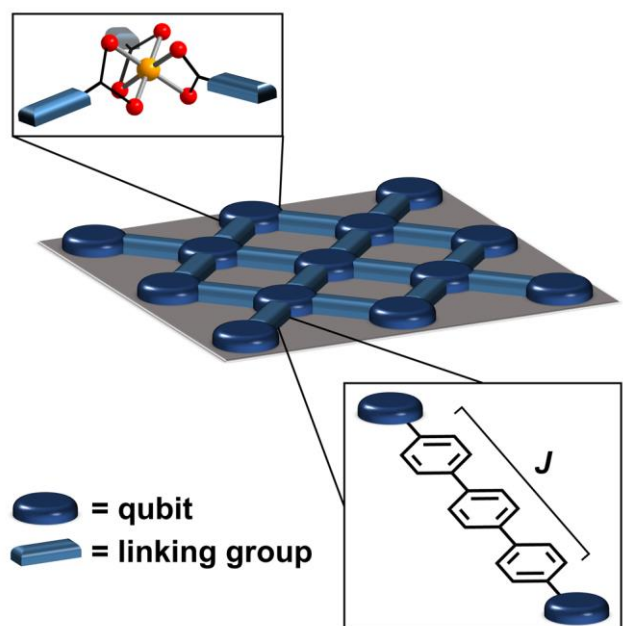


Figure 1.2 Schematic diagram of an array of surface qubits, showing both a potential linker and metal complex geometry. J indicates the strength of the magnetic coupling between the qubits.

single-site addressability intrinsic to a solid-state system while maintaining the highly-prized tunability of the qubit centers. Below, we examine the state of the art in molecular qubits in the context of their ultimate transfer to solid-state architectures. We focus significant attention on the most important next steps in the field: the development of multi-

qubit molecules, enabling optical addressability of molecular qubits, and

constructing qubit frameworks for future device integration. We further examine the broader applicability of qubit design principles toward other applications.

1.2 Current state of the art

A quantum computational architecture which is able to preserve the advantages of molecular systems while successfully translating them into the solid state is likely to take the form of an ordered array of coordination complex qubits. Here, these qubits may be connected by organic or coordination complex-based linkers, e. g. in a metal-organic framework or assembled on a surface (Figure 1.2). In Section 1.3 we discuss the steps necessary to bring this idea to fruition; here we first detail the work accomplished to date on molecular species and how that work informs the design of this type of solid-state architecture.

1.2.1 Functional properties of molecular qubits

The viability of spin-based qubits is determined via pulsed electron paramagnetic resonance

(EPR) spectroscopy. The most important of the qubit parameters is the coherence time, notated as T_2 or T_m , which describes the lifetime of the superposition state before it collapses into one of its constituent classical states.¹⁶ An additional figure of merit is T_1 – the spin-lattice relaxation time – which is the time required for an excited spin to relax back to its ground state. T_1 is an important figure as it is both the upper limit of T_2 ¹⁶ and the lower limit of the timescale of a single computational cycle when thermal relaxation is the method for qubit initialization.¹⁷ As T_1 and T_2 depend on experimental factors like microwave frequency, applied field, and temperature, varying these extrinsic factors and observing the resulting changes can yield mechanistic information regarding these parameters.

1.2.2 Towards long T_2 parameters – the problem of nuclear spins

The elongation of coherence times is a vital strategy towards the use of electronic spins for quantum computation, both in the solid state and in molecular systems. As noted above, one of the DiVincenzo criteria for a quantum computer requires that qubits exhibit long coherence times, with "long" defined as having a coherence time greater than 10^4 times the length of a basic quantum gate operation.⁵ For electronic spin-based systems, the simplest gate operation is the NOT gate, which is equivalent to spin inversion, and occurs on a timescale of ~ 10 ns. The requisite timescale for decoherence is therefore on the order of $100 \mu\text{s}$. Though this value is routinely achieved in defect-based systems,^{8,9,18} the majority of coordination complexes measured before the 2000s exhibited T_2 values of at most a few microseconds, significantly below the target value.¹⁹

The first step towards realizing molecule-derived solid state qubits is therefore a deep understanding of decoherence, the process of superposition collapse, to enable long T_2 parameters to be realized in molecules. Among many potential sources of decoherence (Figure 1.3), it is widely posited that the largest driver of decoherence at low temperatures (typically < 40 K) is a

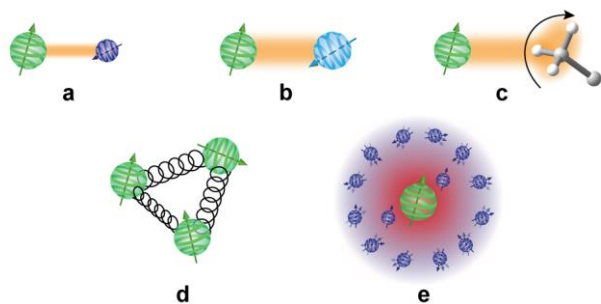


Figure 1.3 Factors which affect T_2 : (a) nuclear spin diffusion, (b) coupling to nearby electronic spins, (c) methyl group rotation, (d) spin-lattice relaxation (T_1), (e) spin diffusion barrier.

phenomenon known as nuclear spin diffusion.

In this effect, flip-flops of nuclear spins in proximity to the electronic spin create magnetic noise that induces decoherence (and shortens T_2). Nearby electronic spins and rotation of methyl groups can also contribute.¹⁹ The existence of these

contributing factors was previously established. However, prior to the last decade, a set of synthetic design parameters that tied specific changes in molecular structure to differences in coherence times was generally lacking. This uncertainty made the development of new, viable, solid-state systems particularly difficult.

The development of such structure-property relationships for spin coherence was therefore an initial target of the research community. One of the first relationships to be explored was the influence of spin-active nuclei on decoherence, due to their omnipresence in ligand architectures and proven role in shortening T_2 . Initial investigations highlighted the utility of ligand deuteration for T_2 enhancement (e.g. $0.55 \mu\text{s}$ for $\text{Cr}_7\text{NiF}_8(\text{piv})_{16}$ to $3.8 \mu\text{s}$ for $\text{Cr}_7\text{NiF}_8(\text{piv-}d_8)_{16}$ at 1.8 K).²⁰ Deuterium exhibits a much lower magnetic moment than protium (^1H , $\mu = 2.79 \mu_N$ vs. ^2H , $\mu = 0.86 \mu_N$),²¹ and thus contributes less to decoherence. The influence of nuclear spins extends into the molecular environment; this property resulted in studies which enhanced T_2 by replacing proton-rich organic solvents with the spin-free solvent CS_2 ,^{22,23} and by reducing the number of spin-active nuclei located on the counterion of the qubit complex.²⁴ Ligand-based methyl rotations are additionally detrimental to T_2 (Figure 1.3), though increasing steric hindrance of the methyl group raises the energy barrier to rotation and partially suppresses the effect.^{19,24-26} By attempting to

design around these factors, researchers were able to design a complex possessing a T_2 of 15.3 μs at 1.5 K, an order of magnitude greater than many previous compounds.²⁴ This body of work thus demonstrated the profound power of synthetic chemistry to extend coherence times.

The foregoing demonstrations instigated subsequent efforts to synthesize systems with minimal quantities of both methyl groups and spin-active nuclei (Figure 1.4). A successful

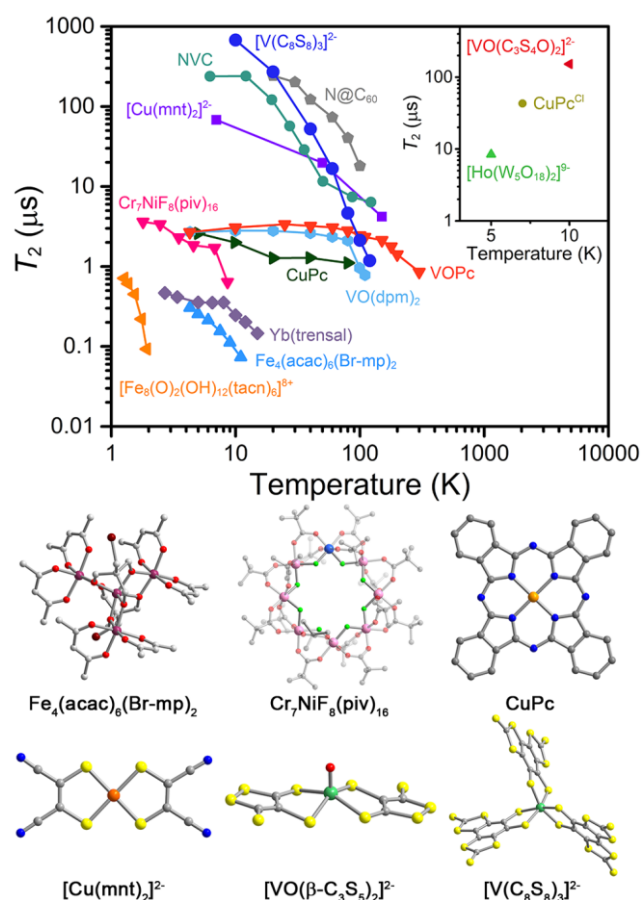


Figure 1.4 Plot illustrating the temperature-dependence of T_2 in a range of molecular qubit complexes, and the crystal structures of a selection of those complexes. Purple, orange, pink, light blue, green, maroon, light green, blue, yellow, red, and gray spheres represent iron, copper, chromium, nickel, vanadium, bromine, fluorine, nitrogen, sulfur, oxygen, and carbon atoms, respectively. Inset: Data for selected complexes which were not collected as part of a temperature-dependence study. Data for all complexes were extracted from references 15, 20, 22, 27–32, 34, 39, 67, and 71–73. Note, the values depicted above represent the maximum measured values of T_2 and do not indicate an intrinsic upper limit for each system.

example was $(\text{Ph}_4\text{P})_2[\text{Cu}(\text{mnt})_2]$, in which the only spin-active nuclei in the ligand field were ^{14}N atoms ($\mu = 0.40 \mu\text{N}$).²¹ When synthesized as the perdeuterated analogue and doped into the diamagnetic congener $(\text{Ph}_4\text{P-}d_{20})_2[\text{Ni}(\text{mnt})_2]$, the species achieved an impressive coherence time of 68(3) μs at 7 K and a value of 600(2) ns at room temperature.²⁷ The ability of deuterated mnt-based complexes to achieve long coherence times was later confirmed with a study of $(\text{Ph}_4\text{P-}d_{20})[\text{Ni}(\text{mnt})_2]$ which demonstrated a T_2 of 38.7 μs at 7 K.²⁸ These molecules represented an important development in new molecular qubits, yet the values of T_2 are still significantly below the threshold value of 100 μs required for viability, and even further below the 631(9) μs value attained by nitrogen

vacancies in diamond at room temperature.¹⁸

The next logical step was the complete exclusion of nuclear spins from the system, an approach which our group and others pursued. However, the majority of elements in the periodic table possess significant natural abundances of isotopes with nuclear spin (Figure 1.5), making this a challenging endeavor. Thus, we targeted complexes with ligands containing only carbon and sulfur, as these have among the highest natural abundances of spin-free isotopes. One such molecule, $[\text{V}(\text{C}_8\text{S}_8)_3]^{2-}$, was prepared with $(\text{Ph}_4\text{P}-d_{20})^+$ cations, and revealed a remarkable 675(7) μs value of T_2 at 10 K following dissolution in carbon disulfide.¹⁵ This observation marked the first time a T_2 above 100 μs was achieved by a molecular complex and was doubly notable for exhibiting a T_2 longer than any other non-isotopically enriched electronic qubit, including nitrogen vacancy centers (NVCs) in diamond^{18,29} or N-atoms implanted inside C_{60} (Figure 1.4).^{23,30} We followed up on this work by showing that vanadyl-based complexes bearing nuclear spin-free ligands could also exhibit threshold-surpassing coherence times of up to 152(6) μs at 10 K in a nuclear spin-free environment by employing the more polar spin-free solvent SO_2 .³¹ Studying the vanadyl systems was important as other studies had shown that the planarity of vanadyl complexes enables their deposition on surfaces;³² thus the vanadyl moiety represents an important path forward in the quest for scalability (see section 1.2.5).

In parallel with studies focused on designing a long T_2 , a separate vein of research concentrated on the exact ways in which nuclear spins affect electronic spin

1																	2		
H																	He		
3	4													5	6	7	8	9	10
Li	Be													B	C	N	O	F	Ne
11	12													13	14	15	16	17	18
Na	Mg													Al	Si	P	S	Cl	Ar
19	20	21	22	23	24	25	26	27	28	29	30	31	32	33	34	35	36		
K	Ca	Sc	Ti	V	Cr	Mn	Fe	Co	Ni	Cu	Zn	Ga	Ge	As	Se	Br	Kr		
37	38	39	40	41	42	43	44	45	46	47	48	49	50	51	52	53	54		
Rb	Sr	Y	Zr	Nb	Mo	Tc	Ru	Rh	Pd	Ag	Cd	In	Sn	Sb	Te	I	Xe		
55	56	57-71	72	73	74	75	76	77	78	79	80	81	82	83	84	85	86		
Cs	Ba		Hf	Ta	W	Re	Os	Ir	Pt	Au	Hg	Tl	Pb	Bi	Po	At	Rn		
87	88	89-103	104	105	106	107	108	109	110	111	112	113	114	115	116	117	118		
Fr	Ra		Rf	Db	Sg	Bh	Hs	Mt	Ds	Rg	Cn	Nh	Fl	Mc	Lv	Ts	Og		
Lanthanides		57	58	59	60	61	62	63	64	65	66	67	68	69	70	71			
Lanthanides		La	Ce	Pr	Nd	Pm	Sm	Eu	Gd	Tb	Dy	Ho	Er	Tm	Yb	Lu			
Actinides		89	90	91	92	93	94	95	96	97	98	99	100	101	102	103			
Actinides		Ac	Th	Pa	U	Np	Pu	Am	Cm	Bk	Cf	Es	Fm	Md	No	Lr			

Figure 1.5 Periodic table with elements highlighted according to the natural abundance of zero-spin isotopes. Green: $\geq 90\%$ abundance, yellow: $\geq 80\%$ abundance, orange: $\geq 70\%$ abundance, white: $< 70\%$ abundance.

coherence. Though the presence of nuclear spins is known to shorten T_2 , the specifics of which types of nuclear spins and which locations relative to the electronic spin are most detrimental remains an open question. This knowledge is vital for creating systems which harbor nuclear spins but still exhibit long coherence times, enabling greater synthetic flexibility in molecular qubit design. A central concept in this research is the diffusion barrier radius (Figure 1.3). For an electronic spin qubit, environmental nuclear spins within the radius are strongly coupled to the electronic spin.^{19,33} Consequently, these spins do not actively flip and induce decoherence, unlike nuclear spins outside the radius. This phenomenon is the reason that nuclear spin can be present on the electron spin-bearing ion (e.g. ^{51}V , $\mu = 5.15 \mu_N$, or ^{63}Cu , $\mu = 2.23 \mu_N$)²¹ without adversely impacting T_2 .³⁴

Understanding how the diffusion barrier radius changes as a consequence of molecular and electronic structure is a key challenge in designing complexes with long T_2 values and molecular arrays. Towards this end, our group comparatively investigated a series of vanadyl bis(dithiolene) complexes and their vanadium tris(dithiolene) analogues. A notable discrepancy between the T_2 values of the two series at low temperature was observed, which could be explained by accounting for the effect of the diffusion barrier radius.³¹ Following that study, our group synthesized a series of four vanadyl bis(dithiolene) molecules which systematically varied the distance between the vanadium ion and a set of protons via the use of a spin-free carbon-sulfur scaffold.³⁵ The series exhibited a notable increase in T_2 (from 7.52(2) to 9.97(3) μs at 40 K) when the average vanadium-proton distance was decreased from 6.6(6) to 4.0(4) \AA , implying a diffusion barrier between those two values. The combination of the above studies elucidated an important design principle: that protons can be incorporated into the design of a qubit complex as long as they are restricted to the immediate coordination sphere. Allowing spin active nuclei in the immediate coordination sphere

of a metal ion drastically expands the number of chemical linkers that can be employed in the synthesis of long-coherence qubit arrays.

1.2.3 Intrinsic and extrinsic properties allow for tuning of T_1

The importance of T_1 to quantum computation lies not only in its effect on T_2 ,¹⁹ but also in the fact that it reflects the timescale of thermal qubit initialization. Effective qubit initialization is one of DiVincenzo's five criteria,⁵ and since all qubits must be in one uniform state before a computational operation can be performed, the speed of initialization limits the speed of the quantum processor. Thus, in a system where spin-lattice relaxation is employed as the initialization mechanism, the processor speed is proportional to $1/T_1$.¹⁷

There are four main mechanisms responsible for spin-lattice relaxation, and the interplay between them at a given temperature governs T_1 .¹⁹ In the temperature regime relevant to quantum computation (<100 K), these processes are the direct process, the Raman process, the Orbach process, and local vibrational modes. The direct process is dominant at the lowest temperatures (up to 20 K) and operates via the emission of a phonon corresponding to the energy of a spin-flip transition. By contrast, the Raman process, which occurs at higher temperatures (typically below 150 K) is similar to the Raman scattering of light – two phonons are simultaneously absorbed and emitted, with the difference in energy between the two corresponding to the spin-flip transition. The Orbach process, like the Raman process, involves two phonons, but occurs via excitation to a real excited state instead of a virtual one. Local modes, as the name indicates, are localized vibrations involving the spin-bearing ion which promote relaxation. Each of these four processes exhibits a different temperature dependence of their contribution to T_1 , and therefore the contribution of each to the overall T_1 can be ascertained by measuring the temperature dependence of T_1 .

Prior to the study of T_1 for QIP, molecular rigidity was understood to be the primary determinant of the relaxation rate in the solid state and frozen solution,^{36,37} the imprecise nature of this criterion drove the need to understand the specific contributions of well-defined chemical moieties to T_1 . One of the most important recent results on this topic was the realization of the ability of the vanadyl moiety to lengthen T_1 in comparison to non-oxo vanadium species. Two separate studies confirmed a roughly order of magnitude increase in spin-lattice relaxation time on moving from vanadium(IV) in a tris(dithiolene) environment to the analogous vanadyl bis(dithiolene) complex.^{31,38} However, it is unclear whether the origin of this effect is the rigidity of the vanadium-oxo bond, or its polarity. In the former case, replacing a dithiolene ligand with an oxo moiety reduces the number of low-energy vibrational modes which contribute to shortening T_1 . In the latter case, the polarity of the moiety engenders stronger dipolar interactions with surrounding molecules, causing a general rigidification of the lattice around the molecules and thus a longer T_1 . The aggregate of these studies represents the creation of an important design principle for modifying T_1 . Developing a detailed understanding of which of these mechanisms is operative will enable translation of these studies to molecules on surfaces. This is an area which will benefit from new approaches and studies to establish the mechanism.

Environmental factors also play a large role in spin-lattice relaxation. One example of this is the effect of differing qubit dilutions: studies by numerous researchers demonstrate that dilution of molecular qubits in the crystalline solid state significantly lengthens T_1 relative to frozen solution.^{27,38,39} T_1 additionally can be susceptible to spin-phonon bottleneck effects in crystalline solid dilutions which drastically alter the low-temperature spin-lattice relaxation rates. Given that molecules on a surface in a high-vacuum environment undergo spin-lattice relaxation predominantly through the substrate, this suggests tuning of the substrate and substrate-qubit

interface are important potential handles for controlling T_1 .⁴⁰ The magnetic field at which relaxation processes are probed is yet another environmental factor affecting T_1 . For example, a combination of studies demonstrated that T_1 exhibits an inverted U-shaped dependence on applied magnetic field, where T_1 is maximized at fields of a few tesla, and drops dramatically near zero field and at higher (~ 10 T) fields.^{32,38–42}

The aggregate of the aforementioned work yields a plethora of design principles that enable tuning of T_1 to values long enough not to limit T_2 , but short enough to produce fast initialization. Though other methods may be superior to thermalization for qubit initialization (see below), T_1 remains an important target for rational synthetic control. The design principles generated for tuning it will significantly aid the translation of molecular qubits into solid-state arrays.

1.2.4 Scaling to multi-qubit molecules and quantum gates

The synthesis of proof-of-concept molecules that demonstrate scalability is integral to the process of moving molecular qubits into the solid state. The original proposal for scalability within molecular systems envisioned the implementation of multiple qubits entirely within a single complex, here employing the multitude of EPR transitions intrinsic to a molecule with a high spin.¹⁴ This approach to scalability received considerable attention, resulting in the first coherent manipulation of spin qubits in both the ground state $S = 1/2$ and excited state $S = 3/2$ manifolds of the single-molecule magnet $[\text{V}_{15}\text{As}_6\text{O}_{42}(\text{H}_2\text{O})]^{6-}$.^{43,44} Complex M_S manifolds such as this are enabled through harnessing electronic structure considerations like exchange coupling (as employed in the V_{15} system),⁴⁵ but also including zero-field splitting,⁴⁶ and hyperfine coupling.⁴⁷ Ultimately, scaling to multi-qubit systems is likely to entail the linking of multiple spin centers.

The approach of weakly coupling multiple spin centers together to create quantum logic gates is an important rational strategy to building a quantum computer. Quantum logic gates, analogous

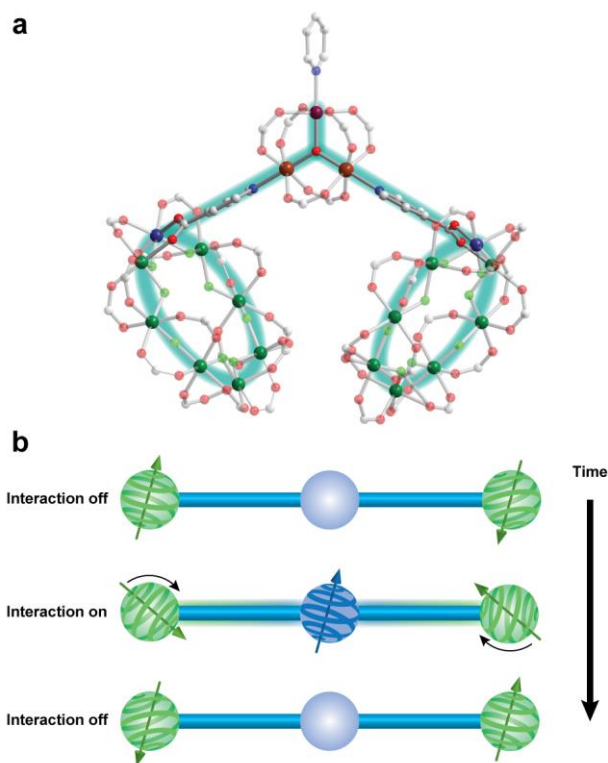


Figure 1.6 A switchable, two-qubit \sqrt{i} SWAP gate. (a) Crystal structure of the molecular gate candidate synthesized by Winpenny and coworkers, $\{\text{Cr}_7\text{NiF}_8(\text{piv})_{15}(\text{O}_2\text{C-py})\} \rightarrow [\text{Ru}_2\text{Co}(\mu\text{-O})(\text{piv})_6(\text{py})] \leftarrow \{\text{Cr}_7\text{NiF}_8(\text{piv})_{15}(\text{O}_2\text{C-py})\}$.⁵⁹ Green, dark purple, brown, maroon, gray, red, blue, and light green spheres represent Cr, Ni, Ru, Co, C, O, N, and F atoms, respectively. Protons and the *tert*-butyl groups of the pivalate moiety have been omitted for clarity. (b) Schematic demonstrating the operation of the \sqrt{i} SWAP gate. Turning the interaction on between the two adjacent qubits (green) via the creation of a spin that links the qubits (blue) permits execution of the gate, in which the qubits partially swap orientation. The interaction is then turned off by returning the linking unit to its diamagnetic state.

to their classical counterparts, are the functional component of a processor lying just above the qubit in complexity. They take inputs and produce an output based on a logical rule. Two examples of quantum gates are the controlled-NOT (CNOT) gate,¹ which inverts the state of the second qubit if and only if the first qubit is in a specific state, and the \sqrt{i} SWAP gate, which partially swaps the states of two qubits (Figure 1.6).⁴⁸ Either of these two-qubit gate types, when incorporated

into a device alongside one-qubit gates such as the NOT gate, is sufficient to create a fully-functioning universal quantum computer.⁴⁹ Consequently, significant effort is focused on implementing these two vital gates in molecular species.

In targeting linked qubit systems, the community has focused on exploring the extent to which qubits can be connected and coupled in a rational manner. Proofs of concept include a range of systems from organic biradicals⁵⁰ to dilanthanide molecules,^{51,52} and even spatially-separated coordination complexes coupled via a resonator.⁵³ Amongst these numerous approaches, the most investigated path involves the chemical and magnetic coupling of heterometallic complexes. By employing this strategy,⁵⁴⁻⁵⁶

Winpenny and coworkers demonstrated the ability to controllably tune interqubit coupling values in multi-qubit species. The qubit linkers used here encompass a number of different chemical coupling methods, ranging from organic linkers, to hydrogen bonding motifs, to coordination complexes, and to supramolecular architectures such as rotaxanes.⁵⁷

Attention then turned to synthesizing molecules with coupling values suitable for the implementation of gates. For the CNOT gate, the coupling between the qubit centers (J) exhibits a characteristic timescale (\hbar/J where \hbar is the Planck constant) which must lie between T_2 and the timescale for qubit manipulation. Further, as the characteristic gate time determines the speed of the gate, shorter timescales are better than longer ones. Since the characteristic timescale for qubit manipulation in electronic spins is ~ 10 ns, the ideal gate time is on the order of 100 ns, which corresponds to a coupling value of $J = 10$ MHz (0.00033 cm^{-1} , 0.00048 K).⁵⁸ The 10 ns control time also implies that the maximum allowable coupling between qubits is on the order of $J = 100$ MHz. Ultimately, fine-tuning of coupling in a variety of heterometallic complexes was shown to enable gate timescales ranging from 77 to 550 ns, the nearly ideal values.⁵⁸

A more daunting challenge in the creation of quantum gates entails designing switchability of the interaction between the two constituent qubits. Switching is vital for the implementation of quantum gates. For example, a CNOT gate with always-on interaction between the qubits (as described above) allows unwanted interactions that require additional error correction. In the case of the \sqrt{i} SWAP gate, which partially swaps the states of the two constituent qubits, the operation is performed by switching on the interaction between the qubits for a specific period of time (Figure 1.6). Implementing single-qubit gates also requires switching in order to temporarily isolate the qubit from all surrounding qubits, making it an indispensable feature.^{59,60}

Various proposals exist for chemically designing switchable interactions between qubits. One

of the ideas, which resulted in promising proof-of concept demonstrations, involves incorporating a switchable linker which can change between a ground state and an excited state in order to entangle two qubits.^{49,59–62} For the ground state of the linker, the interaction between the bridged qubits is turned off, but by excitation into the high-energy state, the linker enables entanglement of the two qubit moieties. One implementation of this proposal entails the use of a paramagnetic linking moiety which can be manipulated by an electromagnetic pulse.^{49,62} Though this implementation requires intensive fine-tuning of interspin couplings, researchers successfully synthesized multiple molecules capable of performing a CNOT gate using this paradigm.^{49,62} A second variation of switchable interaction requires a redox-active linker bridging two qubit moieties. Work by Winpenny and coworkers on synthesizing such a molecule⁴⁹ resulted in the discovery of a candidate molecular quantum gate consisting of two $S = 1/2$ Cr₇Ni rings bridged by a redox-active linker comprised of a Ru₂Co triangular unit.⁵⁹ By oxidizing the $S = 1/2$ Ru^{III}₂Co^{II} subunit by one electron to an $S = 0$ species, the coupling between the centers could be switched off. On the basis of this switch, this molecule is a strong candidate for implementing an \sqrt{i} SWAP gate (Figure 1.6). Further, the use of a redox switching mechanism means that a scanning tunneling microscopy (STM) probe tip could be used to alter the oxidation state of the bridge, allowing for full control over the species on a surface.^{59,60}

1.2.5 Deposition and manipulation of qubits on surfaces

The majority of work on molecular qubits employs characterization in solution or solid dilutions, which favors small molecules but not complex architectures. Surfaces, in contrast, provide a means of allowing the assembly of scalable, molecule-inspired computers in a rational way (Figure 1.2).⁶³ As initial steps in this direction, researchers demonstrated deposition of magnetic multinuclear^{64,65} and mononuclear complexes³² onto both a Au(111) surface and

pyrolytic graphite.⁶⁶ One of the most successful deposition experiments to date involved the codeposition of copper phthalocyanine (CuPc) with free-base phthalocyanine as a diluent on a Kapton film and subsequent measurement by EPR.⁶⁷ However, significant work remains to bridge the gap between these examples and a defect-free surface qubit network suitable for computation.

Once created, a 2D qubit network will face another challenge of addressing molecular qubits: individual manipulation. The most promising technique for this is currently spin-polarized STM (SP-STM), in which an STM tip is capped by a paramagnetic atom which only allows electrons in one electronic state to pass.⁶⁸ In the past few years, multiple groups have made extraordinary advances in the use of SP-STM for surface EPR. In a report in 2010, Loth, Heinrich and coworkers demonstrated the measurement of electron spin relaxation times of single atoms on a Cu(100) surface.⁶⁹ Five years later, Baumann, Paul and coworkers reported a full suite of EPR measurements including an EPR spectrum, T_1 , and T_2 measurements of individual iron atoms on a magnesium oxide surface.⁷⁰ The spectacular advancements achieved in this short period of time in addressing surfaces underscore the potential for usable prototype surface-qubit devices to be manufactured in the coming decade, provided that the chemical species are synthesized to enable it.

Chapter Two: Influence of Electronic Spin and Spin-Orbit Coupling on Decoherence in Mononuclear Transition Metal Complexes

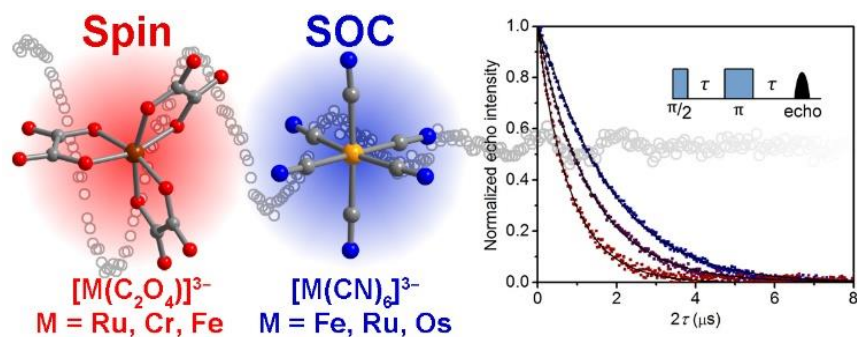
Reprinted with permission from:

Graham, M. J.; Zadrozny, J. M.; Shiddiq, M.; Anderson, J. S.; Fataftah, M. S.; Hill, S.;

Freedman, D. E. *Journal of the American Chemical Society* **2014**, *136*, 7623–7626.

Copyright 2014 American Chemical Society.

This work was performed in collaboration with the co-authors listed above.



2.1 Introduction

The realization of quantum information processing (QIP) is a fundamental challenge with important contributions arising from the intersection of chemistry and physics. Indeed, particular attention is warranted from chemists because a quantum computer could accurately simulate the quantum behavior of chemical

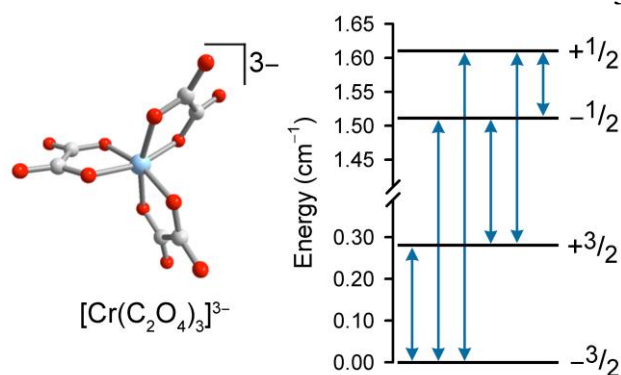


Figure 2.1 Left: Molecular structure of $[\text{Cr}(\text{C}_2\text{O}_4)_3]^{3-}$. Light blue, red, and gray spheres represent chromium, oxygen, and carbon atoms, respectively. Right: Splitting of the M_S levels of the $S = 3/2$ moment in $[\text{Cr}(\text{C}_2\text{O}_4)_3]^{3-}$, calculated for $g_z = 1.99$, $D = -0.71 \text{ cm}^{-1}$, $E = 0 \text{ cm}^{-1}$ under a static 1000 Oe dc field parallel to the z -axis. Blue arrows indicate the six potential qubits in $[\text{Cr}(\text{C}_2\text{O}_4)_3]^{3-}$.⁴

systems.¹ While many systems have been proposed for QIP,² electronic spin represents a promising approach to quantum bits, or qubits.³ Electronic spin-based QIP employs transitions between M_S levels that can be simply addressed by electron paramagnetic resonance (EPR) spectroscopy. Utilizing electronic spin as a qubit offers a key advantage, namely that a single parameter, zero-field splitting, creates a manifold of separately addressable transitions, each one a qubit. The inherent scalability and tunability engendered by zero-field splitting are illustrated in Figure 2.1, which depicts a molecule with spin quantum number S possessing $2S+1$ M_S states and $S(2S+1)$ unique transitions between pairs of those states that could be utilized as qubits.⁴ As zero-field splitting is a synthetically tunable property of high-spin transition metal complexes that splits M_S levels by energies determined by axial (D) and transverse (E) components, it ensures uniqueness of the energies of each of the $S(2S+1)$ qubits.^{3,5,6} Scalability in electron-based QIP is further enabled by the relative strength of magnetic superexchange coupling relative to nuclear-spin systems, thus creating potentially strong inter-qubit interactions over long distances.⁷ The simultaneous realization of scalability and tunability in electron spin qubits demonstrates their

promise for the implementation of quantum computation.^{8,9}

The primary challenge in realizing electronic spin-based QIP lies in developing a long coherence lifetime for the qubit, T_2 ,¹⁰ relative to the timescale of a computational cycle.^{9,11} This is a particular challenge for electronic spin-based QIP because T_2 values for electron spins are typically short.^{7,8,12,13} Yet, theoretical estimates of achievable coherence times¹⁴ suggest that long coherence times are within a synthetically tunable range. Thus, the preparation of molecules with long coherence times is a valuable design target for inorganic chemists.

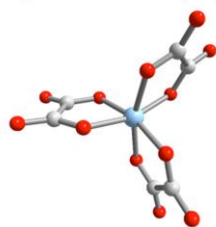
Rational synthesis of molecular qubits necessitates the ability to design molecules with long coherence times. Connecting electronic and molecular structure with decoherence would give rise to design principles that could be followed for the preparation of long-lived electron spin qubits. Two aspects of the electronic structure of paramagnetic complexes which are essential for tuning the qubit transition manifold are S and spin-orbit coupling (SOC).¹⁵ Notably, both of these have also been implicated as major facilitators of decoherence.^{7,16–19} Indeed, the presence of a larger S increases the contribution of electronic dipolar decoherence mechanisms to the overall decoherence rate,^{7,16} while greater SOC allows more rapid decoherence by enhancing coupling between lattice phonons and spin.²⁰ To the best of our knowledge, however, rigorous experimental examination of the contribution of these processes to decoherence under conditions relevant to QIP is lacking. Herein, we report a systematic investigation of the influence of spin magnitude and SOC on coherence times in six paramagnetic transition metal complexes, and demonstrate proof-of-concept with a new candidate qubit.

2.2 Results and Discussion

Six molecules were selected for a systematic study of decoherence comprising two series, one varying the magnitude of S and the other varying SOC (see Figure 2.2). The complexes selected

were $\text{K}_3[\text{Ru}(\text{C}_2\text{O}_4)_3]$ (**1**),²¹ $\text{K}_3[\text{Cr}(\text{C}_2\text{O}_4)_3]$ (**2**),²² $\text{K}_3[\text{Fe}(\text{C}_2\text{O}_4)_3]$ (**3**), $(\text{Ph}_4\text{P})_3[\text{Fe}(\text{CN})_6]$ (**4**),²³ $(\text{Ph}_4\text{P})_3[\text{Ru}(\text{CN})_6]$ (**5**),²⁴ and $(\text{Ph}_4\text{P})_3[\text{Os}(\text{CN})_6]$ (**6**).²⁵ Molecules **1–3** and **4–6** vary spin magnitude and SOC, respectively. The complexes of **1–3** possess spin states of $S = 1/2$, $3/2$, and $5/2$, while those of **4–6** are all $S = 1/2$, but feature increasing free-ion SOC constants of 464, 880, and 3100 cm^{-1} .^{23b,24a,25}

Spin series (S)

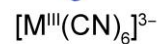
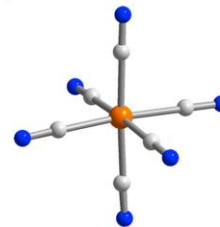


1, M = Ru, $S = 1/2$

2, M = Cr, $S = 3/2$

3, M = Fe, $S = 5/2$

Spin-orbit series (ζ)



4, M = Fe, $\zeta = 464 \text{ cm}^{-1}$

5, M = Ru, $\zeta = 880 \text{ cm}^{-1}$

6, M = Os, $\zeta = 3100 \text{ cm}^{-1}$

Figure 2.2 Depictions of the molecular structures of the spin series **1–3** (left) and spin-orbit series **4–6** (right). Red, blue, and gray spheres represent oxygen, nitrogen, and carbon atoms, respectively. The central light blue and orange spheres represent the varying metal atoms.

These compounds were meticulously selected to create systematic variation of the desired property while maintaining other features of the electronic structure. Importantly, octahedral coordination environments were maintained throughout both series, although the oxalate complexes do deviate from perfect octahedral symmetry. Within each series uniform ligand fields were employed to reduce variation in the structural and electronic properties. All of these molecules possess half-integer spin states, allowing more facile EPR spectroscopic characterization. To eliminate complications arising from nuclear spin-based decoherence within the molecules, complexes in a zero nuclear spin ligand field were selected for the spin series of compounds, while the SOC series employed ligands with nitrogen as the only spin-active nucleus.^{8,20,26,27} All metals selected contain a low natural abundance of spin-active isotopes. However, nuclear spin could not be removed from the solvents and that will be the subject of a future study. Within the spin series **1–3**, it was not possible to completely control for the variation of SOC, as it varies with element and oxidation state.⁵ However, the larger spin-orbit coupling of

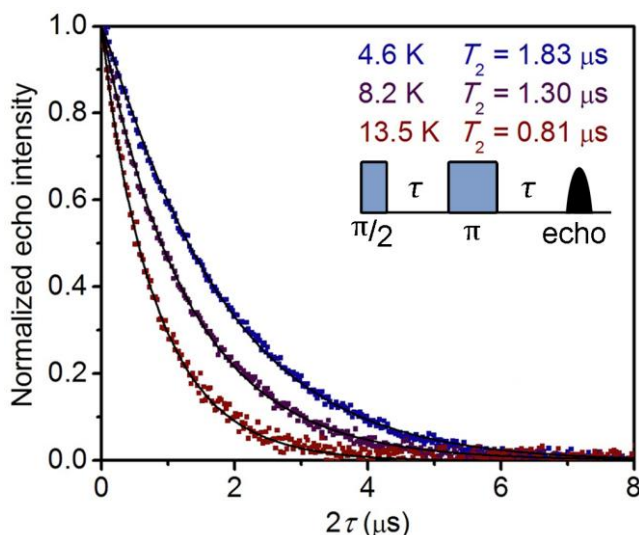


Figure 2.3 Normalized decay curves for **3** in 1:1 H₂O/glycerol and graphical depiction of the Hahn echo pulse sequence. The black lines represent stretched exponential functions fit to the data.

compound **1** compared with compounds **2** and **3** provided a useful intersection point between the two series and allowed for a direct comparison of the effects of both properties of interest. Compounds **1–6** were prepared following literature methods, with the exception of **3**, which was used as received. However, the synthesis of **5** required substantial modification of the original procedure.^{24a}

Coherence times (T_2) for frozen 1 mM solutions of **1–6** in 1:1 (v/v) H₂O/glycerol were extracted from data obtained by application of a two-pulse Hahn echo sequence at temperatures ranging from 5–22 K. The pulse sequence we employed is depicted in Figure 2.3. Cw-EPR spectra were acquired to determine zero-field splitting parameters for **2** and **3**. Echo intensities were recorded as a function of dc applied field. In each echo-detected field-swept spectrum, a maximum in the echo intensity was observed at the dc fields listed in Table 2.1. Echo decay curves were subsequently acquired on all samples at the field of maximum echo intensity. Echo intensities decayed with increasing interpulse delay times (τ) for all complexes, and the rate of decay increased with increasing temperature (see Figure 2.3). Quantitation of

Table 2.1 Magnetic parameters and T_2 values^a for **1–6**.

	1	2	3
S	$1/2$	$3/2$	$5/2$
H_{dc} (Oe) ^c	2812	2130	3501
T_2 at 5 K	3.44(1)	2.79(3)	1.83(1)
T_2 at 14	2.01(1)	1.86(3)	0.81(1)
T_2 at 22	0.41(2)	1.27(4)	0.45(5)
	4	5	6
S	$1/2$	$1/2$	$1/2$
ζ (cm ⁻¹) ^b	464	880	3100
H_{dc} (Oe) ^c	3364	3394	3865
T_2 at 5 K	2.38(6)	2.55(4)	4.12(6)
T_2 at 13	0.55(8)	1.25(5)	3.17(4)
T_2 at 22	0.60(9)	1.29(10)	1.04(4)

^aIn units of μ s, as determined on 1 mM solutions in 1:1 H₂O/glycerol. ^bFree-ion values from refs. 23b, 24a and 25. ^cDc applied field at highest echo intensity.

T_2 proceeded by fitting the decay of the echo intensity by a stretched exponential function, $I(2\tau) = I(0)\exp(-(2\tau/T_2)^x)$, where I is the echo intensity, $I(0)$ a pre-exponential factor, and x the stretch factor, while τ and T_2 possess their previously-defined meanings. Values of T_2 obtained from the best fits to the data are listed in Table 1. For **1–3**, T_2 decreases slightly at 5 K from 3.44(1) in **1** to 1.83(1) μs in **3**. T_2 values slightly increase from **4** to **6**, ranging from 2.38(6) to 4.12(6) μs at 5 K. These values of T_2 for **1–6** are comparable in magnitude to other mononuclear transition metal complexes.²⁸

Insight into the impact of spin magnitude on decoherence can be attained through comparison of the T_2 values across **1–3**. The results confirm that increasing spin magnitude impacts decoherence: **1** displayed the longest T_2 values, followed by **2** then **3**. Thus, the trend in our data is in accordance with expected results: a larger spin magnitude will increase the strength of intermolecular dipolar interactions and enhance the contribution of both electronic and nuclear dipolar flip-flops to the decoherence rate.^{7,16,19,29} However, notably, although T_2 decreases with increasing spin, the difference between **3** and **1** at 5 K is only a factor of ~ 2 . The small magnitude of the decrease allows the molecules possessing the largest spins to display coherence times within the microsecond regime, a relatively long-lived state. These results demonstrate that in the concentration regime appropriate for signal detection, spin magnitude can be varied without significantly compromising T_2 .

Comparison of the T_2 values for **4–6** elucidates the influence of SOC, the magnitude of which increases dramatically in the order $\text{Fe}^{\text{III}} < \text{Ru}^{\text{III}} < \text{Os}^{\text{III}}$. The magnitude of T_2 was expected to decrease in that order, owing to the fact that SOC mediates spin-lattice relaxation, a contributor to decoherence. However, the shortest T_2 value observed at 5 K is for **4**, followed by **5**, then **6** (see Table 2.1). This trend is the opposite of the expected dependence, and thus the operative

mechanisms for decoherence in **4–6** are not strongly dependent on variations in SOC. The T_2 of **1** supports this notion, as **1** exhibits the longest coherence time of the spin series despite having the greatest degree of SOC in that set. These results highlight the fact that one need not focus on low- ζ ions when synthesizing new electron spin qubits. Based upon these results, we

hypothesize that the primary driver of decoherence in these systems is the frequently implicated nuclear spin-based decoherence.^{7,8,11}

In order to validate the design principles set out above, we selected a species, $[\text{Ru}(\text{C}_2\text{O}_4)_3]^{3-}$, with substantial spin-orbit coupling, for evaluation as a qubit. The two conditions required for a successful electron spin qubit are the presence of a sufficiently long T_2 and the ability to place the potential qubit into any arbitrary superposition of its two constituent states. This property, known as coherent spin dynamics, is unusual and has only been observed in a small number of molecular species.^{13,18,19,30} Its existence is demonstrated by transient nutation experiments, in which an applied pulse of varying length, t_p , places the qubit into a specific superposition state determined by the pulse length. After a fixed delay much greater than T_2 , a two-pulse Hahn echo sequence is used to detect the echo intensity (see Figure 2.4).^{29,30}

If the molecule is viable as a qubit, the echo intensity will display a continuous, decaying oscillation (known as a Rabi oscillation) as the system cycles through superposition states.^{13,30b} As electron spin echo envelope modulation (ESEEM)²⁹ or cavity effects^{30a} can also impart oscillating

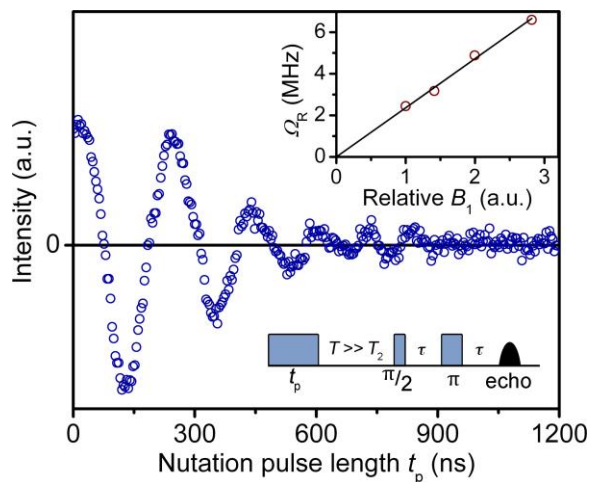


Figure 2.4 Rabi oscillations and pulse sequence for a solution of **1** at 5 K, $H_{\text{dc}} = 2812$ G, and relative B_1 of 2.0. Inset: Rabi frequency of oscillations from **1** as a function of the pulsed field strength relative to the lowest employed B_1 .

t_p dependence to the echo intensity, it is necessary to record nutation data at multiple pulse powers. The frequency of a Rabi oscillation, the Rabi frequency (Ω_R), will increase linearly with the pulsed field strength B_1 , in contrast to ESEEM, for which the frequency remains constant.²⁹ As shown in Figure 2.4, Fourier transforms of the oscillations of **1** recorded at multiple powers reveal a linear relationship between B_1 and Ω_R . Thus, the $M_S = -1/2 \leftrightarrow M_S = +1/2$ transition in complex **1** can be successfully placed into any arbitrary superposition, and the transition does, in fact, behave as an electron spin qubit. To our knowledge, this marks the first observation of Rabi oscillations in a second or third-row transition metal complex.

2.3 Conclusion

The foregoing study demonstrated via measurement of **1–6** that variation in spin and SOC is viable without significant impact on coherence time. One key advantage of electronic spin-based qubits is the ability to synthesize a single molecule containing multiple qubits by tuning zero-field splitting and spin. Since rational synthesis of molecules with a manifold of separately-addressable transitions relies upon careful synthetic tuning of spin and SOC, our results illustrate the viability of mononuclear transition metal molecules as QIP candidates. Observation of Rabi oscillations in a second-row transition metal complex further bolsters this conclusion. Taken together, these results provide a first step toward a set of guidelines for the future development of an electron spin-based molecular qubits. Future research will focus on the synthesis and measurement of nuclear spin-free mononuclear transition metal complexes, and quantifying nuclear spin-based decoherence.

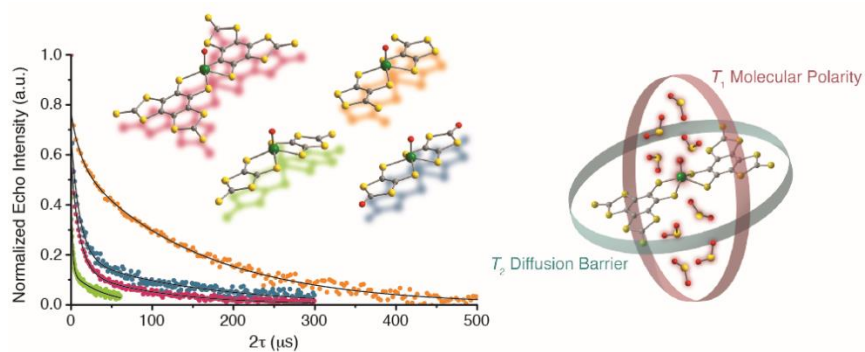
Chapter Three: Long Coherence Times in Nuclear Spin-Free Vanadyl Qubits

Reprinted with permission from:

Yu, C.; Graham, M. J.; Zadrozny, J. M.; Niklas, J.; Krzyaniak, M.; Wasielewski, M. R.;
Poluektov O. G.; Freedman, D. E. *Journal of the American Chemical Society* **2016**, *138*, 14678–
14685.

Copyright 2016 American Chemical Society.

This work was performed in collaboration with the co-authors listed above.



3.1 Introduction

Quantum information processing (QIP) is a powerful computational approach with the potential to revolutionize problem solving in fields ranging from cryptography to the modeling of quantum biological processes.¹⁻⁵ Implementation of QIP relies upon the manipulation of quantum bits, or qubits, that can be placed in a superposition of the binary states "0" and "1". Of the numerous approaches to creating qubits, one promising route employs pairs of electronic spin sublevels, M_S levels, in coordination complexes.⁶⁻⁸ These molecular electronic spin-based qubits are advantageous for two crucial reasons: their capacity for facile addressing via pulsed electron paramagnetic resonance (EPR) techniques and significant chemical tunability via synthetic chemistry.^{8,9} Further promise for electronic spin qubits resides in the prospect of coupling many such spin centers together within the same device.^{7,10-15} Notably, employing transition metals as the source of electronic spin confers two additional dimensions of scalability beyond that of radical-based systems: the potential to incorporate a multitude of M_S levels, and therefore qubits, within the same complex, and the capability of creating hybrid electronic spin nuclear spin-based qubits through the use of hyperfine transitions on a single transition metal.^{10,16-18}

The performance of a qubit system is described by two figures of merit: the coherence time (T_2), which is the time window of control for the qubit,⁸ and the spin-lattice relaxation time (T_1), which serves as an upper limit to T_2 and the inverse of which ($1/T_1$) determines the qubit operating speed.^{19,20} The primary challenge in the practical implementation of electronic spin-based qubits is slowing the collapse of the superposition state, a process known as decoherence or dephasing.^{7,11} The timescale of decoherence is parameterized by T_2 .¹¹ Enabling the rational synthesis of qubits relies upon creating specific design principles that allow chemists to rationally dial-in T_1 and T_2 values via chemical modification. While there are several powerful studies on qubit design,

including our own, there remain many parameters to be studied. Few studies have assessed the generality of qubit design principles discovered in these studies, necessitating significant further study to reveal universal design principles.^{21–28} The absence of synthetic insight lies at the heart of the challenge of constructing viable molecular qubits.

Fundamental investigations of design principles for qubits are optimally performed on $S = 1/2$ complexes, such as those of vanadium(IV), where there are a minimum number of convoluting variables. Further, employing vanadium as a qubit enables us to draw upon on the wealth of knowledge obtained via investigations of biological systems.^{29–31} Indeed, recent studies revealed enormous promise for these species as electron spin-based qubits.^{17,22,24,26,28,32–34} Of specific relevance to the studies described herein, one such complex, $[\text{V}(\text{C}_8\text{S}_8)_3]^{2-}$, exhibits a coherence time of 0.7 ms, unprecedented for molecular systems.^{17,32} This result rivals the performance of current state-of-the-art solid state qubits,^{35–38} and establishes the viability of coordination complexes as potential materials for QIP.

Demonstration of millisecond coherence times in molecular qubits propels the field forward towards preparing molecules amenable for device fabrication. Yet, as a nearly spherical molecule, $[\text{V}(\text{C}_8\text{S}_8)_3]^{2-}$ is ill-suited to this application. Progressing in that direction necessitates an additional design criterion, molecules that are compliant with deposition on surfaces. Note, that these molecules still require long coherence times, analogous to those observed in $[\text{V}(\text{C}_8\text{S}_8)_3]^{2-}$.¹¹ One class of vanadium-based qubits that can potentially satisfy these criteria is square-pyramidal vanadyl(IV) complexes. Indeed, previous elegant research demonstrated the confluence of room-temperature quantum coherence and surface compatibility in these complexes.^{22,33}

Marrying the surface compatibility of vanadyl(IV) complexes with the nuclear spin-free ligand field of $[\text{V}(\text{C}_8\text{S}_8)_3]^{2-}$ offers a pathway to creating long-lived surface-compatible qubits. However,

achieving this goal first requires establishing design principles governing T_1 and T_2 in vanadyl bis(dithiolene) qubits. We sought to both determine whether vanadyl-based qubits can display comparable times to vanadium tris(dithiolene) (hereafter notated as VS_6) qubits, and to determine the influence of ligand design on T_1 and T_2 in these species. For the first aim, we focused on creating an environment that simulates the nuclear spin-free environment of a future device.¹¹ The potential obscuring effect of large numbers of nuclear spins on subtle differences between complexes provides further impetus for removing nuclear spins from both the ligands and solvent. However, previous studies on VS_6 and vanadyl complexes largely employed nuclear spin-bearing solvents, as the only nuclear spin-free solvent that is a liquid under standard conditions is carbon disulfide (CS_2), which is highly nonpolar.^{22,24,32,34} This low polarity results in extremely low solubility for most charged molecular qubits. In order to circumvent this restriction, we investigated unconventional nuclear spin-free solvents and discovered significant promise in the polar solvent sulfur dioxide.³⁹ Note that although SO_2 is a gas under standard conditions, it readily liquefies at $-10^\circ C$. While SO_2 is not a glassing solvent, and can therefore engender aggregation (and hence, additional decoherence processes) of the solute, it nevertheless provides a nuclear spin-free matrix with which to study charged qubit complexes.

Creating design principles for surface-compatible vanadyl species relative to VS_6 species appears, upon initial inspection, to be a trivial modification. Yet there are two significant differences between the classes of compounds. The first relates to the structural change moving from an approximate octahedral geometry to a square pyramidal geometry. This causes spin-containing solvent nuclei to occupy different positions relative to the vanadium center in the two molecule types – an important consideration as environmental nuclear spins are frequently a main contributor to decoherence.^{19,25,32,40} The two configurations of the metal ion also alter the strength

of the molecule's vibrational coupling with the surrounding solvent molecules, which can affect T_1 . The second dramatic change is in the orbital containing the unpaired electron; in vanadyl complexes it is predominately $d_{x^2-y^2}$ in character, whereas in VS_6 complexes the orbital is predominately d_{z^2} in character.⁴¹⁻⁴⁵ This change modifies the extent of the electron delocalization from the metal center, potentially increasing interactions of the unpaired electron with the local environment, and therefore affecting decoherence and spin-lattice relaxation.⁴⁶ In the expansive EPR literature on both vanadyl and VS_6 complexes,^{42,47-53} there is a sole, recent investigation on the effect of substituting a vanadyl complex for the analogous VS_6 complex on T_2 and T_1 .²⁸ However, the scope of this study was limited to the examination of a single pair of complexes in the solid state and at relatively high concentrations. To rigorously develop future design principles and establish whether long coherence times in vanadium moieties are generalizable, a more expansive study probing a series of complexes in modular solution phase systems is required. Importantly, our utilization of the unique nuclear spin-free solvent SO_2 enables us to deconvolute the effect of local variables from the external matrix environment.

In order to address the dearth of design principles underlying vanadyl qubits and studies of processable qubits in spin-free environments, we report herein the synthesis and characterization of a series of vanadyl complexes with nuclear spin-free ligands in both spin-bearing solvents and SO_2 . Taken together with our group's previous investigation of an analogous series of four VS_6 complexes, this set of complexes offers insight into design criteria for future device-ready qubits.

3.2 Results and Discussion

To enable the clearest study, vanadyl complexes $(Ph_4P)_2[VO(C_8S_8)_2]$ (**1**), $(Ph_4P)_2[VO(\beta-C_3S_5)_2]$ (**2**), $(Ph_4P)_2[VO(\alpha-C_3S_5)_2]$ (**3**), and $(Ph_4P)_2[VO(C_3S_4O)_2]$ (**4**) were synthesized with the same set of nuclear spin-free carbon sulfide ligands previously employed in the analogous four

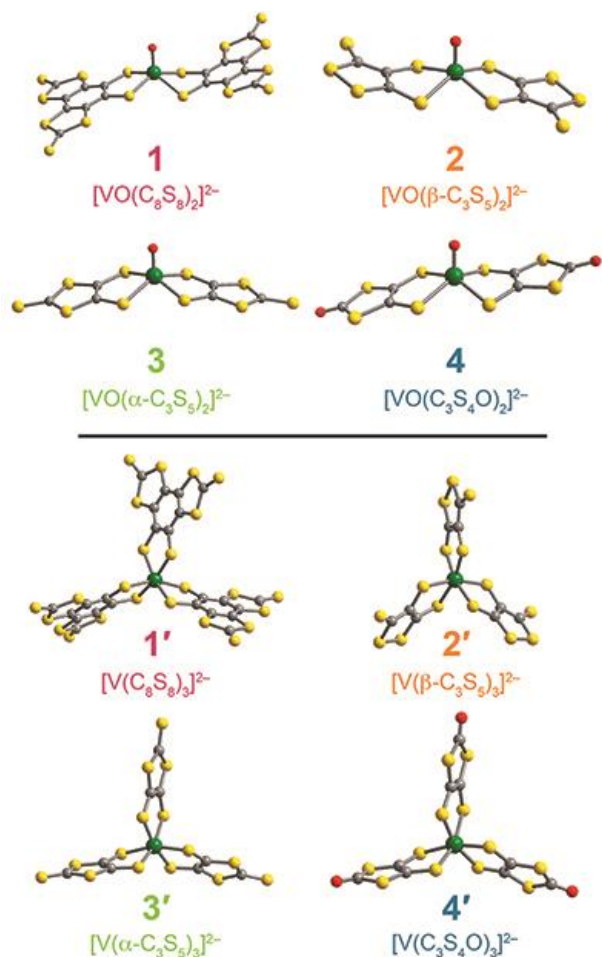


Figure 3.1 Molecular structures of the vanadyl complexes **1–4** (top half) and the analogous VS₆ complexes **1'–4'** (bottom half) synthesized in a previous report.³² Green, yellow, red, and gray represent vanadium, sulfur, oxygen, and carbon, respectively.

tris(dithiolene) complexes $(\text{Ph}_4\text{P})_2[\text{V}(\text{C}_8\text{S}_8)_3]$ (**1'**), $(\text{Ph}_4\text{P})_2[\text{V}(\beta\text{-C}_3\text{S}_5)_3]$ (**2'**), $(\text{Ph}_4\text{P})_2[\text{V}(\alpha\text{-C}_3\text{S}_5)_3]$ (**3'**), and $(\text{Ph}_4\text{P})_2[\text{V}(\text{C}_3\text{S}_4\text{O})_3]$ (**4'**) (Figure 3.1). All four vanadyl complexes possess a square pyramidal geometry around the vanadium center. Within the series, V=O bond lengths range from 1.599(4) Å to 1.605(3) Å, and V–S bond lengths range from 2.306(2) Å to 2.395(2) Å, comparable to those seen in other vanadyl complexes with thiolato sulfur donors.^{44,47,48,54,55}

We first sought to investigate differences in the extent of electron delocalization between the two series, as this may have important implications for qubit performance. To measure the hyperfine coupling across the vanadyl

series, and thereby probe the extent of electron delocalization away from the vanadium center, we performed continuous-wave (CW) EPR spectroscopy at X-band frequency (9.68 GHz) on 0.5 mM solutions of **1–4** (see Figure 3.2). The impact of differing nuclear spin environments was explored by measuring **1–4** in both 1:1 dimethylformamide:toluene (DMF:Tol) and 1:1 DMF-*d*₇:Tol-*d*₈. CW spectra for the complexes exhibit eight transitions corresponding to the $S = 1/2$ state coupling with the $I = 7/2$ ⁵¹V nucleus. Easyspin⁵⁶ was used to fit the spectra to quantify axial hyperfine coupling (**A**) and *g* parameters employing the Hamiltonian $\hat{H} = g\mu_B\mathbf{H}\mathbf{S} - g_N\mu_N\mathbf{H}\mathbf{I} + \mathbf{I}\mathbf{A}\mathbf{S}$, where *g*

is the axial g -tensor, μ_B is the Bohr magneton, \mathbf{H} is the magnetic field, \mathbf{S} is the electronic spin, g_N is the nuclear g -tensor, μ_N is the nuclear magneton, \mathbf{I} is the nuclear spin, and \mathbf{A} is the axial hyperfine coupling tensor. Modeling the spectra as axial systems yielded $g_{\parallel} = 1.971$ to 1.976 , $g_{\perp} = 1.989$ to 1.990 , $A_{\parallel} = 411$ to 418 MHz, and $A_{\perp} = 131$ to 132 MHz; these values are in accord with other vanadyl bis(dithiolene) complexes.^{28,49,50,53} Values of g and A were identical in the protiated and deuterated solvent matrices, indicating no significant change in molecular geometry as a function of solvent.

Averaged hyperfine tensor values for the vanadyl series of **1–4** fell within the narrow range of $\langle |A| \rangle = 224$ to 227 MHz. Values for the previous series of VS_6 compounds, which were fit assuming only positive signs of A_x , A_y , and A_z , showed complexes **2'–4'** in a similarly narrow range, $\langle |A| \rangle = 235$ to 248 MHz, while the low value of **1'** ($\langle |A| \rangle = 192$ MHz) served

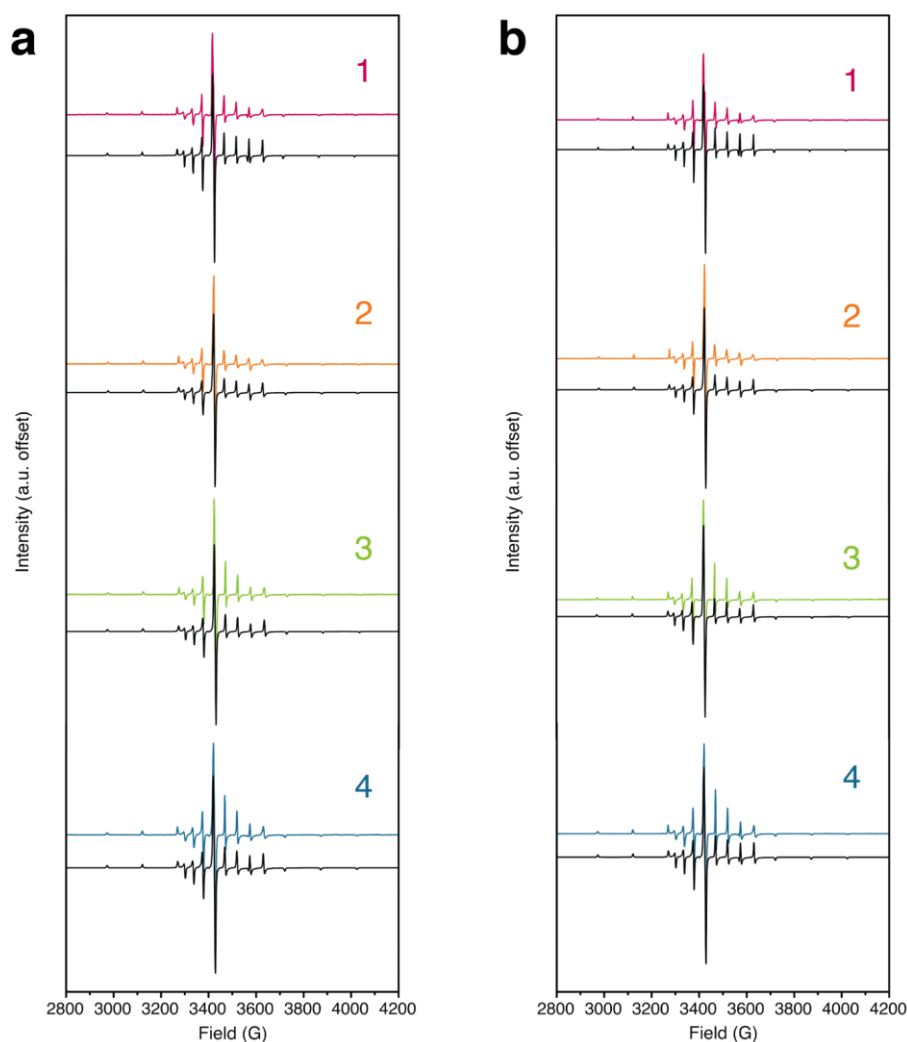


Figure 3.2 Continuous wave (CW) EPR spectra of **1–4** collected in (a) 1:1 DMF:Tol and (b) in 1:1 DMF- d_7 :Tol- d_8 at 100 K. Colored lines represent experimental data, and the fitted spectra are shown in the black lines.

as an outlier.³² The differences in $\langle |A| \rangle$ suggest that the unpaired electron in **1–4** may be more delocalized from the vanadium center than in **2'–4'**, but less so in **1'**. Conclusions on the amount of delocalization between **1–4** and **1'–4'** are complicated by the differing geometries, but the significant difference in $\langle |A| \rangle$ between **1'** and **2'–4'** allows for a direct comparison within the VS₆ series. Therefore, any differences in properties arising from different delocalization between **1–4** and **1'–4'** should also manifest between **1'** and **2'–4'**.

Our initial goal was to establish whether the same design principle of a nuclear spin-free ligand field is viable within vanadyl complexes. Here, the absence of a large ligand shielding the metal center from solvent interactions, coupled with the increased electron delocalization into the ligand field, led us to ask whether the coherence times of **1–4** would be comparable to those observed in VS₆ complexes. Therefore we endeavored to measure **1–4** in a nuclear spin-free solvent. Predictably, our attempts to solubilize the vanadyl complexes in CS₂ were unsuccessful, which we attribute to the complexes' 2- charge and the low polarity of CS₂. Indeed, these challenges are likely the reason so few molecular qubit candidates are measured in this convenient solvent. We circumvented the solubility problem by utilizing SO₂, a polar nuclear spin-free molecule, as a solvent, the same solvent employed in previous study of ours.³⁹ To the best of our knowledge, this is the only previous report of the use of SO₂ as a solvent for candidate qubits.

Hahn echo experiments performed on the central resonance of 0.13 mM solutions of the complexes in SO₂ at 10 K yielded coherence times, extracted from the long component of the biexponential fit, of 40(1) to 152(6) μ s, with the highest values observed in **2** (151(2) μ s) and **4** (152(6) μ s) (Figure 3.3). These coherence times are among the longest observed in molecular qubits, eclipsed only by (Ph₄P-*d*₂₀)₂[V(C₈S₈)₃] in CS₂.³² Note that the biexponential decay character suggests the presence of two distinct decoherence processes. Here, we attribute the faster

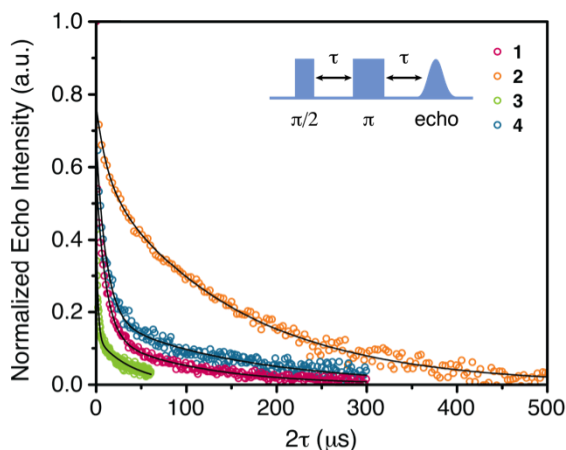


Figure 3.3 Normalized Hahn echo decay curves of **1–4** in SO_2 at 10 K. The black lines correspond to biexponential fits of the data. The pulse sequence of the Hahn echo experiment is shown.

relaxation process to electron spin-electron spin coupling caused by aggregation of the complex or counter-ions, and the slower process to nuclear spin diffusion. Aggregation induces decoherence by increasing the proximity of the complexes, and hence the electronic spins, to each other, allowing neighboring spins to mutually interfere.

Frozen SO_2 is not a glass, and therefore

readily provides opportunities for aggregation along the numerous crystalline grain boundaries of the frozen solvent matrix.³² While the non-glassing behavior certainly is not ideal, the T_2 values extracted from the slow relaxation process nevertheless provides a measure of the intrinsic coherence times of **1–4** in nuclear spin-free environments. Even when the fast process for each of the species is neglected, the T_2 values of the vanadyl complexes at 10 K remain several orders of magnitude lower than T_1 . We attribute the observation that T_2 is not T_1 -limited to the nuclear spins of the non-deuterated Ph_4P^+ cations, which remain a source of protons in the otherwise proton-free environment. Note, Ph_4P^+ also contains ^{31}P which provides a second source of nuclear spin. Despite the promotion of decoherence by both proximal nuclear spins and complex aggregation, T_2 values for these systems are nearly two orders of magnitude longer than those observed for all previous measurements of molecular vanadyl qubits. This measurement in SO_2 enables us to fully isolate these molecules from adjacent nuclear spins, thereby enabling the realization of coherence times that are substantially longer than those observed in the solid state.²⁸ These results

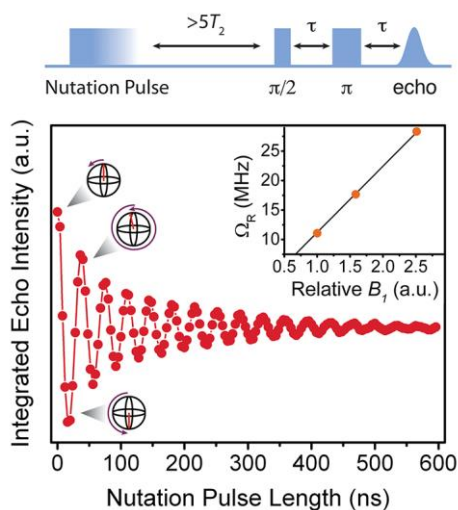


Figure 3.4 Nutation experiment performed on **1** in 1:1 DMF-*d*₇:Tol-*d*₈ showing Rabi oscillations that demonstrate the capability of the complex to be placed in any arbitrary superposition between the $M_S = -1/2$ and $M_S = +1/2$ spin states. The spin orientation as a function of pulse length is depicted alongside the nutation data. A diagram of the pulse sequence used for nutation measurements is shown above. A linear dependence is observed between the Rabi frequency and the pulsed field strength.

demonstrate that extraordinary coherence times are attainable in vanadyl complexes in SO₂ and the utility of SO₂ as a polar, nuclear spin-free solvent for future studies – both our own and those of the community at large.

In light of the results above, we performed nutation experiments to determine whether **1–4** can be placed into any arbitrary superposition of states. Demonstration of this capability establishes a candidate molecule’s viability as a qubit. Nutation experiments can also quantify the gate time for the simplest

logic gate: a NOT gate. Toward those ends, a variable length microwave pulse (a nutation pulse) was applied to 0.5 mM solutions of the complexes in both 1:1 DMF:Tol and 1:1 DMF-*d*₇:Tol-*d*₈ at the central resonance, followed by a two-pulse sequence to generate an echo that detects the turning angle. Because the applied magnetic field quantizes the alignment of the spin into two discrete states, denoted down ($M_S = -1/2$) and up ($M_S = +1/2$), any spin alignment that deviates from one of these states constitutes a superposition of the two states. A viable qubit will display a continuous decaying oscillation (Rabi oscillation) of echo intensity as the qubit cycles through all possible superposition states.^{57,58} We observe in our system of vanadyl complexes this decaying oscillation as the nutation pulse length increases (Figure 3.4). Note that nuclear spins and cavity effects⁵⁹ can also contribute oscillations to the echo intensity. These contributions necessitate measuring the Rabi frequency at multiple pulsed field strengths, as the frequency of true nutations

is linearly proportional to the pulsed microwave field strength (B_1) for true Rabi oscillations. The unique Rabi frequency extracted from these measurements has also been used in quantum sensing applications as a mechanism of probing the local environment.⁶⁰ Fourier transforms of the Rabi oscillations for **1–4** at different pulsed fields in 1:1 DMF:Tol and 1:1 DMF- d_7 :Tol- d_8 yield Rabi frequencies of 9.8 to 29.8 MHz. Within the series of compounds, spin-flip times, corresponding to NOT gates, ranged from 17 to 53 ns. Crucially, a linear relationship is present between the Rabi frequency and B_1 , which demonstrates these oscillations can be attributed to quantum control, not nuclear spins or cavity effects (Figure 3.4). These data confirm our candidate qubits can be placed into any arbitrary superposition, establishing them as qubits.

With a demonstration that these species display coherence times suitable for implementation and Rabi oscillations, we further sought to investigate the design principles underlying vanadyl qubits. Enabling the directed synthesis of further vanadyl qubits necessitates creating design principles beyond that of nuclear spin-free ligand environments. Towards that end, we investigated the spin-lattice relaxation times (T_1) of **1–4** via pulsed EPR. Spin-lattice relaxation is the phonon-mediated electronic spin transition from the excited to ground Zeeman energy levels. The degree to which phonons contribute to spin-lattice relaxation depends on a number of factors, including vibrational modes of the molecule and its local environment, the presence or absence of low-lying excited states, and the spin-orbit coupling of the unpaired electron.¹⁹ T_1 therefore serves as a sensitive probe of both the molecule's intrinsic properties and its interaction with the local environment.

Acquisition of T_1 data first proceeded by inversion recovery experiments on 0.5 mM solutions of **1–4** in 1:1 DMF:Tol from 10 K to 140 K. All experiments were performed at the highest intensity central resonance in the EPR spectrum. At 10 K, T_1 for **1–4** ranges from 16.29(8) to

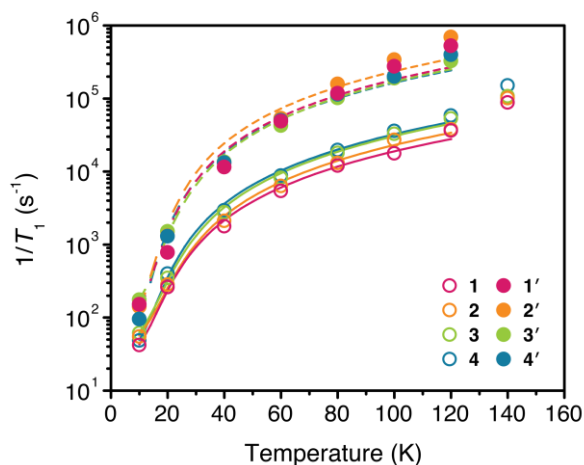


Figure 3.5 Spin-lattice relaxation rates ($1/T_1$) of **1–4** (open circles) as a function of temperature in 1:1 DMF:Tol. Closed circles correspond to the previously-measured series **1'–4'**. The magnitude of T_1 for **1–4** is approximately half to one order of magnitude larger than those observed in **1'–4'** across the entire temperature range. Solid lines represent the fits to **1–4** from 10–120 K, and the dotted lines represent the fits to **1'–4'**.

23.8(2) ms and rapidly decreases with increasing temperature, ultimately reaching 6.62(5) to 11.38(8) μ s at 140 K. Values of $1/T_1$ for **1–4** are depicted alongside those of **1'–4'** in Figure 3.5. Interestingly, we found the magnitudes of the T_1 values for **1–4** to be one-half to one order of magnitude larger than those observed in **1'–4'** across the entire temperature range measured. This disparity is similar to that observed by Sessoli and coworkers in their recent comparative study.²⁸

Within the vanadyl **1–4** series, the T_1 values are nearly identical, demonstrating that different ligands within the series do not appreciably impact T_1 . This mirrors the previous measurements on **1'–4'**, which demonstrated a similar lack of T_1 ligand-dependence. In addition, very similar T_1 values were obtained with **1–4** in DMF- d_7 :Tol- d_8 , indicating that the change in lattice phonon modes caused by deuteration has a negligible effect on spin-lattice relaxation, as previously noted.⁶¹

Elucidating the key molecular differences in **1–4** and **1'–4'** that result in this dramatic change in T_1 is critical to understanding how to tune this parameter. We focused our attention onto the contribution of various phonon-mediated processes to spin-lattice relaxation by examining the temperature dependence of T_1 . Low-energy vibrational modes dissipate the energy released during electronic spin-lattice relaxation. Two such low-energy phonon-mediated processes that contribute significantly to T_1 at low temperatures in a variety of vanadium(IV) complexes are the direct and

Raman processes.^{62,63} The first of these, the direct process, is a very low energy process that occurs via emission of a phonon corresponding to the energy of the spin-flip relaxation. It is typically dominant at temperatures below 20 K. The Raman process is a two-phonon process, analogous to the Raman scattering of light, in which the difference between the energies of the absorbed and emitted phonons is equal to the energy of the spin-flip transition. In the Raman process, the excited virtual state must correspond to an energy less than the Debye temperature, which is typically on the order of 100 K for frozen solvent glasses; it is therefore typically dominant at < 100 K in these systems.^{62,63}

Fitting of the temperature dependence of T_1 confirms that the Raman process in **1'**–**4'** possesses a coefficient approximately 10-fold higher than that of **1**–**4**, and is therefore responsible for the majority of the difference in T_1 between the two series. Further, fitting the Debye temperature yields similar values of 112 to 127 K between the two series, which confirms that the Debye temperature does not contribute to the difference in T_1 .⁶² As the contribution of the Raman process to T_1 is governed by low-frequency vibrational modes involving the spin center,^{61,64} the differing Raman coefficients indicate that a difference in the vibrational environment around the vanadium center is the underlying cause of the T_1 disparity.

Supporting our hypothesis, multiple studies note that measuring the same species in increasingly polar solvents yields increasing values of T_1 .^{61,64} Such results suggest that the local molecular environment may be more important in determining the relevant vibrational environment than specific bonds within the complex. Specifically, previous T_1 studies of **1'**–**4'** note that as the solvent polarity increases from DMF:Tol to butyronitrile:DMF, T_1 of all the complexes increases at least two-fold.³² To test the impact of solvent polarity in this vanadyl system, we conducted a variable-temperature T_1 solvent dependence study with complex **4** in 4:1

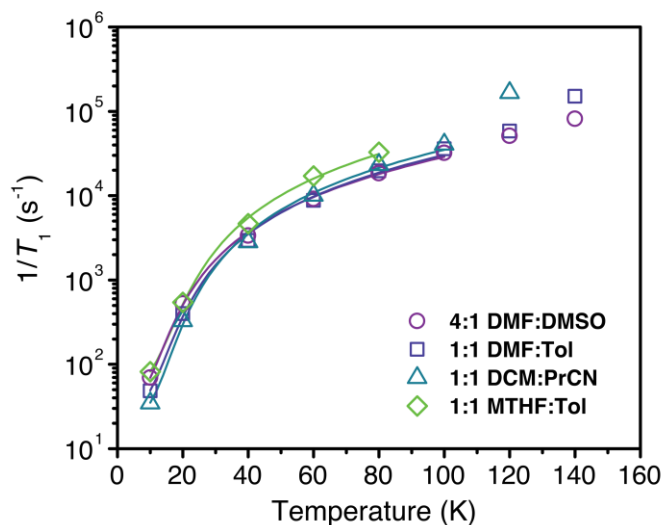


Figure 3.6 Variable-temperature spin-lattice relaxation rates ($1/T_1$) of **4** measured in 0.5 mM solutions of the complexes in 4:1 DMF:DMSO, 1:1 DMF:Tol, and 1:1 DCM:PrCN, and a saturated solution in 1:1 MTHF:Tol. Solid lines represent the fits to the data from 10–100 K except for the 1:1 MTHF:Tol system, which was fit from 10–80 K.

DMF:dimethylsulfoxide (DMSO), 1:1 dichloromethane (DCM):butyronitrile (PrCN), and 1:1 2-methyltetrahydrofuran (MTHF):Tol (Figure 3.6). Fitting the temperature dependence of T_1 yielded coefficients for the Raman process that increased by a factor of 2 from the most polar solvent, DMF:DMSO, to the least polar, MTHF:Tol. Based on these results, we propose that vanadyl complexes, which are distinctly more polar than their VS_6

analogues, interact more strongly with the solvent matrix. In addition, the presence of the bare oxygen atom may enable stronger interactions with surrounding DMF molecules. We argue that this strong vibrational coupling serves to directly rigidify the spin center in **1–4** with respect to its local environment and suppresses the low-energy molecular vibrations that diminish T_1 . We therefore propose the design principle that polarity of the vanadyl complex enables the longer T_1 observed in **1–4** over **1'–4'**.

There are suitable alternate explanations, which we discount for the following reasons. In principle, differences in electron delocalization between the two series may explain the increase in T_1 on moving from VS_6 to vanadyl. Here, such differences could lead to dissimilar interactions with the solvent matrix. As noted above, however, if this were a contributing factor, one would expect a significant difference between the T_1 value of **1'** and those of **2'–4'** — a difference that is not observed. Thus, these data suggest that the range of electron delocalization onto the ligands

observed in **1–4** and **1'–4'** does not have a significant effect on the spin-lattice relaxation time.

Another well-documented contributor to spin-lattice relaxation rate is spin-orbit coupling, which couples lattice vibrations (phonons) to the electron spin.¹⁹ Indeed, increasing spin-orbit coupling, which can be parametrized by g -anisotropy ($\Delta g = |g_{\parallel} - g_{\perp}|$), directly correlates with decreasing T_1 values.^{61,63,65} While a recent study suggested the difference in T_1 between VS₆ and vanadyl species may be attributed to the differences in spin-orbit coupling,²⁸ our investigation suggests the difference in g -anisotropy across the series of eight molecules is insufficient to generate this disparity in T_1 . Analysis of Δg in both sets of molecules yielded values that span from 0.015 to 0.019 for **1–4** and 0.019 to 0.031 for **1'–4'**. Between pairs of analogous vanadyl and VS₆ complexes (e.g. **1** vs. **1'**, **2** vs. **2'**, etc.), the differences in g -anisotropy ($|\Delta g_{\text{vanadyl}} - \Delta g_{\text{VS}_6}|$) spanned 0.003 to 0.013. Differences in g -anisotropy of a similar magnitude in vanadium(IV) complexes in a previous study correlated with a factor of 2 to 4 variation in T_1 , and was not determined to be a major contributor to spin-lattice relaxation.⁶² Here, we observe a much larger factor of 3 to 10 difference in T_1 between analogous members of the two series. Further, we note a lack of discernable trend in T_1 from variation of Δg within each series. Thus, on the basis of these data, we conclude that the observed differences in spin-orbit coupling are not the origin of the large difference in T_1 between the series.

Another possibility we considered is whether changes in T_1 can be attributed to a specific local vibrational mode. Indeed, when we initiated this investigation we believed that could be a source of decoherence, and performed spectroscopic measurements to search for such a mode. Our fits of the EPR data to a Raman process suggest that the energy scale of the identifiable local modes such as the vanadyl oxo stretch is of too high to influence the observed T_1 disparity. The phonon modes involved in the Raman process possess energies less than the Debye temperature, and for our

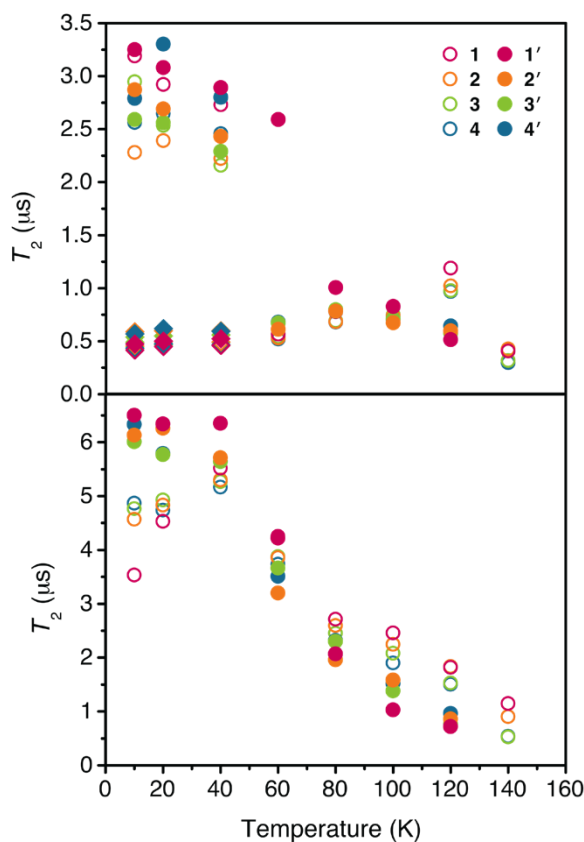


Figure 3.7 Decoherence times (T_2) as a function of temperature in 1:1 DMF:Tol (top) and 1:1 DMF- d_7 :Tol- d_8 (bottom). Open symbols correspond to **1–4**, while the closed symbols correspond to **1'–4'**. Diamond symbols correspond to the fast process in the biexponential fits.

systems the maximum phonon energies are approximately 83 cm^{-1} . As noted previously, the stretching modes associated with a vanadyl oxo are $\sim 980\text{ cm}^{-1}$, whereas those of V–S are approximately 400 cm^{-1} .^{44,52,54} The energies of these stretching modes far exceed the range expected for the Raman process in the temperature range studied, and are not expected to contribute significantly to T_1 relaxation. Based on these observations, we conclude that although vibrations involving atoms of the first coordination sphere are

likely involved in the collective modes, which influence T_1 at these temperatures, it is unlikely that the energies of the specific bond

stretching modes are the root cause of the observed T_1 difference between the two series. While a previous study cited these bond stretching frequencies as the source of T_1 differences between vanadyl and VL₃ complexes in crystalline matrices, we suggest our proposed local environment rigidity concept is also applicable to these systems.²⁸ The compact packing of the vanadyl complex, with the O–H dipole interactions with the nearby cations, may concertedly engender higher energy phonon modes that do not participate in spin-lattice relaxation, thereby lengthening T_1 in vanadyl complexes.

Following the creation of a new design principle for long T_1 values in these vanadyl species,

we proceeded to investigate the lifetimes of the spin superposition states (T_2). To obtain T_2 values, Hahn echo decay curves were collected at the central EPR resonance of 0.5 mM solutions of **1–4** in both 1:1 DMF:Tol and 1:1 DMF- d_7 :Tol- d_8 from 10 to 140 K. Coherence times were extracted from these data by fitting the decay curves with stretched or biexponential functions, and the T_2 values are plotted alongside those of **1'–4'** in Figure 3.7. In 1:1 DMF:Tol, the coherence times of **1–4** are nearly identical to those of **1'–4'**, reaching 3.2(2) μs at the lowest temperatures. We note that **1–4** exhibit distinctly biexponential decay curves in DMF:Tol below 40K, similar to **1'–4'**. This implies the presence of two separate populations of spins, each subject to a distinct set of decay processes. As the temperature increases, the curve shape is better fit by a stretched exponential function, and there is a concerted drop-off in T_2 at 60 K. A notable difference between the two series occurs at 120 K, where the T_2 values of **1–4** rise while those of **1'–4'** decrease.

In the deuterated solvent mixture, a difference is observed between the two series below 40 K, with **1–4** displaying T_2 parameters from 3.5(2) to 4.87(8) μs at 10 K, between 1.2 and 3.0 μs shorter than the corresponding species in **1'–4'**. Furthermore, the biexponential behavior is notably absent for both series, as the echo decays are well fit to a stretched exponential function. Above 40 K, both series demonstrate similar temperature dependences in T_2 , and exhibit the same concerted drop in T_2 at 60 K observed in the protiated solvent matrix.

Inspection of these data reveals crucial insight into factors governing the relative qubit performance of these two sets of compounds. Specifically, the role of methyl rotation on the rate of decoherence may be an important factor to account for in this system. At low temperature, the biexponential behavior for both **1–4** and **1'–4'** is absent in the deuterated solvent, suggesting contributions from methyl group tunneling rotation at low temperatures in 1:1 DMF:Tol. As the temperature increases, the concerted drop in T_2 at 60 K in both solvent systems can be attributed

to increased decoherence from the onset of classical methyl rotation occurring on the timescale of the T_2 measurement.⁶⁶ Finally, as the temperature is further increased to 120 K, the increase in T_2 of **1–4** is can be ascribed to the methyl rotation timescale becoming much shorter than the experimental timescale. This phenomenon causes coupling to individual protons on the methyl group to be averaged out and their contribution to decoherence to diminish.^{19,61} Such behavior would also likely occur in **1'–4'** were it not for the significantly lower T_1 ; at 120 K, T_2 for the VS₆ series is virtually identical to that of T_1 , meaning that T_2 is T_1 -limited. T_1 limitation also occurs in the vanadyl species; however it occurs at a temperature that is ~20 K higher, causing T_2 to drop significantly between 120 and 140 K.

Though methyl rotation explains the difference in behavior between solvent systems, it does not address the low-temperature discrepancy in T_2 between **1–4** and **1'–4'**. To explain this difference, the concept of a nuclear spin diffusion barrier must be invoked (Figure 3.8). Nuclear spins within a given distance of an electronic spin center exhibit dipolar coupling to the electron spin. When strong enough, this coupling impedes the rapid spin flips that induce decoherence. The volume in which dipolar coupling enables the slowing of spin flips is defined by the so-called nuclear spin diffusion barrier. The radius of this barrier around an electronic spin is typically estimated as 3–10 Å in protiated environments.^{19,66} Transitioning from a protiated to a deuterated environment

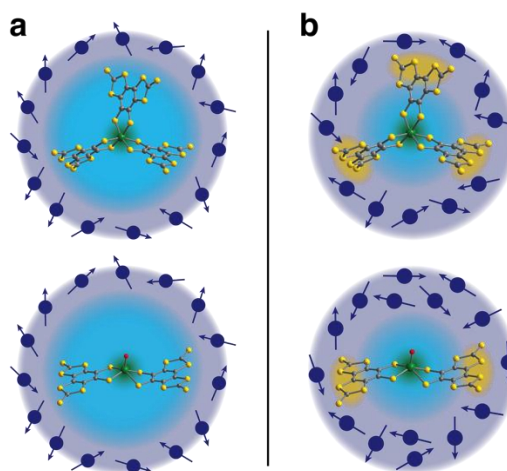


Figure 3.8 Proposed model of the spin diffusion barrier of **1** and **1'** in (a) 1:1 DMF:Tol and (b) 1:1 DMF-*d*₇:Tol-*d*₈. The light blue region depicts the extent of the spin diffusion barrier, while the light purple region indicates the region containing nuclear spins that contribute to decoherence. The yellow regions portray regions of space where the nuclear spin-free ligand displaces decoherence-active solvent spins. In the deuterated solvent, the replacement of a C₈S₈²⁻ ligand with an oxo results in more solvent deuterons in close proximity to the electron spin that contribute to decoherence.

contracts the diffusion barrier around an electronic spin. The smaller deuterium magnetic moment engenders weaker dipolar coupling with the electronic spin, thereby diminishing the spatial extent to which spin flips are suppressed and hence the radius of the diffusion barrier.

We therefore propose that in a protiated environment, all of the ligands are located entirely within the barrier radius (Figure 3.8a). Hence, replacing one ligand with an oxo does not alter the quantity of nuclear spins contributing to decoherence. However, in a deuterated environment, the barrier radius shrinks, and the ligands protrude into the decoherence-active portion of the spin bath (Figure 3.8b). Removing one ligand in a deuterated environment causes decoherence-active solvent deuterons to replace the nuclear spin-free ligand; these contribute to decoherence, resulting in a shorter T_2 . Such a model implies that the greatest difference in T_2 between analogous members of the two series should be observed between the two species with the largest ligand, **1** and **1'**, which is indeed consistent with our results. Thus, while the oxo bond may improve molecular polarity and consequently augment T_1 , the absence of the third nuclear spin-free ligand is detrimental to T_2 . The use of multiple bulky, nuclear spin-free ligands is therefore established as a novel design parameter for enhancing T_2 in molecular qubits.

3.3 Conclusion

The foregoing results illustrate the impact of ligand field and electronic structure considerations on the performance of two analogous series of vanadium-based complexes as electronic spin-based qubits. The significant enhancement of T_2 observed in SO₂ vs. deuterated solvents highlights the criticality of a nuclear spin-free environment, and demonstrates the utility of SO₂ as a nuclear spin-free solvent for future studies. Importantly, the realization of long T_2 values here highlights the promise of obtaining exceptionally long T_2 parameters in species that may readily assemble on surfaces. Our systematic study of **1–4** and **1'–4'** critically emphasizes the

role of solute-solvent interactions in T_1 , and suggests the polarity of a complex as an important design parameter. This is a novel design parameter for transition metal-based molecular qubits, and may lead to new directions in qubit synthesis, wherein alternative ligand sets to nonpolar carbon-sulfide structures are favored. Importantly, this work reinforces the importance of the spin diffusion barrier in determining T_2 , meriting future studies on the exact extent of the barrier in vanadium-based qubits. Questions remain whether these same models, which arise from solution measurements, hold true for molecules appended to surfaces. Future studies will indeed be required to answer such questions.

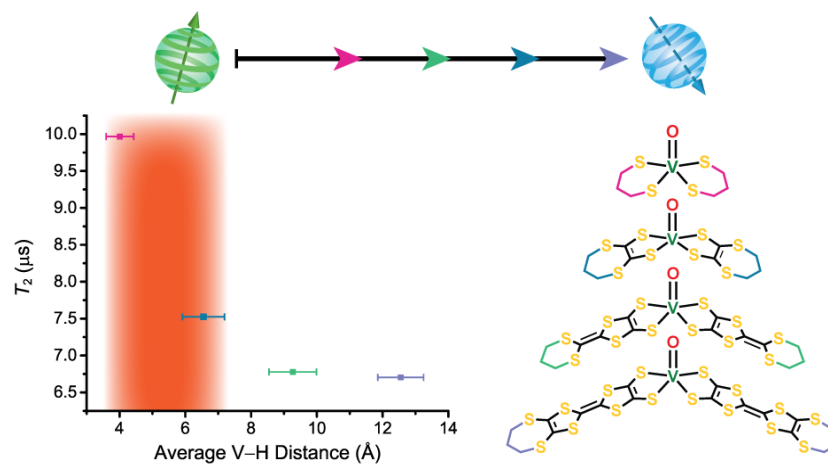
Chapter Four: Synthetic Approach to Determine the Effect of Nuclear Spin Distance on Electronic Spin Decoherence

Reprinted with permission from:

Graham, M. J.; Yu, C.; Krzyaniak, M.; Wasielewski, M. R.; Freedman, D. E. *Journal of the American Chemical Society* **2017**, *139*, 3196–3201.

Copyright 2017 American Chemical Society.

This work was performed in collaboration with the co-authors listed above.



4.1 Introduction

The interplay of electronic and nuclear spins creates unique fingerprints within electronic paramagnetic resonance (EPR) and nuclear magnetic resonance (NMR) spectra. As two illustrative examples, in biological EPR, the interaction between electronic and nuclear spins has been harnessed to provide insight into biochemical processes,^{1,2} while in silicon carbide systems, it enables a crucial process known as coherence transfer.³ Understanding the complex interaction between electronic and nuclear spins could illuminate important processes across a range of fields. Within the realm of electronic-nuclear spin interactions, our interest resides in studying the effect of nuclear spin interactions on electronic spin coherence. Flipping of weakly coupled nuclear spins induces the loss of information stored within electronic spins in a process known as decoherence.⁴ There is a paucity of studies probing the effect of nuclear-electronic interspin distance on the characteristic timescale of electronic spin coherence, T_2 . Of vital interest to us, creating new knowledge within this area will advance the burgeoning area of electronic spin-based quantum information processing (QIP). QIP is a revolutionary approach to computation which requires long values of T_2 .⁵⁻⁸ Designing complexes that exhibit long coherence times necessitates an understanding of precisely how the position of nuclear spins relative to the electronic spin center affects decoherence. However, the lack of synthetic studies elucidating this positional dependence currently inhibits the rational design of long-coherence complexes.

Of the numerous candidates for qubits, the smallest unit of information in QIP, electronic spin offers considerable advantages, including its inherent quantum nature and ability to be placed into superposition states via the use of pulsed microwaves.^{4,9-13} Yet, in comparison with other qubit candidates, electronic spins suffer from short values of T_2 . For a quantum object to be viable as a qubit, it must exhibit a T_2 value on the order of 10^4 times the duration of a simple computational

operation, which for electronic spin is ~ 10 ns.¹⁴ Thus, to be viable, electronic spin qubits require coherence times of > 100 μ s. Despite a few notable exceptions within molecular and solid-state compounds,^{15–22} the vast majority of electronic spin-based qubits exhibit T_2 values in the sub-10 μ s regime.²³

Designing new molecules and materials with long coherence times necessitates a clear set of design principles. Chief amongst those design principles, as noted above, is the relationship between nuclear-electronic interspin distance and coherence times. While the necessity of understanding this relationship would be obviated by simply removing all nuclear spins from the electronic spin environment, such as in isotopically purified diamond,²⁴ there are only a limited number of species for which this strategy will be effective.

Creating new design principles requires careful consideration of the impact of nuclear spin on electronic spin coherence. Although nuclear spin diffusion is driven by dipolar coupling between the electron and environmental nuclei, it does not exhibit a simple r^{-3} dependence. Instead, there exists a critical radius, known as the spin diffusion barrier radius, inside of which nuclei are so strongly coupled to the electron spin that they do not undergo flip-flops on the experimental timescale, and therefore do not contribute to decoherence.²³ Effectively, the diffusion barrier creates two regimes, within the spin diffusion barrier and significantly distal from electronic spin center, wherein nuclear spins do not shorten T_2 . One could therefore envision crafting molecules that, despite containing spin-active nuclei, are designed such that the spin-active nuclei do not contribute to decoherence.

The idea of a diffusion barrier radius (sometimes also referred to as a "frozen core")²⁵ was first postulated in 1949,²⁶ and initially observed directly in 1973 via analysis of nuclear relaxation rates of protons near a Yb^{3+} impurity in a crystal of $\text{Y}(\text{C}_2\text{H}_5\text{SO}_4)_3 \cdot 9\text{H}_2\text{O}$.²⁷ This and other reports

on solid-state systems assign the radius as lying between 3 and 10 Å from the metal center.^{25,27–30}

However, the radius is highly system-dependent, and specific systems such as phosphorus donors in natural-abundance silicon can exhibit radii of upwards of 50 Å.³¹ Studies of molecular species established a similar range of barrier radii to those of most solid-state systems (between 4 and 10 Å) by methods including time-resolved polarized neutron scattering³² and fitting T_2 data with a model incorporating a diffusion barrier.^{28,33} Notably, thus far, there are no synthetic studies of the diffusion barrier radius. There is, however, ample current research focused on theoretical models of the behavior of nuclear spins in systems exhibiting a barrier radius,^{31,34,35} offering promise for the future synergy of theory with our experimental results.

We aimed to address the lack of synthetic studies by designing a series of systems with a range of electron-nuclear distances and examining the effect of that variation on decoherence. Specifically, we targeted a series of coordination complexes based on the $S = 1/2$ vanadium(IV) ion. We selected the V^{4+} species based upon significant previous work demonstrating long coherence times and coherences up to room temperature, recommending such species as candidates for rigorous studies of coherence times.^{15,36–43} Herein we report the synthesis of a family of four novel vanadium(IV) complexes with a nuclear spin-bearing propyl bridge spaced at controlled distances from the metal center. Within this series, each complex was designed to possess a narrow, discrete range of electron-proton distances. Our results demonstrate that the diffusion barrier radius lies between 4.0(4) and 6.6(6) Å in the studied complexes. This result paves the way for the design of future nuclear spin-containing, long-coherence molecules.

4.2 Results and Discussion

We sought out a series of compounds whereby it would be possible to systematically vary the separation between an electronic spin-bearing metal and a set of nuclear spin-bearing atoms. The

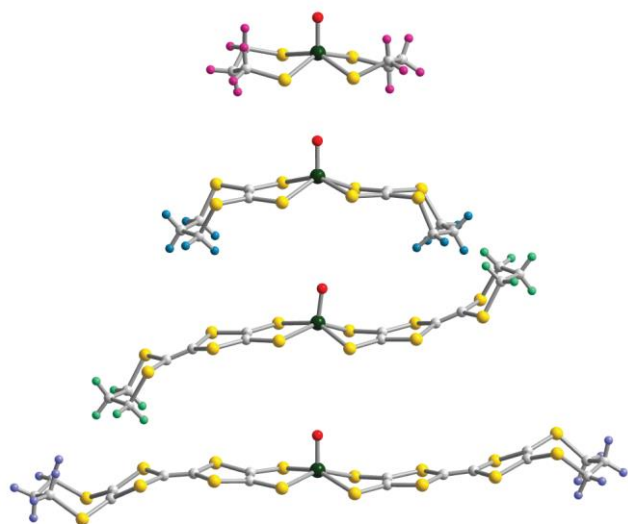


Figure 4.1 Crystal structures of the anionic complexes of **1–4**. Dark green, yellow, red, and grey spheres represent vanadium, sulfur, oxygen, and carbon, respectively. Protons are colored pink in **1**, blue in **2**, light green in **3**, and purple in **4**.

vast literature on conjugated carbon-sulfide ligands for organic conductors^{44,45} enabled us to identify a series of ligands with which we could accomplish this goal by spacing an alkyl bridge at specific distances from an electronic spin. The nuclear spin-free nature of the carbon-sulfide ligand backbone (98.9% and 99.3% natural abundance of spin-free isotopes for C and S, respectively) and the high modularity of this chemistry facilitated the rational synthesis of these species.

Employing this ligand motif, we synthesized four new vanadium(IV) complexes: $(\text{Ph}_4\text{P})_2[\text{VO}(\text{C}_3\text{H}_6\text{S}_2)_2]$ (**1**), $(\text{Ph}_4\text{P})_2[\text{VO}(\text{C}_5\text{H}_6\text{S}_4)_2]$ (**2**), $(\text{Ph}_4\text{P})_2[\text{VO}(\text{C}_7\text{H}_6\text{S}_6)_2]$ (**3**), and $(\text{Ph}_4\text{P})_2[\text{VO}(\text{C}_9\text{H}_6\text{S}_8)_2]$ (**4**) (Figure 4.1). Each complex was carefully designed to house propyl linkers (each containing 6 protons) at a specific distance from an $S = 1/2$ vanadium(IV) ion (Figure 4.2). The combination of the improved solubility enabled by the propyl unit relative to species containing the analogous ethyl-bridged ligands,⁴⁶ and the propyl moiety's six spin-active protons recommended it as the nuclear spin-bearing component. Further, the magnitude of the nuclear spin of ^1H ($\mu = 2.79 \mu_{\text{N}}$ for ^1H , 99.99% natural abundance) is unusually large relative to other elements on the periodic table, for example ^{35}Cl ($\mu = 0.82 \mu_{\text{N}}$) or ^{14}N ($\mu = 0.40 \mu_{\text{N}}$),⁴⁷ making it an ideal choice. The aforementioned modularity of the carbon-sulfur scaffold allowed placement of the propyl linkers at well-defined locations, yielding average V–H distances of 4.0(4) Å for **1**, 6.6(6) Å for **2**, 9.3(7) Å for **3**, and 12.6(7) Å for **4**.

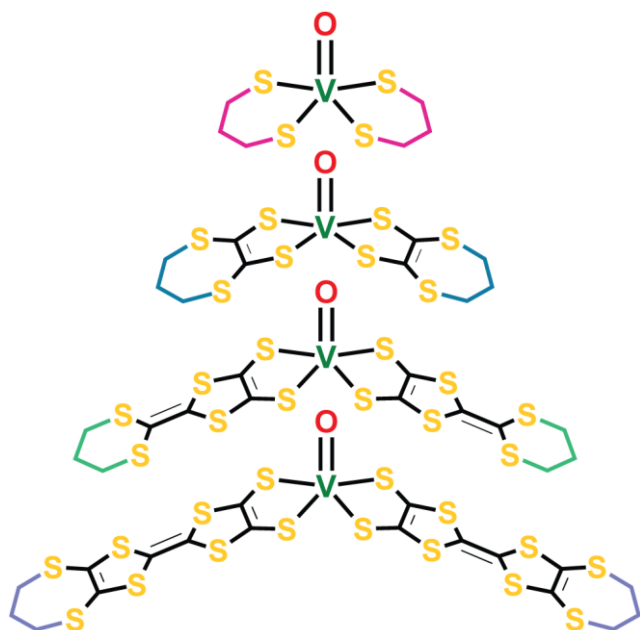


Figure 4.2 Schematic drawing of the four complexes employed in this study showing the functional components of the ligand design. The electronic spin-bearing vanadium center is highlighted in dark green, while the propyl linker with its six spin-active protons is depicted in variable colors (pink for **1**, blue for **2**, light green for **3**, and purple for **4**).

The vanadyl coordination complexes were accessed via metalation of the sodium or potassium salt of the appropriate ligand with vanadyl acetylacetonate, followed by cation metathesis with tetraphenylphosphonium bromide. The ligands were synthesized through an approach which relied largely on the $C_3S_5^{2-}$ ("dmit") ligand as a precursor.^{48,49}

The ligand component of compound **2** was synthesized via nucleophilic attack of the $C_3S_5^{2-}$ moiety on 1,3-dibromopropane,⁵⁰ followed by conversion of the thione into a ketone with $Hg(OAc)_2$ to afford the proligand.⁵¹ The $C_7H_6S_6^{2-}$ ligand for compound **3** involved substituting one of the ketone moieties of thiapendione ($C_4S_4O_2$)⁵² for a dibutyltin protecting group, then subjecting that species to a Me_3Al -mediated coupling with an ester containing the 1,3-dithiane moiety to generate the ketone-protected proligand.⁵³ Finally, we accessed the cyanoethyl-protected proligand of $C_9H_6S_8^{2-}$ via the phosphite-mediated coupling of two C_3S_5 -based subunits.⁵⁰ For **2** and **3**, ligand deprotection was accomplished via nucleophilic attack of either $NaOEt$ (**2**) or $KOMe$ (**3**) on the ketone moiety, while for **1** and **4**, deprotection occurred via deprotonation (using $KOMe$ in the case of **1** and $KOtBu$ for **4**).

Our initial studies focused on determining the vanadium hyperfine coupling parameter, A , and the electron g -tensor, g , to characterize the magnetic properties of the series of complexes. These compounds were designed to maintain a uniform electronic structure at the spin-bearing center, as

significant deviations from that would pose a challenge for deriving meaningful conclusions from the series. Fortunately, previous studies demonstrated that A and g are largely invariant across series of vanadyl complexes,^{43,54–56} since the orbital bearing the unpaired electron remains constant.⁵⁴ To establish the validity of our design approach, we extracted g and A via echo-detected electron paramagnetic resonance (ED-EPR) spectroscopy. ED-EPR results in a spectrum containing the same information as a traditional continuous-wave (cw) EPR spectrum, however it is recorded as an absorption spectrum instead of the more common derivative lineshape.⁵⁷ Fitting of the ED-EPR spectra of solutions of **1–4** in 45 vol% dimethylformamide- d_7 /toluene- d_8 (DMF- d_7 /toluene- d_8) to an axial Hamiltonian (see Figure 4.3) yielded values of $g_{\perp} = 1.982–1.986$, $g_{\parallel} = 1.969–1.978$, $A_{\perp} = 120–129$ MHz, and $A_{\parallel} = 395–418$ MHz, all of which are within the range of values typically exhibited by vanadyl bis(dithiolene) complexes.^{40,43,54–56,58,59} These data demonstrate that the complexes possess similar local electronic structures, eliminating variability in electronic structure from consideration.

The performance of a qubit system is described by two figures of merit: the coherence time (T_2), which is the time window of control for the qubit,⁸ and the spin-lattice relaxation time (T_1), which serves as an upper limit to T_2 and the inverse of which (T_1^{-1}) determines the qubit operating speed.^{23,60}

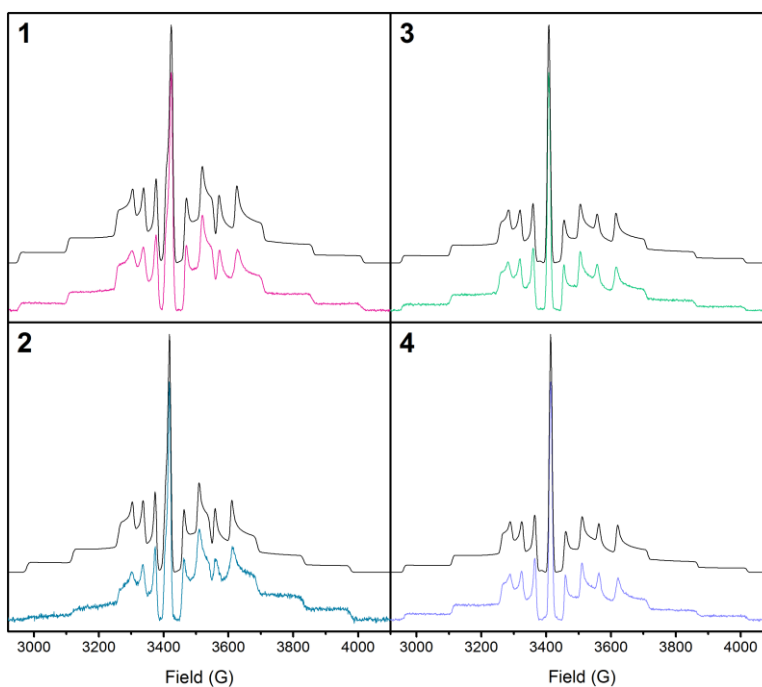


Figure 4.3 Echo-detected EPR spectra for **1–4** in DMF- d_7 /toluene- d_8 . Fits to the spectra are shown in black and offset from the data, shown in color.

Measuring T_1 allows us to determine its impact on T_2 and probe the processes by which spin-lattice relaxation occurs. We therefore performed inversion recovery measurements⁵⁷ on dilute solutions of the complexes in 45 vol% DMF- d_7 /toluene- d_8 to quantify T_1 (Figure 4.4, plotted as T_1^{-1}). Examination of the data reveals a high degree of similarity between complexes with values ranging from 11.3(9)–17.5(14) ms at 10 K to 10.32(12)–12.97(13) μ s at 140 K. Further, the values of T_1 are virtually identical to those previously reported in a study of vanadyl dithiolene complexes,⁴³ as are the values obtained by fitting the data to an equation modeling T_1 that incorporates the effect of a direct and a Raman process. The direct process is a phonon-mediated spin-flip in which the emitted photon is of the exact energy of the spin transition, whereas the two-phonon Raman process works analogously to the Raman scattering of light, where the difference between the energies of the two phonons is equal to the energy of the spin flip.²³ These two processes are commonly assigned as the predominant contributors to T_1 below 100 K.^{23,61} The surprising consistency of T_1 values between two families of complexes with significantly different ligand sets speaks to the importance of the immediate coordination sphere around the vanadium ion in

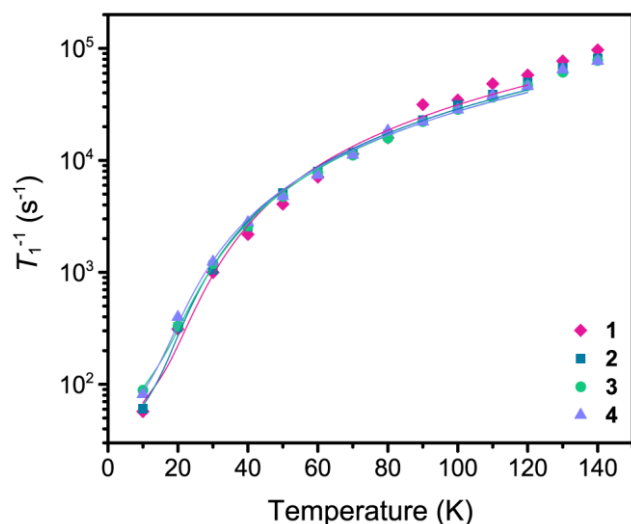


Figure 4.4 Temperature dependence of T_1^{-1} for **1–4** in DMF- d_7 /toluene- d_8 . Fits of the data to an equation accounting for effects from the direct and Raman processes are shown as lines.

influencing T_1 and the relative irrelevance of the composition of more distant elements of the ligand sphere. It also provides further evidence of the uniformity of the series of compounds with regard to every variable except nuclear spin proximity.

Following measurement of T_1 , we sought to determine the parameter directly influenced by interactions between electronic and

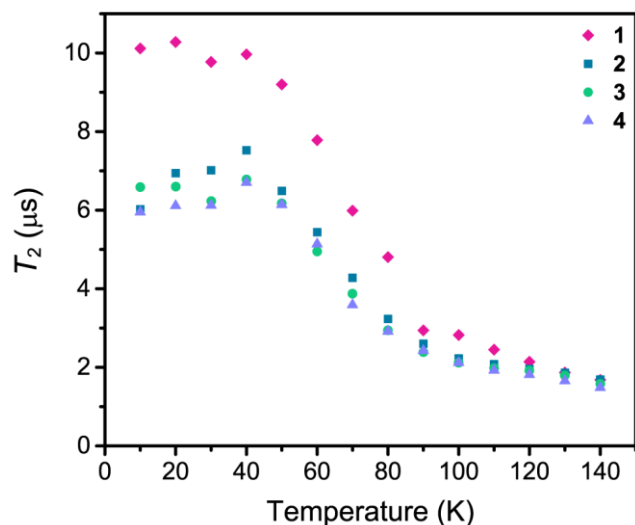


Figure 4.5 Temperature dependence of T_2 for **1–4** in DMF- d_7 /toluene- d_8 .

nuclear spins, T_2 . Measurement of the coherence times (T_2) of the complexes proceeded via application of a standard Hahn echo pulse sequence⁵⁷ at temperatures between 10 and 140 K, and fitting of the resulting decay curve to a stretched exponential function (Figure 4.5).³³ All T_2 measurements were acquired in DMF- d_7 /toluene- d_8 in order to minimize the solvent contribution to decoherence, as deuterons possess a significantly lower magnetic moment ($\mu = 0.86 \mu_N$) than protons.⁴⁷ The most noticeable feature of the dataset is the longer T_2 values exhibited by **1** than those of **2–4**; at 40 K, **1** possesses a T_2 value of 9.97(3) μs , whereas **2–4** exhibit values of 6.70(2)–7.52(2) μs . Upon closer inspection, it is further evident that **2** exhibits slightly longer values of T_2 than **3** and **4** across the range of measured temperatures (e.g. 7.52(2) μs for **2** at 40 K, compared with 6.78(2) μs for **3** and 6.70(2) μs for **4**). The observed differences in T_2 are consistent with a model for decoherence incorporating a nuclear spin diffusion barrier. Specifically, the decrease in T_2 on moving from **1** to **2**, and then to **3** and **4**, is consistent with the protons of **1** being positioned inside the diffusion barrier radius, those of **2** being located close to the barrier radius, and those

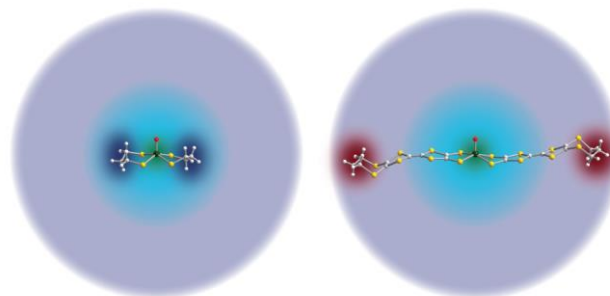


Figure 4.6 Depiction of our model of the measured diffusion barrier. On both sides, the inner blue circle indicates the diffusion barrier while the larger purple circle indicates the region in which nuclei contribute maximally to decoherence. At left, the ligand protons are positioned within the diffusion barrier radius, and thus do not contribute to decoherence. At right, the protons are fully outside the barrier radius, and contribute significantly to decoherence. Note that although the barrier is not necessarily spherical, we have depicted it as such for simplicity.

of **3** and **4** occupying positions significantly outside the barrier radius (Figure 4.6). This implies a barrier radius of between 4.0(4) and 6.6(6) Å from the spin center (Figure 4.7). Further, the fact that there is only a minimal change in T_2 on moving from **3** to **4** (9.3(7) Å and 12.6(7) Å, respectively) potentially suggests that the distance at which nuclei contribute maximally to decoherence is approximately 13 Å. Future work on analogous complexes with greater V–H distances will be necessary to confirm this. Knowledge of the maximal decoherence radius is extremely important for the design of long-coherence complexes, and until now has never been addressed specifically in the literature.

The diffusion barrier, illustrated in Figure 4.6, defines multiple regions by their differing nuclear-electronic coupling strengths. The nuclear spins closest to the electronic spin lie within the diffusion barrier, and are strongly coupled to the electronic spin, preventing the spin flips that erase information. That portion is depicted in a blue circle. Since the protons of compound **1** occupy positions in this region, the strength of the magnetic coupling between those protons and the electronic spin ties them together, preventing them from contributing to decoherence. The next region of interaction is described by sufficiently weak coupling to prevent the spins from locking, but sufficiently strong coupling to enable the electronic spin to experience the effects of nuclear spin-based decoherence. The protons of compounds **3** and **4** occupy this region, and thus the electronic spins in these compounds

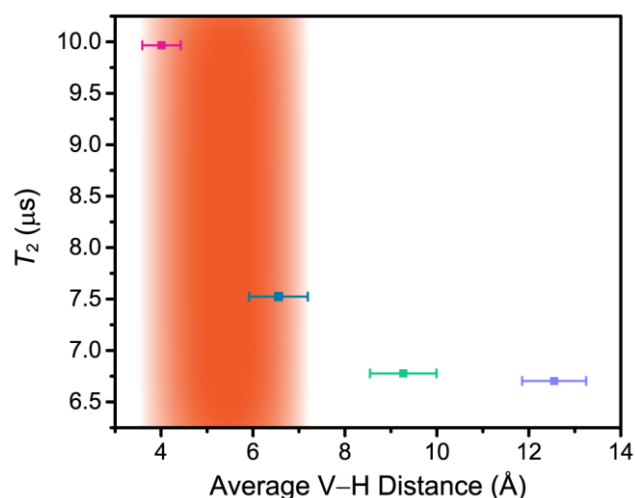


Figure 4.7 Plot of T_2 versus average V–H distance at 40 K for **1–4** in DMF- d_7 /toluene- d_8 . Horizontal error bars represent the standard deviation for the distribution of V–H distances. Vertical error bars are inside the symbols in all cases. The area highlighted in orange represents the window for the potential extent of the diffusion barrier.

experience the maximum impact of decoherence. We postulate that if a complex were designed with a propyl bridge significantly greater than 13 Å from an electronic spin, it would enter the final regime wherein the distal interactions do not engender decoherence

This hypothesis could be tested by expanding the current data set to additional complexes with longer V–H spacings, and by devising studies to probe the common scenario of baths of nuclear spins. In a spin bath, nuclear spin-nuclear spin interactions and the increase in the number of nuclear spins at a given radius from the qubit center with r^2 both strongly affect the distance- T_2 relationship.^{34,35} Performing these studies would shed light onto the generality of these conclusions, and provide insight into the precise end of the diffusion barrier. Thus, the distance dependence of contributions to T_2 remains a fruitful area for future study.

The shape of the temperature-dependence of T_2 for the complexes offers further information about the types of processes contributing to decoherence in different temperature regimes. Between 10 and 40 K, the values of T_2 for all species are approximately constant. Decoherence in this regime is dominated by nuclear spin diffusion, as is frequently observed for coordination complexes in spin-bearing solvents.^{15,23,62,63} Above 40 K, the drop in T_2 is assigned to the onset of methyl group rotation occurring at a frequency comparable to the experimental timescale. As the temperature further increases above 80 K, the contribution of methyl rotations decreases as the rotational time constant becomes faster than the experimental timescale, resulting in a shallowing of the slope of the T_2 vs. temperature curve for all complexes.^{23,33,63} However, T_2 for all complexes continues to decrease with increasing temperature, attaining values of 1.485(14)–1.69(2) μs at 140 K. Even at high temperatures, T_2 remains approximately one order of magnitude lower than T_1 , indicating that it is not T_1 -limited.

4.3 Outlook

Our synthetic studies establish the nuclear spin diffusion barrier at a radius between 4.0(4) and 6.6(6) Å and suggest the maximal decoherence radius may be at approximately 13 Å. These studies offer promise for the synthesis of new candidate qubits with nuclear spin proximate to electronic spin. Indeed, relaxing a rigid nuclear spin-free design principle will inform our future studies on bimetallic qubit systems. Crucially, beyond qubits, the work described herein may impact a wide range of research fields. One area with the potential for dramatic impact is that of dynamic nuclear polarization nuclear magnetic resonance, (DNP-NMR). Extraordinary signal enhancements are possible with DNP-NMR which have the potential to revolutionize NMR spectroscopy of biological systems.⁶⁴ However, the exact method of polarization transfer between electrons and nuclei in DNP-NMR, especially in the context of the spin diffusion barrier, remains a matter of ongoing research,^{34,35} which hinders the rational development of improved polarization agents. We anticipate these results will provide insight into the future design of such systems.

Outside of molecular polarization agents and qubits, within solid-state quantum sensors, there is ample work on detecting nuclear spins via electronic spin coherence.^{65,66} Establishing a distance dependence between electronic spin coherence and nuclear spin proximity may also aid in developing new quantum sensors, an area at the vanguard of quantum technologies.

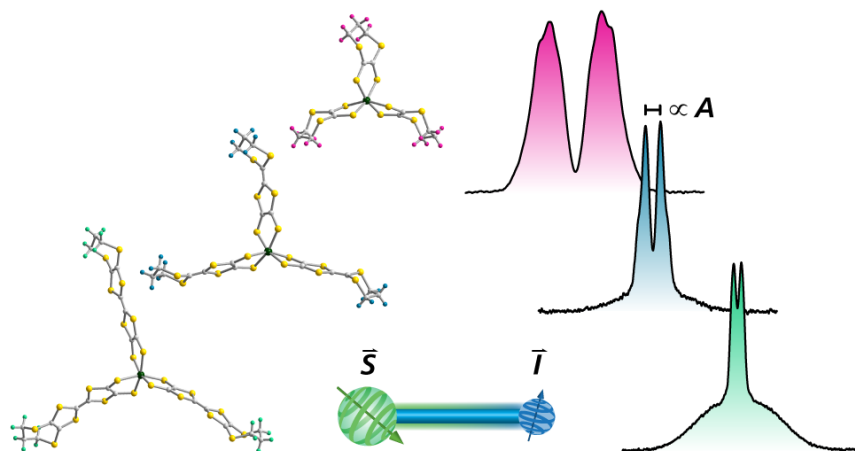
Chapter Five: Probing Nuclear Spin Effects on Electronic Spin Coherence via EPR
Measurements of Vanadium (IV) Complexes

Reprinted with permission from:

Graham, M. J.; Krzyaniak, M.; Wasielewski, M. R.; Freedman, D. E. *Inorganic Chemistry* **2017**,
56, 8106–8113.

Copyright 2017 American Chemical Society.

This work was performed in collaboration with the co-authors listed above.



5.1 Introduction

Quantum information processing (QIP) is an emerging computational paradigm that has the potential to ignite a second digital revolution.^{1,2} QIP is predicated on the ability to place a quantum object into a superposition of two states, enabling it to serve as a quantum bit (qubit), the fundamental unit of information in QIP.¹⁻⁴ One promising physical system for the actualization of qubits is unpaired electronic spins in coordination complexes.⁵⁻⁸ As such spins are inherently quantum objects containing two states, $M_S = \pm 1/2$, they are readily placed into superposition states via the use of pulsed microwaves. Further, the chemical tunability engendered by coordination complexes means that molecular qubits can be chemically coupled to each other to yield functional devices, and possess electronic properties which are readily adaptable to the constraints of a given system.

A crucial challenge for the realization of electron spin-based QIP is the creation of design principles that allow the rational synthesis of qubits with long spin coherence lifetimes, also termed superposition lifetimes or T_2 .⁵⁻⁸ Long T_2 times are a vital prerequisite for qubit viability,⁹ and are difficult to obtain due to ever-present interactions with the environment which promote decoherence, the collapse of the superposition state. The maximization of T_2 (which is also sometimes referred to as the spin-spin relaxation time) is therefore a significant focus of the QIP literature. Recent advances have resulted in the synthesis of both solid-state and molecular qubits exceeding the 100 μs coherence time threshold for qubit viability,¹⁰⁻¹⁸ and new strategies are being developed for the creation of long-coherence complexes.¹⁹ However, significant work remains before full synthetic control of coherence times is achieved.

One fruitful system that has produced a plethora of design principles and information about the root causes of decoherence in molecules is coordination complexes bearing the vanadium(IV)

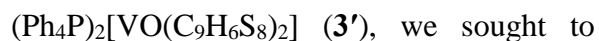
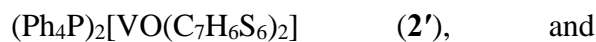
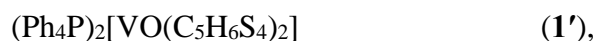
ion. Studies of vanadium(IV) complexes yielded quantum coherences that persist up to room temperature,²⁰ elucidated the effects of specific chemical moieties^{11,21} and environmental factors^{22,23} on decoherence, and established the possibility of employing hyperfine transitions as qubits.²⁴ Most recently, our group reported a study of four vanadyl complexes which were designed to probe the effect of varying the distance between a set of ligand-based nuclear spins and the electronic spin qubit located on the vanadium center.²⁵ Nuclear spins undergoing mutual flip-flops are frequently the largest contributor to decoherence,^{5-8,26} so understanding the precise relationship between the relative position of nuclear spins and their contribution to decoherence is of vital importance. In this prior study, we ascertained that the behavior of the nuclear spins was governed by a nuclear spin diffusion barrier – a distance from the electronic spin center within which nuclei are so strongly coupled to the electron spin that they are effectively locked, and do not undergo decoherence-producing flip-flops.²⁶ Thus, spin-active nuclei positioned inside the barrier do not contribute to decoherence. Outside the barrier, the nuclear spins are no longer locked, but are still coupled to the electron spin, resulting in significant contributions to decoherence. Our study demonstrated that in the series of molecules, the diffusion barrier lies between 4.0(4) and 6.6(6) Å from the vanadium center.

Expanding upon this single study, we sought to determine whether we would observe similar effects in a series of vanadium tris(dithiolene) (hereafter referred to as VS₆) complexes. The abundance of studies on V(IV)-based qubits provides us with a set of established differences and similarities between analogous vanadyl bis(dithiolene) and VS₆ species, thereby recommending the VS₆ species as an initial point of comparison.^{10,11,21} We endeavored to synthesize and examine a series of VS₆ complexes bearing the same four ligands as were previously used to probe the extent of the diffusion barrier radius in vanadyl complexes. As the vanadium ion in a VS₆ complex

houses its paramagnetic electron in a different orbital than a vanadyl complex, and VS_6 complexes exhibit a different ligand geometry around the metal center, comparison between analogous complexes of the two types allows for assessment of the generality of the design principles previously established for the vanadyl species.¹¹ Examination of the distance dependence in a different complex also potentially allows for observation of additional decoherence phenomena occurring in the vanadyl complexes which are masked by the strong interaction of the vanadyl moiety with its local environment.^{11,21} Towards these ends, we report the synthesis and characterization of three novel VS_6 species and the analysis of their coherence properties in the context of the previously-synthesized vanadyl analogues. We find that in addition to electron-nuclear distance, the charge-to-size ratio of a qubit complex plays an important role in decoherence, and discuss the implications of this novel design principle.

5.2 Results and Discussion

To mimic our prior study of the effect of nuclear-electronic distance in the complexes



we sought to synthesize a series of VS_6 molecules bearing the same ligands as previously used.²⁵

Towards that end we synthesized the analogous three VS_6 complexes

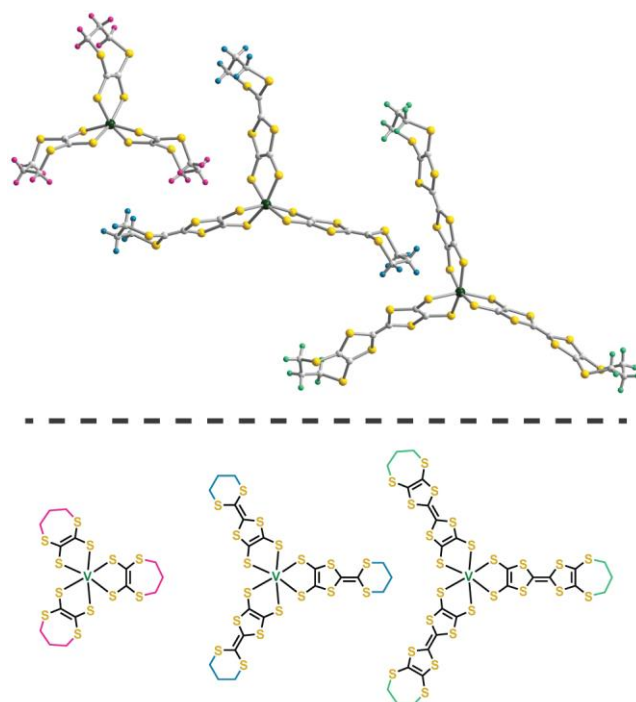


Figure 5.1 Top: Crystal structures of the anionic complexes of **1–3**. Dark green, yellow, and grey spheres represent vanadium, sulfur, and carbon atoms, respectively. Hydrogen atoms are colored pink in **1**, blue in **2**, and light green in **3**. Bottom: Schematic drawings of the anionic complexes of **1–3**.

$\text{K}_2[\text{V}(\text{C}_9\text{H}_6\text{S}_8)_3]$ (**3**) (Figure 5.1). The complexes were accessed via a similar route employed for the vanadyl complexes. For **1** and **2**, the ketone-protected proligands^{27,28} were deprotected via nucleophilic attack of KOMe to afford $\text{K}_2\text{C}_5\text{H}_6\text{S}_4$ and $\text{K}_2\text{C}_7\text{H}_6\text{S}_6$, respectively,²⁹ which were then reacted with $\text{VCl}_4(\text{C}_4\text{H}_8\text{O})_2$ to generate the complexes. In the case of **2**, metalation in tetrahydrofuran resulted in a spontaneous oxidation of the complex to generate the monoanionic species; reduction with potassium naphthalenide produced the targeted dianionic complex. Complex **3** was generated by deprotection of the cyanoethyl-protected proligand³⁰ with KOTBu to afford $\text{K}_2\text{C}_9\text{H}_6\text{S}_8$, which was then reacted with $\text{VCl}_4(\text{C}_4\text{H}_8\text{O})_2$ as for **1** and **2**. This complex was found to be unstable in solution at room temperature, with degradation beginning within ~24 hours; as such, solutions were prepared and then frozen and stored in liquid nitrogen until measurement. In the solid state, however, the compound is stable for at least two weeks at room temperature when stored under an inert atmosphere. Unfortunately, attempts to synthesize $[\text{V}(\text{C}_3\text{H}_6\text{S}_2)_3]^{2-}$, the analogue of the smallest member of the vanadyl series, were unsuccessful. We hypothesize that this is due to the formation of multinuclear complexes, as was previously observed with reaction of the 1,2-ethanedithiolate ligand with vanadium(IV).³¹

Each complex employed a spin-free carbon-sulfur scaffold to place propyl linkers (each containing 6 protons) at a specific distance from an $S = 1/2$ vanadium(IV) ion. Since protons exhibit a large nuclear magnetic moment of $\mu = 2.79 \mu_{\text{N}}$ and a 99.99% natural abundance (compared with e.g. $\mu = 0.40 \mu_{\text{N}}$ for ^{14}N),³² they are an ideal choice for examining the impact of nuclear spins on decoherence. The average V–H distances exhibited by the complexes were 6.6(7) Å for **1**, 9.9(7) Å for **2**, and 12.7(7) Å for **3**, similar to the values of 6.6(6) Å, 9.3(7) Å, and 12.6(7) Å observed in **1'–3'**, respectively. Thus, **1–3** provide a suitable platform for examining the effect of changing geometry and electronic structure on T_2 while keeping the important variable of V–H distance

consistent with the previous series. Further, unlike the previous series, **1–3** possess potassium counterions in place of the nuclear spin-laden Ph_4P^+ . The low magnetic moment of potassium ($\mu = 0.39 \mu_{\text{N}}$ for ^{39}K) eliminates possible counterion effects from consideration and enables the use of electron-nuclear double resonance (ENDOR) experiments to probe the magnitude of hyperfine coupling to the ligand protons.

Following synthesis, we characterized the complexes by continuous-wave electron paramagnetic resonance (cw-EPR) spectroscopy in order to determine the electron g -tensor and the vanadium hyperfine coupling (A) for each species.³³ These two parameters characterize the environment experienced by the unpaired electron, enabling assessment of the consistency of the electronic structure between the three complexes. Differences in electronic structure would create a confounding variable in the series, making it difficult to assess the effect of changing V–H distance on decoherence. As such, establishing electronic consistency across the series is an important first step. Fitting of the cw-EPR spectra of solutions of **1–3** in 45 vol% dimethylformamide-

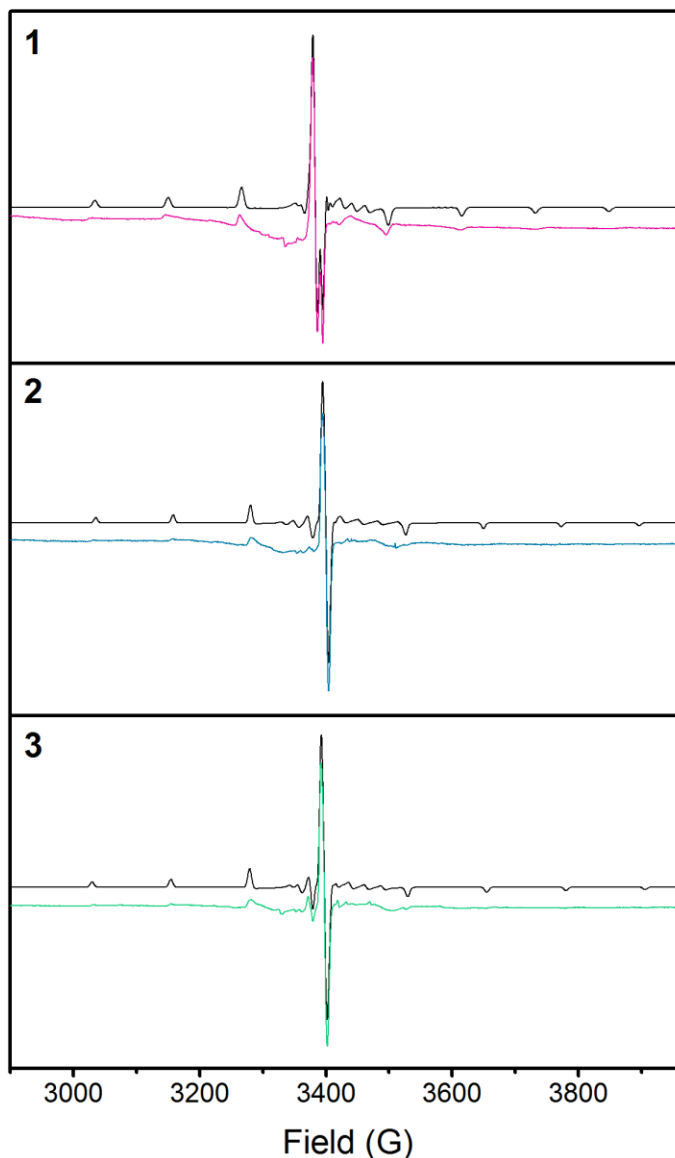


Figure 5.2 Cw-EPR spectra for **1–3** in $\text{DMF-}d_7/\text{toluene-}d_8$. Fits to the spectra are shown in black and offset from the data, shown in color.

d_7 /toluene- d_8 (DMF- d_7 /toluene- d_8) to a rhombic Hamiltonian yielded values of $g_1 = 1.962$ – 1.972 , $g_2 = 1.983$ – 1.988 , $g_3 = 1.992$ – 1.995 , $A_1 = 321$ – 343 MHz, $A_2 = 43$ – 73 MHz, and $A_3 = 5$ – 7 MHz (Figure 5.2). As the range of values across the series is narrow for each parameter, the complexes possess similar electronic structures. The values are also comparable to those typically exhibited by VS_6 species, although most previously reported VS_6 complexes exhibit two large principle hyperfine values (> 200 MHz) and one small value (< 100 MHz), whereas these complexes possess one large principle value and two small values.^{10,21,34–36}

To quantify the hyperfine interaction between the unpaired electron and the ligand protons in each molecule, and thereby confirm that increasing V–H distance does in fact result in a significant decrease in hyperfine coupling, we subjected solutions of **1–3** in 45 vol% DMF- d_7 /toluene- d_8 to Mims ENDOR spectroscopy (Figure 5.3).³³ ENDOR allows for measurement of the hyperfine interactions present in the systems, and therefore enables analysis of the contributions to the overall hyperfine interaction of the through-bond isotropic (Fermi contact) interaction and the through-space dipolar interaction. The obtained spectra are well-simulated by considering the 18 protons in each complex as belonging to three groups of six: one group representing the central protons of the propyl moieties and

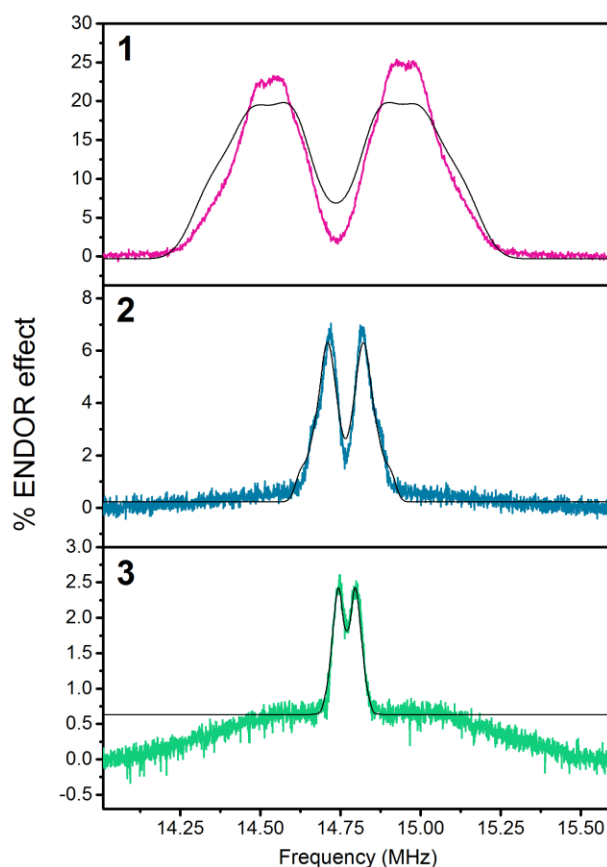


Figure 5.3 Mims ENDOR spectra of **1–3** (colored lines) and simulations of the spectra based on fitted parameters (black lines). Data were acquired at 40 K at a field corresponding to the highest-intensity central feature in the echo-detected EPR spectrum.

the other two representing the edge protons. Within a given group, the isotropic and dipolar couplings are constrained to be equal between different protons (but the two couplings are not constrained to be equal to each other). The dipolar interactions for all groups were calculated based on the V–H distances present in the crystal structures, and were fixed in order to fit the value of the isotropic coupling to the ENDOR data (Table 5.1).

Fitting of the ENDOR data confirms that the magnitude of the hyperfine interaction decreases substantially across the series, and that this decrease is due to changes in both the isotropic

Table 5.1 Best-fit simulation parameters from the ENDOR spectra of **1–3** in DMF-*d*₇/toluene-*d*₈. "Iso" indicates the isotropic (Fermi contact) coupling, "dip" indicates the dipolar coupling, and center/edge indicate the position of the protons within the propyl group. The dipolar couplings were fixed at the values shown below during fitting. All *A* values and the linewidth are expressed in MHz. Note that the absolute signs of the isotropic and dipolar couplings cannot be obtained by fitting Mims ENDOR data – only their relative sign. Thus in the simulations, all dipolar couplings were defined to be positive.

Parameter	1	2	3
$A_{\text{iso}}^{\text{center}}$	0.40	−0.15	−0.070
$A_{\text{iso}}^{\text{edge1}}$	0.43	0.16	0.071
$A_{\text{iso}}^{\text{edge2}}$	−0.16	−0.030	−0.025
$A_{\text{dip}}^{\text{center}}$ (fixed)	0.2035	0.06559	0.03227
$A_{\text{dip}}^{\text{edge1}}$ (fixed)	0.2413	0.07684	0.03603
$A_{\text{dip}}^{\text{edge2}}$ (fixed)	0.4097	0.1070	0.04710
Linewidth (FWHM)	0.077	0.025	0.013
Root-mean-square deviation	7.1%	4.0%	4.6%

coupling and the dipolar coupling. As an example, the magnitude of the fitted isotropic coupling of the central protons decreases from 0.40 MHz in **1**, to 0.15 MHz in **2**, and finally to 0.070 MHz in **3**, while the calculated dipolar coupling for the central protons decreases from 0.20 MHz to 0.066 MHz, and finally to 0.032 MHz.³⁷ The fits of the ENDOR data also reveal the consistency of the geometry of the complexes between the solid state and

solution. Although the dipolar couplings were fixed to values obtained from the crystal structures, the fits obtained from these values nonetheless fit the ENDOR data well. This indicates that the V–H distances do not change substantially upon solvation.

Upon quantification of the hyperfine interaction via ENDOR, and confirmation that the geometries of the solvated complexes match those of the solid-state structures, we proceeded to probe the performance of **1–3** as qubits by measurement of two qubit figures of merit: the spin-lattice relaxation time (T_1) and the coherence time (T_2). The spin-lattice relaxation time is the timescale on which the excited spins relax back to their ground state. As it defines the upper limit of the coherence time, measuring it is important to determine its effect on T_2 and elucidate the processes by which relaxation occurs.^{26,33} We obtained T_1 values by subjecting 0.32 mM solutions of the complexes in 45 vol% DMF- d_7 /toluene- d_8 to inversion recovery measurements at temperatures between 10 and 140 K and fields corresponding to the highest echo intensity in each

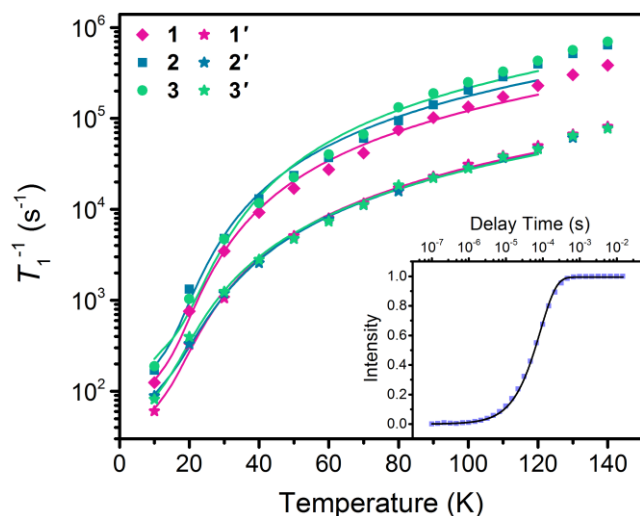


Figure 5.4 Temperature dependence of T_1^{-1} for **1–3** and data previously acquired on **1'–3'** in DMF- d_7 /toluene- d_8 .²⁵ Fits of the data to an equation accounting for effects from the direct and Raman processes through 120 K are shown as lines. Inset: Example of data produced by the inversion recovery experiment, and a fit to the data used to extract out T_1 . The data depicted were collected on **3** in DMF- d_7 /toluene- d_8 at 40 K.

spectrum, and fitting the data to an exponential growth curve to extract out the characteristic time constant.³³ Examination of the data reveals a high degree of similarity between the complexes, although **1** exhibits slightly longer values of T_1 than **2** and **3** across the temperature range measured, indicating a small difference in coupling to lattice vibrational modes between **1** and **2/3** (Figure 5.4, plotted as T_1^{-1}). In contrast, in the previously-synthesized vanadyl complexes,

the T_1 data for **1'** overlay well with those of **2'** and **3'**.²⁵ Between analogous complexes in the VS₆ and vanadyl series, a significant difference in T_1 is evident which ranges from a factor of 1.9–2.3 at 10 K to 4.7–9.1 at 140 K.

Further insight into this difference between **1–3** and **1'–3'** is gained by fitting the data to an equation modeling a direct and a Raman process for relaxation. The direct process is a single-phonon spin-flip process which dominates below 20 K; the Raman process, analogous to the Raman scattering of light, is a higher-temperature, two-phonon process in which the difference in energy between the absorbed and emitted phonons corresponds to the energy of the spin-flip.²⁶ Fitting the data to an equation incorporating these two processes reveals that the difference in T_1 between the VS₆ and vanadyl complexes is due to contributions from both relaxation mechanisms: the direct process is 2–3 times faster in **1–3**, and the Raman process is approximately an order of magnitude faster in **1–3**. The values of T_1 found here, the coefficients of the direct and Raman processes, and the disparity between the two series of complexes are all virtually identical to those previously reported in a comparative study of VS₆ and vanadyl dithiolene complexes by our group.¹¹ In that study, we attributed the difference between the two families to differing interactions with the surrounding solvent matrix – an explanation that is equally valid here. Indeed, the consistency observed between the previous study and this one highlights the importance of the immediate coordination sphere of the vanadium ion in determining T_1 , regardless of the composition of the more distant elements of the ligand.

In order to understand the coherent spin dynamics of the complexes, we then measured their coherence times (T_2) via application of a standard Hahn echo pulse sequence at temperatures between 10 and 140 K, and fit the resulting decay curve to a modulated stretched exponential function.³³ In order to minimize the contribution of extraneous solvent nuclear spins to

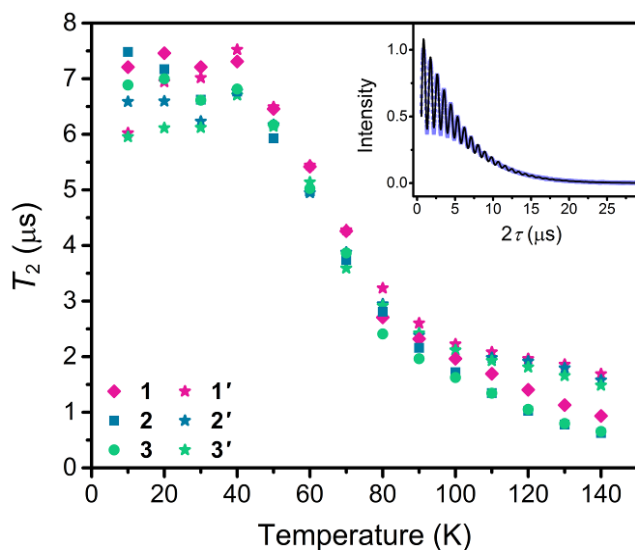


Figure 5.5 Temperature dependence of T_2 for **1–3** and **1'–3'** in DMF- d_7 /toluene- d_8 . Inset: Example of data produced by the Hahn echo experiment, and a fit to the data used to extract out T_2 . The data depicted were collected on **1** in DMF- d_7 /toluene- d_8 at 40 K.

across the entire temperature range measured, with an average difference between the T_2 values of **1** and **3** of $0.38(8) \mu\text{s}$ (Figure 5.5). The difference is consistent with the presence of a nuclear spin diffusion barrier, with the protons of **1** being located close to the barrier radius, and those of **2** and **3** occupying positions significantly outside the barrier radius. This observation mirrors the trend previously observed in **1'–3'** and is consistent with the previously-assigned barrier radius of between $4.0(4)$ and $6.6(6) \text{ \AA}$ from the spin center. The similarity of T_2 between **2** and **3** further supports, though does not definitively confirm, the previous assignment of 13 \AA as the radius of maximal decoherence contribution.²⁵

To garner additional information about the processes driving decoherence, we examined the shape of the temperature-dependence of T_2 . In the 10–40 K regime, the three species exhibit approximately constant values of T_2 between $6.61(2)$ to $7.48(3) \mu\text{s}$. This is consistent with nuclear spin diffusion, a temperature-independent process, dominating T_2 .²⁶ Above 40 K, a sharp drop in T_2 with increasing temperature is observed in both series, which indicates the onset of methyl- d_3

decoherence, the T_2 measurements were performed on 0.32 mM solutions of the complexes in 45 vol% DMF- d_7 /toluene- d_8 , as deuterons possess a significantly lower magnetic moment ($\mu = 0.86 \mu_N$) than the ligand protons.³² As for the T_1 experiments, data were acquired at fields corresponding to the highest echo intensity in each EPR spectrum. The data reveal values of T_2 for **1** that are slightly longer than those of **2** and **3**

group rotation. As both DMF- d_7 and toluene- d_8 contain methyl- d_3 groups, interchange of the positions of methyl deuterons caused by rotation can induce electronic decoherence and shorten T_2 . Previous work examining the effect of methyl groups on decoherence established that the onset of this phenomenon typically occurs between 40 and 80 K,^{11,25,26,38} a temperature range consistent with what is observed here. As the temperature increases above 80 K, the frequency of methyl- d_3 rotation becomes much faster than the experimental timescale, resulting in a partial leveling-off of the T_2 versus T curve.³⁸ Though the T_2 values of **1–3** and **1'–3'** are similar from 40–90 K, signifying similar contributions of methyl deuterons to decoherence in both series, they begin to diverge from each other 100 K. At 140 K, **1–3** reach values of 0.65(2)–0.92(1) μs – 0.75–0.95 μs lower than those of **1'–3'** at the same temperature. This difference is the consequence of the significantly shorter values of T_1 exhibited by **1–3** than those of **1'–3'**. At 140 K, **1–3** possess T_1 values of 1.43(2)–2.60(2) μs , while those of **1'–3'** are an order of magnitude greater: 12.31(14)–12.97(13) μs . The T_2 of **1–3** is therefore T_1 -limited at high temperatures, whereas the T_2 of **1'–3'** is not.

As changing the solvent environment can enable additional insight into the processes affecting decoherence,^{10,38} we acquired T_1 and T_2 data on **1–3** in a different solvent matrix, 45 vol% acetonitrile- d_3 /toluene- d_8 (MeCN- d_3 /toluene- d_8). Though lower signal/noise in the MeCN- d_3 /toluene- d_8 solvent matrix only permitted measurement up to 80 K in the case of **1** and **3** and 110 K in the case of **2**, the lower-temperature data enabled meaningful comparison with the data obtained in DMF- d_7 /toluene- d_8 . To confirm the consistency of the electronic structure of the complexes between the two solvent systems, we attempted to acquire cw-EPR spectra of **1–3**. However, due to the low signal-to-noise ratio of **1** and **3**, we were only able to acquire a cw spectrum for **2**. Therefore, we acquired echo-detected spectra of **1** and **3**. Parameters extracted from the cw-EPR spectrum of **2** were generally consistent with those found in DMF- d_7 /toluene-

d_8 , and simulated spectra for **1** and **3** based on the parameters obtained from the DMF- d_7 /toluene- d_8 samples were consistent with the experimental echo-detected spectra (see Figure 5.6).

Analysis of the T_1 data reveals T_1 values that are slightly lower in MeCN- d_3 /toluene- d_8 than in DMF- d_7 /toluene- d_8 across the measurable temperature regime for **2** and **3**. However, values obtained for **1** are similar between the two solvents (Figure 5.7). The slight decrease in T_1 for **2** and **3** on moving to a less-polar solvent matrix is consistent with previous observations,^{10,11,39,40} though the behavior of **1** is not, and indicates that additional factors are required to explain the observed trend.

On examination of the T_2 data for **1–3** in MeCN- d_3 /toluene- d_8 , we noted a striking dissimilarity to that observed in DMF- d_7 /toluene- d_8 (Figure 5.8). Although the trend of T_2 shortening

with increasing V–H distance is preserved, the T_2 of **1** (3.19(5) μ s) is more than double that of **2** (1.56(6) μ s) and **3** (1.42(5) μ s) at 10 K, and decreases only slightly with increasing temperature while those of **2** and **3** drop more sharply. The result is that at 80 K, the T_2 of **1** (2.8(2) μ s) is 5 times that of **2** (0.57(3) μ s) and 11 times that of **3** (0.26(2) μ s). The large differences between complexes observed here stand in stark contrast to the moderate differences observed in DMF-

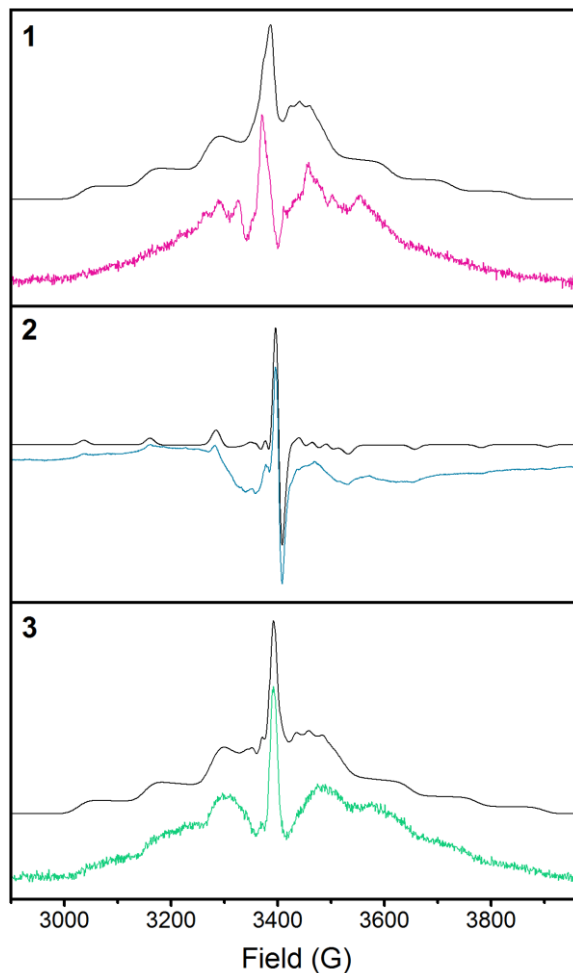


Figure 5.6 Cw-EPR spectra for **2** in MeCN- d_3 /toluene- d_8 (center). Echo-detected EPR spectra for **1** and **3** in MeCN- d_3 /toluene- d_8 (top and bottom). The fit to the cw spectrum and simulations of the echo-detected spectra based on cw parameters from the DMF- d_7 /toluene- d_8 samples (for **1** and **3**) are shown in black and offset from the data, shown in color.

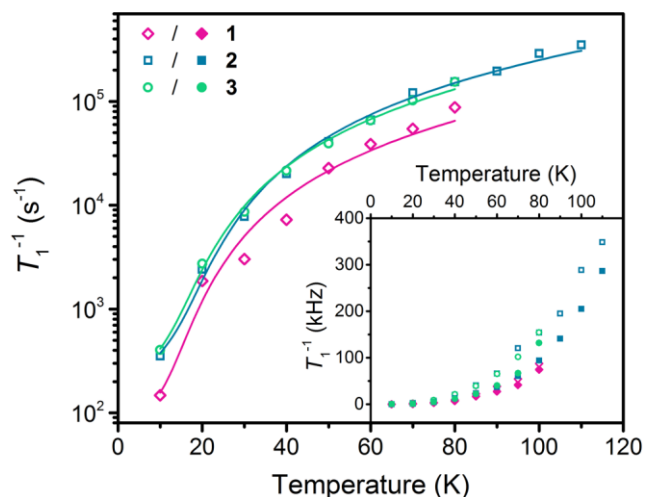


Figure 5.7 Temperature dependence of T_1^{-1} for **1–3** in MeCN- d_3 /toluene- d_8 . Fits of the data to an equation accounting for effects from the direct and Raman processes are shown as lines. Inset: comparison of the temperature dependence of T_1^{-1} in MeCN- d_3 /toluene- d_8 (open symbols) with that in DMF- d_7 /toluene- d_8 (filled symbols), plotted with a linear y-axis for clarity.

d_7 /toluene- d_8 . Further, the T_2 values across the entire temperature range measured are severely attenuated in comparison to the values obtained in DMF- d_7 /toluene- d_8 ; **1** possesses a T_2 1–2.3 times greater in DMF- d_7 /toluene- d_8 , and **2** and **3** exhibit values 3.2–9.3 times greater (Figure 5.8). Differences of this magnitude resulting from solvent substitution bear further investigation to discover their sources.

To aid our analysis, we examined the stretch factor, an additional parameter which can be extracted out of a Hahn echo decay curve. The stretch factor of a decay curve varies depending on the frequency of the dominant decoherence process (W): it approaches 0.5 when the characteristic timescale of the primary decoherence process, $1/W$, is on the order of the interpulse delay τ , is greater than 2 when $1/W$ is much greater than τ , and is approximately equal to 1 when $1/W$ is much less than τ .^{26,38} Comparison of the stretch factors exhibited by the complexes in MeCN- d_3 /toluene- d_8 and DMF- d_7 /toluene- d_8 reveals that they are much larger in the latter solvent system than in the former by an average of 0.4(2), 0.66(10), and 0.6(2)

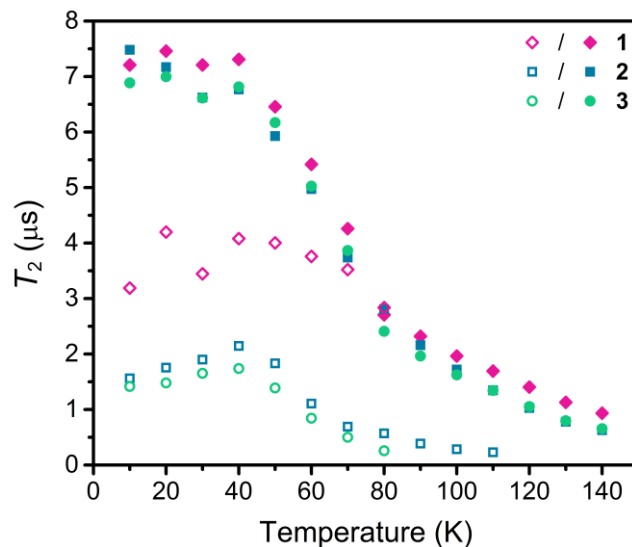


Figure 5.8 Temperature dependence of T_2 for **1–3** in MeCN- d_3 /toluene- d_8 (open symbols) and DMF- d_7 /toluene- d_8 (filled symbols, for comparison).

for **1–3**, respectively. Within the MeCN-*d*₃/toluene-*d*₈ dataset, **1** possesses an average stretch factor across the temperature range of 0.8(2), while **2** and **3** possess significantly lower average stretch factors of 0.59(7)⁴¹ and 0.55(8). Thus, the value of the stretch factor and T_2 are directly correlated in this system. This analysis leads to the conclusion that the characteristic frequency of the dominant decoherence process differs between the two solvent matrices, and between **1** and **2/3** in MeCN-*d*₃/toluene-*d*₈.

A phenomenon which explains the overall drop in T_2 on moving from DMF-*d*₇/toluene-*d*₈ to MeCN-*d*₃/toluene-*d*₈, and which is consistent with the observed stretch factors, is the difference in methyl-*d*₃ rotation rate between DMF-*d*₇ and MeCN-*d*₃. Methyl rotation is observed to play a large role in decoherence, not only at high temperatures where classical rotation dominates, but at lower temperatures as well, where classical rotation cannot occur but tunneling rotation does.^{38,42} An isolated molecule of MeCN-*d*₃ exhibits zero barrier to methyl-*d*₃ rotation by symmetry,⁴³ and therefore undergoes both classical and tunneling rotation at a faster rate than either DMF-*d*₇ or toluene-*d*₈.³⁸ Indeed, the tunneling frequencies of protiated MeCN, toluene, and DMF have been estimated at 22 GHz,⁴⁴ 6.3–6.9 GHz,⁴⁵ and 31 MHz,⁴⁶ respectively. Though deuterated methyl groups undergo tunneling at a lower frequency than protiated methyls,⁴⁷ the tunneling frequencies of methyl-*d*₃ groups can still be appreciable. For example, the tunneling frequency exhibited by toluene-*d*₈ is 270 MHz⁴⁵ – over an order of magnitude slower than that of protiated toluene, but an order of magnitude faster than that of protiated DMF. The decreased barrier to rotation in the methyl-*d*₃ group of MeCN-*d*₃ compared with DMF-*d*₇ can therefore account for the greater decoherence observed for all complexes in MeCN-*d*₃/toluene-*d*₈ across the entire temperature range. However, it does not explain why the difference between the T_2 values of **1** and **2/3** in MeCN-*d*₃/toluene-*d*₈ is so much greater than that seen in DMF-*d*₇/toluene-*d*₈, nor does it address

the disparity in T_1 values.

To explain the difference between the T_1 and T_2 values of **1** and **2/3** in MeCN- d_3 /toluene- d_8 , it is necessary to consider the strength of complex-solvent electrostatic interactions. The series of **1–3** varies not only the V–H interatomic distance, but also the number of atoms over which the 2– charge of each complex is delocalized. As a result, a given atom in **1** should carry a larger partial negative charge than an analogous atom in **3**. This larger negative charge will then engender a stronger electrostatic interaction between specific atoms in the complex and the methyl deuterons of the surrounding solvent molecules, which carry a partial positive charge (Figure 5.9).

The difference in electrostatic interaction strength explains the trends observed in the variable-solvent T_1 data. On moving from DMF- d_7 /toluene- d_8 to the less-polar MeCN- d_3 /toluene- d_8 , T_1 decreases for **2** and **3**, but not for **1**. This can be attributed to the decrease in solvent polarity being masked in the case of **1** by the strong electrostatic interactions of the complex with surrounding solvent molecules. These interactions would create a localized region of higher rigidity that would

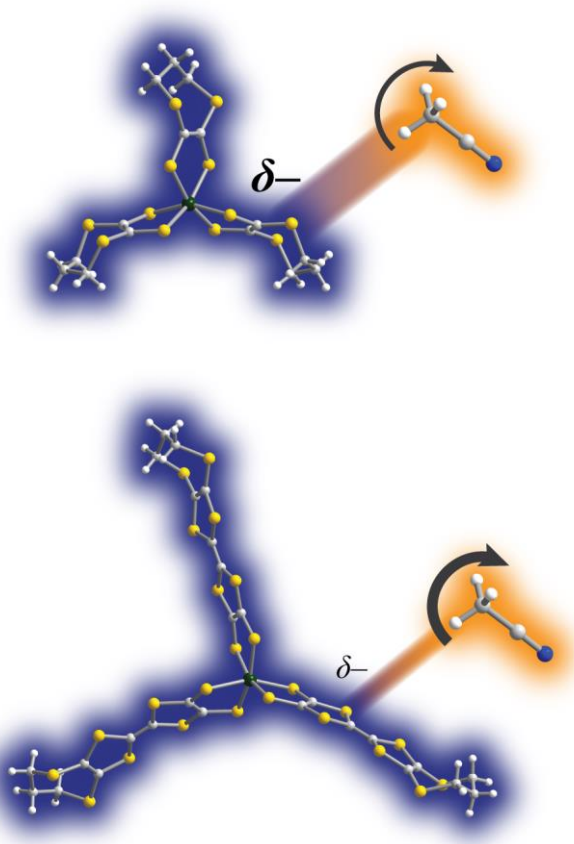


Figure 5.9 Scheme demonstrating the effect of charge density on methyl-promoted decoherence. In the top half, **1**, with its 2– charge spread over fewer atoms, induces a stronger electrostatic interaction with the methyl group of MeCN- d_3 , thereby decreasing the rotational rate of the methyl- d_3 group. In the bottom panel, the greater delocalization of charge in **3** results in a weaker electrostatic interaction with the methyl protons, a greater methyl rotation rate, and greater decoherence.

counteract the overall decrease in lattice rigidity caused by the change to a less-polar matrix. By contrast, the more diffuse charges of **2** and **3** would yield weaker electrostatic interactions with surrounding solvent molecules, less local rigidity, and therefore a larger shift in T_1 on moving to a less-polar solvent.

Differences in electrostatic interaction strength between complexes also explain the disparity in T_2 between **1** and **2/3** in MeCN- d_3 /toluene- d_8 . The vanishing barrier to methyl- d_3 rotation in an isolated molecule of MeCN- d_3 means that its rate of rotation will be extremely dependent on interactions with the local environment.⁴⁴ In the case of **1**, which has a greater charge-to-size ratio, the strong electrostatic interactions of the complex with the methyl deuterons of MeCN- d_3 molecules lead to a greater barrier to methyl- d_3 rotation in those MeCN- d_3 molecules, which results in a slowing of both the tunneling and classical rotation of those methyl- d_3 groups. As the rotation rate of the methyl- d_3 groups decreases, the nuclear spin diffusion caused by the rotation diminishes, which decreases the detrimental effect of the methyl deuterons on T_2 (Figure 5.9). By contrast, **2** and **3**, with their more diffuse charges, do not engender as strong an interaction with the surrounding MeCN- d_3 methyl groups, causing those MeCN- d_3 molecules to exhibit faster methyl- d_3 rotation. The higher rotation frequency increases the rate of nuclear spin diffusion, yielding shorter coherence times for **2/3** than for **1** – exactly what is observed in our data. Thus, the observed solvent dependences of T_1 , T_2 , and the stretch factor can all be explained by a model which includes solvent methyl- d_3 group rotation (both classical and tunneling), and accounts for the varying strength of electrostatic interactions between solvent methyl- d_3 groups and dissolved metal complexes.

5.3 Outlook

Our study provides evidence that in addition to the previously-established effect of nuclear

spin-electron spin distance, variation in charge-to-size ratio can also impact T_2 , primarily through mediation of the electrostatic interaction of the qubit complex with its immediate environment. This result suggests increased molecular charge as a novel design principle for reducing the effect of environmental nuclei on both T_1 and T_2 . Although we anticipate a hypothetical quantum computer constructed from molecular qubits will employ arrays of qubits on a surface, rather than molecules dissolved in solution, this design principle has important implications for the choice of the substrate in such a system.

Additional work remains to confirm the effect of electrostatic interactions and explore it further; the synthesis of a series of complexes which rationally vary charge delocalization would be helpful in this regard. One possible implementation would involve ligands similar to those employed here, but capped by a nuclear spin-free moiety (such as a ketone or thione) instead of a propyl group. Our group is currently exploring this and other potential systems for further examining the effect of charge density on spin relaxation.

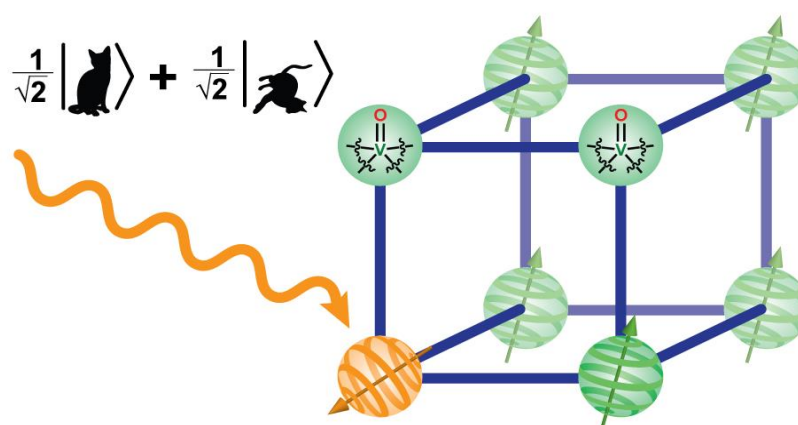
Chapter Six: Conclusion and Outlook

Reprinted with permission from:

Graham, M. J.; Zadrozny, J. M.; Fataftah, M. S.; Freedman, D. E. *Chemistry of Materials* **2017**,
29, 1885–1897.

Copyright 2017 American Chemical Society.

This section was written in collaboration with the co-authors listed above.



The fundamental work completed over the past decade forms a solid foundation of design principles that will enable the eventual synthesis of a surface-based quantum computer. Propelling the field forward in the near future will require employing these principles for the synthesis of viable multi-qubit systems. Moreover, many disparate fields of science can benefit from the study of structure-coherence relationships in molecules and the translation of that understanding into the solid state. This is especially true given that the versatility of transition metal-based materials allows their properties to be tuned not just for use in QIP, but also for other disparate applications like quantum sensing. Here we address both topics, detailing the next steps toward prototype QIP devices and examining other applications for which a detailed understanding of spin coherence is an essential step forward.

6.1 Scaling up requires proof-of-concept molecules and prototype arrays

Bringing molecular design principles into the solid state will require significantly expanding upon current work in molecular multi-qubit systems. The initial challenges in this field are the construction of a wider variety of coupled qubit systems, and designing optimal inter-qubit coupling in these systems. Beautiful research into lanthanides and multinuclear qubits suggests approaches for those systems, yet comparable studies of interacting single-ion transition metal qubits are absent. Ameliorating this deficit is particularly crucial due to the potential tunability inherent to the latter category of complexes. Indeed, employing a mononuclear building unit paradigm for creating multi-qubit systems could lead to a dramatic increase in the coherence time of the constituent qubits. The maximum T_2 value exhibited by a multi-qubit complex is just over $3 \mu\text{s}$,¹ far short of the $100 \mu\text{s}$ viability threshold. We propose a combination of eliminating nuclear spins from ligand scaffolds and intelligently placing any spin-active moieties close to the spin-bearing ion will greatly increase T_2 . As the supporting ligand structures of existing multinuclear

qubit species contain a large number of protons or deuterons, moving away from this architecture may be promising.

Work also remains on developing viable routes to switching interqubit interactions in multi-qubit complexes. Although redox-switching is well-suited to qubits on surfaces,

it is extremely difficult to achieve bulk electron transfer on the necessary nanosecond timescales with proof-of-concept molecules dispersed in a dilute matrix. A potential solution to this challenge employs photoswitchable linkers with a photoaccessible paramagnetic excited state and a diamagnetic ground state. The incorporation of a photoswitchable ligand in a heterobimetallic complex would allow basic computations to be performed on bulk samples, and pave the way for future scaling of electronic spin systems. However, in a future device, microwave switching will still likely dominate as the method of choice due to the proven ability of microwaves to control multiple superconducting qubits^{2,3} and the difficulties associated with coupling single photons to individual qubits.⁴

A promising approach for scaling from proof-of-concept molecules to devices is the chemical synthesis of qubit arrays. Metal-organic frameworks (MOFs) provide the most straightforward route to such qubit assemblies. These species enable, via judicious selection of material building blocks, exact control over specific aspects of the material and hosted qubits. For example, the choice of the linking moiety that bridges the qubit nodes directly affects interqubit orientations and distances, and thus magnetic coupling (Figure 6.1). As MOFs are built from molecular building blocks, they combine the aforementioned synthetic tunability of interqubit interactions

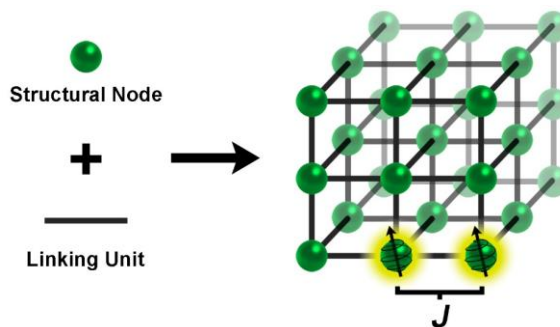


Figure 6.1 Qubits (glowing components) can be installed in metal organic frameworks via selection of proper structural nodes or linking moieties. Magnetic interactions (J) between qubits are open to synthetic fine tuning via proper choice of bridging units.

present in molecules with the benefits of solid-state systems. The molecular nature of MOFs also enables tuning of their phonon spectrum,⁵ which determines the interaction of qubits with the thermal energy of the environment, and therefore T_1 .

The immediate goal in the synthesis of MOF-based qubits is the translation of molecular design principles into MOF systems and the synthesis of long-coherence MOFs. To the best of our knowledge, there are no demonstrations of long ($> 100 \mu\text{s}$) spin-spin relaxation times in metal organic frameworks, and even targeted studies of relaxation times in MOFs are extraordinarily rare in the literature. Examples of applying pulsed EPR to electronic spins in MOFs, however, are not, and cases exist where three-pulse ESEEM, HYSCORE, and ENDOR measurements prove valuable for yielding chemical insight.⁶⁻⁹ While such investigations do not explicitly probe the magnitude of T_2 , successfully performing such pulsed measurements typically requires spin-spin relaxation times of at least 100 ns, and here T_2 likely extends to a few microseconds. Extending T_2 past the viability threshold will require novel MOF architectures which, at a minimum, nearly or completely exclude nuclear spins. Further, additional strategies exist for lengthening T_2 (see section 1.3.4) which may be employed in tandem with the elimination of nuclear spins to extend relaxation times.

6.2 Optical control of qubits is essential for matching the performance of defect systems

Integrating recent breakthroughs in optical manipulation schemes for electronic spin qubits is an attractive strategy for realizing both initialization and readout of qubit operations.^{10,11} As noted above, initialization of qubits by thermalization alone requires long timescales. In contrast, exploiting the orders-of-magnitude faster timescales of optical transitions circumvents this challenge, engendering qubits which are more suitable for device construction. Previous work on optical control exists mostly within the defect-based qubit literature, spanning multiple different

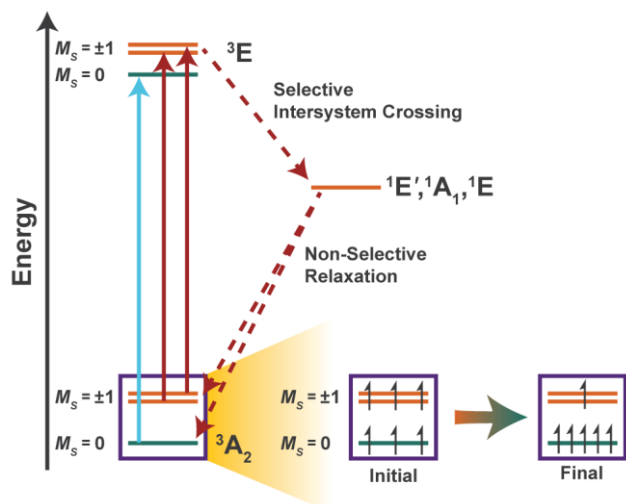


Figure 6.2 Illustration of the photopolarization pathway operative in nitrogen-vacancy centers. Electrons are excited from all spin sublevels in the ground state manifold in a momentum-conserving manner, however intersystem crossing occurs more rapidly from the $M_S = \pm 1$ sublevels than from the $M_S = 0$ sublevel of the 3E state, causing depopulation of those sublevels. Relaxation from the lower-lying states occurs non-selectively to the ground state, completing the polarization pathway, with final selective polarization of the $M_S = 0$ sublevel.

defect types and materials. Awschalom and Hanson, in particular, demonstrated efficient initialization into the $M_S = 0$ spin sublevel of the $S = 1$ ground state of a NV center, attaining values of electronic spin polarization in the range of 0.7–0.9 following a few microseconds of illumination.¹² The

initialization here relies on spin selection rules, wherein intersystem crossing (ISC) occurs more rapidly from the $M_S = \pm 1$ spin sublevels of 3E excited state than from the $M_S = 0$ sublevel, depopulating those sublevels in

the excited state and thereby providing an efficient means for polarizing the $M_S = 0$ sublevel of the ground state (Figure 6.2).¹³

A related approach introduced in a recent report by Awschalom and coworkers demonstrated 99% polarization of the ground spin sublevel in Cr^{4+} defects of SiC and GaN.¹⁴ Here, resonant photoexcitation selectively excites electrons out of the $M_S = 0$ level and thereby drives the population into the $M_S = \pm 1$ sublevels. This approach towards initialization is considerably more difficult to access in molecular complexes, as the resonant optical excitation necessitates extremely narrow linewidths on the scale of the zero-field splitting of the $S = 1$ Cr^{4+} dopant (0.22 cm^{-1} in the system in question).¹⁴ However, incorporation of this polarization method into molecule-based solid-state systems may be possible due to their increased rigidity. $S = 1$ transition metal complexes, such as complexes of Cr^{4+} or Ni^{2+} , which possess both triplet electronic ground and

excited states, could be suitable for either of the aforementioned photopolarization methods, though significant ligand field engineering will be required to synthesize appropriate species.

The second advantage of moving towards optically controlled electronic qubits is the ability for readout through integrated fluorescence measurements of the spin states of interest. As an example, NVCs feature fluorescence from their excited spin triplet state (3E) which exhibits contrast in the integrated fluorescence intensity between the $M_S = \pm 1$ and 0 spin-sublevels. This contrast in fluorescence serves as an effective measure of the population of the $M_S = 0$ spin sublevel, and is the mechanism for optical readout.¹⁰ Optical readout of qubits would enable extremely high readout sensitivity¹⁵ and circumvent some of the challenges associated with performing single-qubit EPR; mimicking the electronic structure of optically measurable solid state defects in modular molecular species is therefore an exciting and challenging prospect. The inherent tunability of the ligand field enables fine-grained control over the optical properties, providing enhanced control over spin-state polarization and fluorescence readout. Successful translation of the solid-state photophysical properties into molecular species will require ingenuity in tuning of photoexcited relaxation processes. As engineering of electronic relaxation rates is similarly vital to photoinitialization, success in addressing this challenge will ultimately dictate the practicality of the photoaddressable qubit paradigm for molecular-inspired device architectures. Designing synthetic approaches towards these challenges would enable tremendous progress towards applications in QIP and sensing.

6.3 Magnetic resonance imaging probes require tuning of the same properties as molecular qubits

Harnessing the quantum properties of molecular magnetic moments via coordination chemistry has significantly broader implications than developing quantum computation. An example of this

lies in the field of magnetic resonance imaging: determination of factors that affect T_1 and T_2 for electronic spins is a crucial component in the design of new MRI (magnetic resonance imaging) probes.¹⁶ Contrast agents in MRI exploit magnetic interactions between open shell complexes and surrounding nuclear spins to generate image contrast. When tethered to chemical probes, such contrast agents can provide spatial resolution of chemical information.^{17,18} A separate and promising mechanism to yield information focuses on probes that enhance nuclear spin polarization to afford increased MRI sensitivity.¹⁹ Dynamic nuclear polarization in solution²⁰ is a promising strategy for this goal but requires long relaxation times (T_1 and T_2) of the electronic spin agent. Thus, the best molecular electronic-spin qubits may also prove valuable as future MRI chemical probes. Note that metal ions are of particular interest here. Biological systems signal physiological dysfunction through atypical variations in temperature, electrochemical potential, acidity, and oxygen concentration. Metal complexes could easily be designed for targeted reactivity to these environmental stimuli. Thus, coupling these reactivity considerations to the quantum properties of designed qubits may instigate a step forward to new families of MRI probes.

6.4 MOF-based qubits can serve as quantum sensors

Quantum sensing is at the vanguard of quantum systems, and may significantly benefit from the molecular qubit design principles unearthed thus far. This nascent field exploits the quantum states of qubits as sensors by manipulating the environment's effects on the qubit, thereby treating decoherence and similar phenomena as a feature rather than a "bug". Qubits in metal-organic frameworks are competent sensors of material properties like structural phase transitions.⁷ Moreover, interactions of the qubits with adsorbed species in a MOF, such as H_2 /HD/D₂, CO₂, and CO, give rise to chemical information about the qubit's surroundings (Figure 6.3).^{8,9} Recent studies focused on biological quantum sensing evidence the power of this approach through the use of

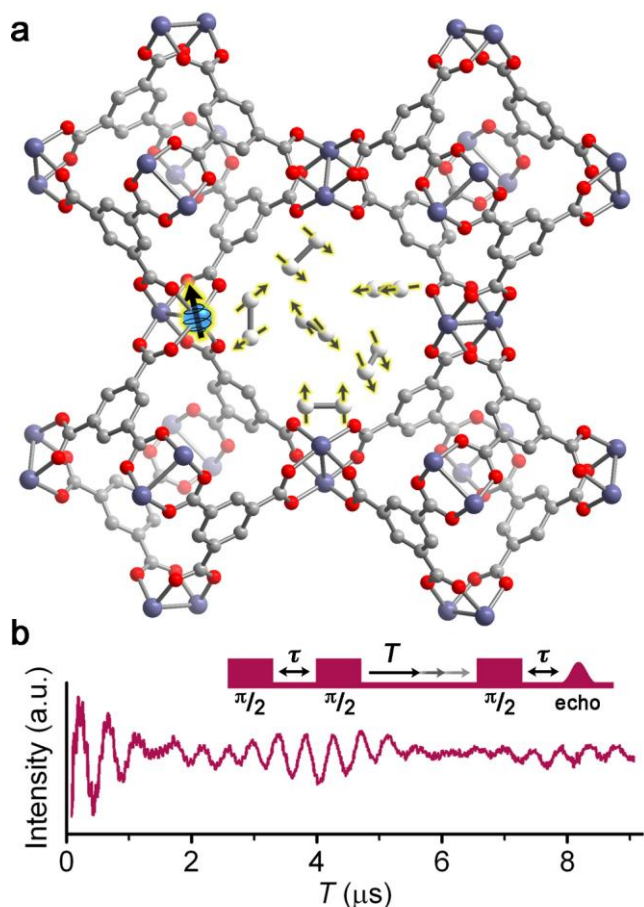


Figure 6.3 (a) The nuclear spins of the molecule ^1H - ^2H (gray, glowing yellow) in the pores of the $\text{Cu}_{2.97}\text{Zn}_{0.03}(\text{Btc})_2$ framework are detected by the Cu^{2+} spin qubits (blue, glowing yellow). (b) This interaction imparts quantum oscillations on the intensity of the three-pulse stimulated echo of the Cu^{2+} ion and provides the primary mechanism of sensing. The frequency of this oscillation corresponds to detected nuclei, in this case ^2H . These data are adapted from ref. 7.

defect sites in solid state materials.²¹ In those studies, defect sites demonstrated their ability to perform thermometry and thermal mapping,^{22,23} sense nuclei and paramagnetic electrons in proximal proteins,^{24,25} and monitor single-neuron action potentials.²⁶ Pushing these instances of quantum sensing to the forefront of materials science requires developing higher sensitivities and the ability to target specific chemical analytes. MOFs are particularly attractive for the latter application, since they offer a highly modifiable pore environment that can be designed for chemical selectivity.²⁷

In order to create MOFs that combine this selectivity with the benefits of quantum sensing, however, sufficiently long relaxation

times for spin qubits need to be realized within MOF architectures. To this end, it is desirable for T_2 to be large even in the presence of nuclear spins, as such spins are an integral part of any potential sensor environment. Such a goal represents a distinct departure from the strategy in quantum computation of avoiding nuclear spins. An approach to extending T_2 in MOFs (and one that is applicable to the synthesis of long-coherence species for QIP) employs atomic-clock EPR transitions (Figure 6.4). Transitions located at hyperfine-induced anticrossings in the Zeeman

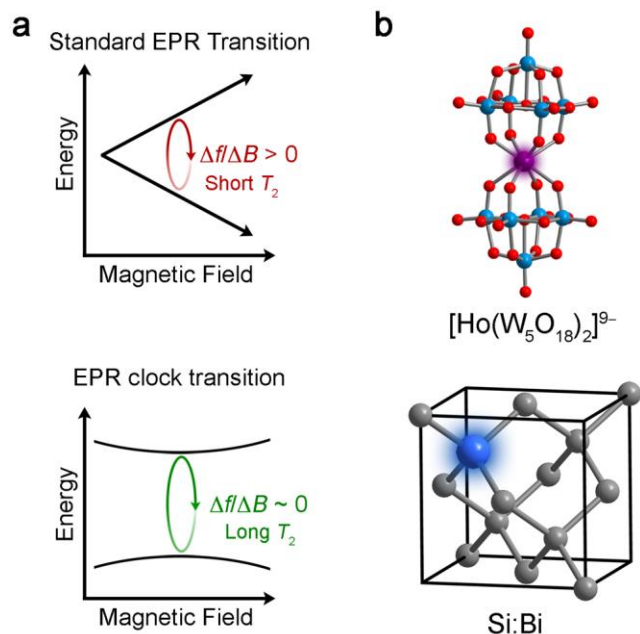


Figure 6.4 Depiction of clock transition and known spin qubits that exhibit them. (a) The two levels of an electronic spin qubit are susceptible to magnetic noise because their transition frequencies (energies), f , change with local magnetic field, $\Delta f/\Delta B \neq 0$. For a qubit that harnesses a clock transition, the two levels are insensitive to magnetic noise because small magnetic field changes do not appreciably alter their energies, $\Delta f/\Delta B \approx 0$. (b) Two existing electronic spin qubits that exploit clock transitions. Glowing blue, glowing purple, teal, gray, and red spheres are Bi, Ho, W, Si, and O atoms, respectively. See references 28 and 29 for more details.

diagram exhibit a vanishing field-dependence of the transition frequency, and are therefore highly resistant to spin-based decoherence. Exciting precedent reveals that extremely long (2.7 s) T_2 parameters are achieved by targeting such transitions in spins of Bi-doped Si.²⁸ A recent breakthrough highlights the promise of extending these design principles to molecules, demonstrating 8.4 μs T_2 values at 5 K for $[\text{Ho}(\text{W}_5\text{O}_{18})_2]^{9-}$.²⁹ Note that this magnitude of T_2 , though below 100 μs , is remarkable considering the high local concentration of Ho^{3+} electronic spins (which possess one of the largest magnetic moments for an isolated metal ion) and Na^+ counterion

nuclear spins ($\mu = 2.22 \mu_N$, 100% natural abundance).³⁰ Integrating the design principles of clock-like transitions with porous materials is a promising strategy for realizing long T_2 values in nuclear spin-rich environments, thereby enabling a new generation of quantum sensing materials.

6.5 Conclusion

The rational design of molecular qubits is an extraordinarily exciting area that has progressed from modest beginnings to a wide-ranging and highly impactful field of endeavor in less than a decade. The research performed to date has yielded a plethora of design principles informing the synthesis and tuning of molecular qubits. Shifting these principles into solid-state architectures is

the field's next great challenge, and will be accomplished through a focus on building multi-qubit systems and enabling the same level of photoaddressability as is present in defect-based systems. In parallel, the hard-won understanding of molecular coherences developed in this field must be disseminated to the wider chemical community. The structure-coherence relationships discovered here directly inform fields as diverse as MRI contrast agents and quantum sensing, and have the potential to influence any area in which the interaction of an electron with its environment is important. Making the impact of this research felt will require engaging synthetic chemists in other fields, enabling them to apply the results to novel problems. If this is accomplished, the coming decade will see the promise of this accumulated knowledge come to fruition.

References

References for Chapter One

- (1) Nielsen, M. A.; Chuang, I. L. *Quantum Computation and Quantum Information*, 10th anniversary ed.; Cambridge University Press: Cambridge, 2010.
- (2) Stolze, J.; Suter, D. *Quantum Computing: A Short Course from Theory to Experiment*, 2nd ed.; Wiley-VCH Verlag GmbH & Co. KGaA: Weinheim, 2008
- (3) Perdomo-Ortiz, A.; Dickson, N.; Drew-Brook, M.; Rose, G.; Aspuru-Guzik, A. Finding low-energy conformations of lattice protein models by quantum annealing. *Sci. Rep.* **2012**, *2*, 571.
- (4) Gershenfeld, N.; Chuang, I. L. Quantum computing with molecules. *Sci. Am.* **1998**, *278*, 66–71.
- (5) DiVincenzo, D. P. The physical implementation of quantum computation. *Fortschr. Phys. – Prog. Phys.* **2000**, *48*, 771–783.
- (6) Doherty, M. W.; Manson, N. B.; Delaney, P.; Jelezko, F.; Wrachtrup, J.; Hollenberg, L. C. L. The nitrogen-vacancy colour centre in diamond. *Phys. Rep.* **2013**, *528*, 1–45.
- (7) Koehl, W. F.; Buckley, B. B.; Heremans, F. J.; Calusine, G.; Awschalom, D. D. Room temperature coherent control of defect spin qubits in silicon carbide. *Nature*, **2011**, *479*, 84–87.
- (8) Widmann, M.; Lee, S.-Y.; Rendler, T.; Son, N. T.; Fedder, H.; Paik, S.; Yang, L.-P.; Zhao, N.; Yang, S.; Booker, I.; Denisenko, A.; Jamali, M.; Momenzadeh, S. A.; Gerhardt, I.; Ohshima, T.; Gali, A.; Janzén, E.; Wrachtrup, J. Coherent control of single spins in silicon carbide at room temperature. *Nat. Mater.* **2014**, *14*, 164–168.
- (9) Christle, D. J.; Falk, A. L.; Andrich, P.; Klimov, P. V.; Hassan, J. U.; Son, N. T.; Janzén, E.; Ohshima, T.; Awschalom, D. D. Isolated electron spins in silicon carbide with millisecond coherence times. *Nat. Mater.* **2014**, *14*, 160–163.
- (10) Jelezko, F.; Wrachtrup, J. Single defect centres in diamond: A review. *Phys. Status Solidi A* **2006**, *203*, 3207–3225.
- (11) Toyli, D. M.; Weis, C. D.; Fuchs, G. D.; Schenkel, T.; Awschalom, D. D. Chip-scale nanofabrication of single spins and spin arrays in diamond. *Nano Lett.* **2010**, *10*, 3168–3172.
- (12) Scarabelli, D.; Trusheim, M.; Gaathon, O.; Englund, D.; Wind, S. J. Nanoscale engineering of closely-spaced electronic spins in diamond. *Nano Lett.* **2016**, *16*, 4982–4990.
- (13) O’Gorman, J.; Nickerson, N. H.; Ross, P.; Morton, J. J. L.; Benjamin, S. C. A silicon-based surface code quantum computer. *NPJ Quantum Inf.* **2016**, *2*, 15019.
- (14) Leuenberger, M.; Loss, D. Quantum computing in molecular magnets. *Nature* **2001**, *410*, 789–793.

- (15) Zadrozny, J. M.; Niklas, J.; Poluektov, O. G.; Freedman, D. E. Millisecond Coherence Time in a Tunable Molecular Electronic Spin Qubit. *ACS Cent. Sci.* **2015**, *1*, 488–492.
- (16) Schweiger, A.; Jeschke, G. *Principles of Pulse Electron Paramagnetic Resonance*; Oxford University Press: New York, 2001.
- (17) Nellutla, S.; Morley, G. W.; van Tol, J.; Pati, M.; Dalal, N. S. Electron spin relaxation and ^{39}K pulsed ENDOR studies on Cr^{5+} -doped K_3NbO_8 at 9.7 and 240 GHz. *Phys. Rev. B* **2008**, *78*, 054426.
- (18) Stanwix, P. L.; Pham, L. M.; Maze, J. R.; Le Sage, D.; Yeung, T. K.; Cappellaro, P.; Hemmer, P. R.; Yacoby, A.; Lukin, M. D.; Walsworth, R. L. Coherence of nitrogen-vacancy electronic spin ensembles in diamond. *Phys. Rev. B* **2010**, *82*, 201201(R).
- (19) Eaton, S. S.; Eaton, G. R. In *Biological Magnetic Resonance*; Berliner, L. J., Eaton, S. S., Eaton, G. R., Eds.; Kluwer Academic/ Plenum Publishers: New York, 2000; Vol. 19, Distance Measurements in Biological Systems by EPR, pp 29–154.
- (20) Ardavan, A.; Rival, O.; Morton, J. J. L.; Blundell, S. J.; Tyryshkin, A. M.; Timco, G. A.; Winpenny, R. E. P. Will Spin-Relaxation Times in Molecular Magnets Permit Quantum Information Processing? *Phys. Rev. Lett.* **2007**, *98*, 057201.
- (21) *CRC Handbook of Chemistry and Physics*, 97th Ed.; Haynes, W. M., Ed.; CRC Press: Boca Raton, FL, 2016; Section 11-2.
- (22) Schlegel, C.; van Slageren, J.; Manoli, M.; Brechin, E. K.; Dressel, M. Direct Observation of Quantum Coherence in Single-Molecule Magnets. *Phys. Rev. Lett.* **2008**, *101*, 147203.
- (23) Morton, J. J. L.; Tyryshkin, A. M.; Ardavan, A.; Porfyrakis, K.; Lyon, S. A.; Briggs, G. A. D. Electron spin relaxation of N@C_{60} in CS_2 . *J. Chem. Phys.* **2006**, *124*, 014508.
- (24) Wedge, C. J.; Timco, G. A.; Spielberg, E. T.; George, R. E.; Tuna, F.; Rigby, S.; McInnes, E. J. L.; Winpenny, R. E. P.; Blundell, S. J.; Ardavan, A. Chemical engineering of molecular qubits. *Phys. Rev. Lett.* **2012**, *108*, 107204.
- (25) Zecevic, A.; Eaton, G. R.; Eaton, S. S.; Lindgren, M. Dephasing of electron spin echoes for nitroxyl radicals in glassy solvents by non-methyl and methyl protons. *Mol. Phys.* **1998**, *95*, 1255–1263.
- (26) Eaton, G. R.; Eaton, S. S. Solvent and Temperature Dependence of Spin Echo Dephasing for Chromium(V) and Vanadyl Complexes in Glassy Solution. *J. Magn. Reson.* **1999**, *136*, 63–68.
- (27) Bader, K.; Dengler, D.; Lenz, S.; Endeward, B.; Jiang, S.-D.; Neugebauer, P.; van Slageren, J. Room temperature quantum coherence in a potential molecular qubit. *Nat. Commun.* **2014**, *5*, 5304.
- (28) Bader, K.; Schlindwein, S. H.; Gudat, D.; van Slageren, J. Molecular qubits based on

potentially nuclear-spin-free nickel ions. *Phys. Chem. Chem. Phys.* **2017**, *19*, 2525–2529.

(29) Takahashi, S.; van Tol, J.; Beedle, C. C.; Hendrickson, D. N.; Brunel, L.-C.; Sherwin, M. S. Coherent Manipulation and Decoherence of $S = 10$ Single-Molecule Magnets. *Phys. Rev. Lett.* **2009**, *102*, 087603.

(30) Morton, J. J. L.; Tyryshkin, A. M.; Ardavan, A.; Porfyrakis, K.; Lyon, S. A.; Briggs, G. A. D. Environmental effects on electron spin relaxation in N@C60. *Phys. Rev. B* **2007**, *76*, 085418.

(31) Yu, C.-J.; Graham, M. J.; Zadrozny, J. M.; Niklas, J.; Krzyaniak, M.; Wasielewski, M. R.; Poluektov O. G.; Freedman, D. E. Long Coherence Times in Nuclear Spin-Free Vanadyl Qubits *J. Am. Chem. Soc.* **2016**, *138*, 14678–14685.

(32) Tesi, L.; Lucaccini, E.; Cimatti, I.; Perfetti, M.; Mannini, M.; Atzori, M.; Morra, E.; Chiesa, M.; Caneschi, A.; Sorace, L.; Sessoli, R. Quantum coherence in a processable vanadyl complex: new tools for the search of molecular spin qubits. *Chem. Sci.* **2016**, *7*, 2074–2083.

(33) Wolfe, J. P. Direct Observation of a Nuclear Spin Diffusion Barrier. *Phys. Rev. Lett.* **1973**, *31*, 907–910.

(34) Pedersen, K. S.; Ariciu, A.-M.; McAdams, S.; Weihe, H.; Bendix, J.; Tuna, F.; Piligkos, S. Toward Molecular 4f Single-Ion Magnet Qubits. *J. Am. Chem. Soc.* **2016**, *138*, 5801–5804.

(35) Graham, M. J.; Yu, C.-J.; Krzyaniak, M. D.; Wasielewski, M. R.; Freedman, D. E. Synthetic Approach To Determine the Effect of Nuclear Spin Distance on Electronic Spin Decoherence. *J. Am. Chem. Soc.* [Online early access]. DOI: 10.1021/jacs.6b13030.

(36) Fielding, A. J.; Fox, S.; Millhauser, G. L.; Chattopadhyay, M.; Kroneck, P. M. H.; Fritz, G.; Eaton, G. R.; Eaton, S. S. Electron spin relaxation of copper(II) complexes in glassy solution between 10 and 120 K. *J. Magn. Reson.* **2006**, *179*, 92–104.

(37) Zhou, Y.; Bowler, B. E.; Eaton, G. R.; Eaton, S. S. Electron Spin Lattice Relaxation Rates for $S = \frac{1}{2}$ Molecular Species in Glassy Matrices or Magnetically Dilute Solids at Temperatures between 10 and 300 K. *J. Magn. Reson.* **1999**, *139*, 165–174.

(38) Atzori, M.; Morra, E.; Tesi, L.; Albino, A.; Chiesa, M.; Sorace, L.; Sessoli, R. Quantum Coherence Times Enhancement in Vanadium(IV)-based Potential Molecular Qubits: The Key Role of the Vanadyl Moiety. *J. Am. Chem. Soc.*, **2016**, *138*, 11234–11244.

(39) Atzori, M.; Tesi, L.; Morra, E.; Chiesa, M.; Sorace, L.; Sessoli, R. Room-Temperature Quantum Coherence and Rabi Oscillations in Vanadyl Phthalocyanine: Toward Multifunctional Molecular Spin Qubits *J. Am. Chem. Soc.* **2016**, *138*, 2154–2157.

(40) Tesi, L.; Lunghi, A.; Atzori, M.; Lucaccini, E.; Sorace, L.; Totti, F.; Sessoli, R. Giant spin-phonon bottleneck effects in evaporable vanadyl-based molecules with long spin coherence. *Dalton Trans.* **2016**, *45*, 16635–16642.

- (41) Zadrozny, J. M.; Graham, M. J.; Krzyaniak, M. D.; Wasielewski, M. R.; Freedman, D. E. Unexpected Suppression of Spin-Lattice Relaxation via High Magnetic Field in a High-Spin Iron(III) Complex. *Chem. Commun.* **2016**, *52*, 10175–10178.
- (42) Zadrozny, J. M.; Freedman, D. E. Qubit Control Limited by Spin–Lattice Relaxation in a Nuclear Spin–Free Iron(III) Complex. *Inorg. Chem.* **2015**, *54*, 12027–12031.
- (43) Bertaina, S.; Gambarelli, S.; Mitra, T.; Tsukerblat, B.; Müller, A.; Barbara, B. Quantum oscillations in a molecular magnet. **2008**, *453*, 203–206.
- (44) Yang, J.; Wang, Y.; Wang, Z.; Rong, X.; Duan, C.-K.; Su, J.-H.; Du, J. Observing Quantum Oscillation of Ground States in Single Molecular Magnet. *Phys. Rev. Lett.* **2012**, *108*, 230501.
- (45) Choi, K.-Y.; Wang, Z.; Nojiri, H.; van Tol, J.; Kumar, P.; Lemmens, P.; Bassil, B. S.; Kortz, U.; Dalal, N. S. Coherent Manipulation of Electron Spins in the {Cu₃} Spin Triangle Complex Impregnated in Nanoporous Silicon. *Phys. Rev. Lett.* **2012**, *108*, 067206.
- (46) Fataftah, M. S.; Zadrozny, J. M.; Coste, S. C.; Graham, M. J.; Rogers, D. M.; Freedman, D. E. Employing Forbidden Transitions as Qubits in a Nuclear Spin-Free Chromium Complex. *J. Am. Chem. Soc.* **2016**, *138*, 1344–1348.
- (47) Zadrozny, J. M.; Niklas, J.; Poluektov, O. G.; Freedman, D. E. Multiple Quantum Coherences from Hyperfine Transitions in a Vanadium(IV) Complex. *J. Am. Chem. Soc.* **2014**, *136*, 15841–15844.
- (48) Burkard, G.; Loss, D.; DiVincenzo, D. P. Coupled quantum dots as quantum gates. *Phys. Rev. B* **1999**, *59*, 2070–2078.
- (49) Ferrando-Soria, J.; Moreno Pineda, E.; Chiesa, A.; Fernandez, A.; Magee, S. A.; Carretta, S.; Santini, P.; Vitorica-Yrezabal, I. J.; Tuna, F.; Timco, G. A.; McInnes, E. J. L.; Winpenny, R. E. P. A modular design of molecular qubits to implement universal quantum gates. *Nat. Commun.* **2016**, *7*, 11377.
- (50) Nakazawa, S.; Nishida, S.; Ise, T.; Yoshino, T.; Mori, N.; Rahimi, R. D.; Sato, K.; Morita, Y.; Toyota, K.; Shiomi, D.; Kitagawa, M.; Hara, H.; Carl, P.; Höfer, P.; and Takui, T. A synthetic two-spin quantum bit: *g*-engineered exchange-coupled biradical designed for controlled-NOT gate operations. *Angew. Chem. Int. Ed.* **2012**, *51*, 9860–9864.
- (51) Luis, F.; Repollés, A.; Martínez-Pérez, M. J.; Aguilà, D.; Roubeau, O.; Zueco, D.; Alonso, P. J.; Evangelisti, M.; Camón, A.; Sesé, J.; Barrios, L. A.; Aromí, G. Molecular Prototypes for Spin-Based CNOT and SWAP Quantum Gates. *Phys. Rev. Lett.* **2011**, *107*, 117203.
- (52) Aguilà, D.; Barrios, L. A.; Velasco, V.; Roubeau, O.; Repollés, A.; Alonso, P. J.; Sesé, J.; Teat, S. J.; Luis, F.; and Aromí, G. Heterodimetallic [LnLn'] Lanthanide complexes: toward a chemical design of two-qubit molecular spin quantum gates. *J. Am. Chem. Soc.* **2014**, *136*, 14215–14222.

(53) Jenkins, M. D.; Zueco, D.; Roubeau, O.; Aromí, G.; Majer, J.; Luis, F. A scalable architecture for quantum computation with molecular nanomagnets. *Dalton Trans.* **2016**, *45*, 16682–16693.

(54) Affronte, M.; Casson, I.; Evangelisti, M.; Candini, A.; Carretta, S.; Muryn, C. A.; Teat, S. J.; Timco, G. A.; Wernsdorfer, W.; Winpenny, R. E. P. Linking rings through diamines and clusters: Exploring synthetic methods for making magnetic quantum gates. *Angew. Chem. Int. Ed.* **2005**, *44*, 6496–6500.

(55) Timco, G. A.; Faust, T. B.; Tuna, F.; Winpenny, R. E. P. Linking heterometallic rings for quantum information processing and amusement. *Chem. Soc. Rev.* **2011**, *40*, 3067–3075.

(56) McInnes, E. J. L.; Timco, G. A.; Whitehead, G. F. S.; Winpenny, R. E. P. Heterometallic rings: their physics and use as supramolecular building blocks. *Angew. Chem. Int. Ed.* **2015**, *54*, 14244–14269.

(57) Fernandez, A.; Ferrando-Soria, J.; Pineda, E. M.; Tuna, F.; Vitorica-Yrezabal, I. J.; Knappke, C.; Ujma, J.; Muryn, C. A.; Timco, G. A.; Barran, P. E.; Ardavan, A.; Winpenny, R. E. P. Making hybrid [n]-rotaxanes as supramolecular arrays of molecular electron spin qubits. *Nat. Commun.* **2016**, *7*, 10240.

(58) Ardavan, A.; Bowen, A. M.; Fernandez, A.; Fielding, A. J.; Kaminski, D.; Moro, F.; Muryn, C. A.; Wise, M. D.; Ruggi, A.; McInnes, E. J. L.; Severin, K.; Timco, G. A.; Timmel, C. R.; Tuna, F.; Whitehead, G. F. S.; Winpenny, R. E. P. Engineering coherent interactions in molecular nanomagnet dimers. *NPJ Quantum Inf.* **2015**, *1*, 15012.

(59) Ferrando-Soria, J.; Magee, S. A.; Chiesa, A.; Carretta, S.; Santini, P.; Vitorica-Yrezabal, I. J.; Tuna, F.; Whitehead, G. F. S.; Sproules, S.; Lancaster, K. M.; Barra, A.-L.; Timco, G. A.; McInnes, E. J. L.; Winpenny, R. E. P. Switchable interaction in molecular double qubits. *Chem* **2016**, *1*, 727–752.

(60) Lehmann, J.; Gaita-Ariño, A.; Coronado, E.; Loss, D. Spin qubits with electrically gated polyoxometalate molecules. *Nature Nanotech.* **2007**, *2*, 312–317.

(61) Santini, P.; Carretta, S.; Troiani, F.; Amoretti, G. Molecular nanomagnets as quantum simulators. *Phys. Rev. Lett.* **2011**, *107*, 230502.

(62) Chiesa, A.; Whitehead, G. F. S.; Carretta, S.; Carthy, L.; Timco, G. A.; Teat, S. J.; Amoretti, G.; Pavarini, E.; Winpenny, R. E. P.; Santini, P. Molecular nanomagnets with switchable coupling for quantum simulation. *Sci. Rep.* **2014**, *4*, 7423.

(63) Gatteschi, D.; Cornia, A.; Mannini, M.; Sessoli, R. Organizing and Addressing Magnetic Molecules. *Inorg. Chem.* **2009**, *48*, 3408–3419.

(64) Corradini, V.; Moro, F.; Biagi, R.; De Renzi, V.; del Pennino, U.; Bellini, V.; Carretta, S.; Santini, P.; Milway, V. A.; Timco, G.; Winpenny, R. E. P.; Affronte, M. Successful grafting of isolated molecular Cr₇Ni rings on Au(111) surface. *Phys. Rev. B* **2009**, *79*, 144419.

(65) Ghirri, A.; Corradini, V.; Bellini, V.; Biagi, R.; del Pennino, U.; De Renzi, V.; Cezar, J. C.; Muryn, C. A.; Timco, G. A.; Winpenny, R. E. P.; Affronte, M. Self-Assembled Monolayer of Cr₇Ni Molecular Nanomagnets by Sublimation. *ACS Nano* **2011**, *5*, 7090–7099.

(66) Ghirri, A.; Corradini, V.; Cervetti, C.; Candini, A.; del Pennino, U.; Timco, G.; Pritchard, R. J.; Muryn, C. A.; Winpenny, R. E. P.; Affronte, M. Deposition of Functionalized Cr₇Ni Molecular Rings on Graphite from the Liquid Phase. *Adv. Funct. Mater.* **2010**, *20*, 1552–1560.

(67) Warner, M.; Din, S.; Tupitsyn I. S.; Morley, G. W.; Stoneham, A. M.; Gardener, J. A.; Wu, Z.; Fisher, A. J.; Heutz, S.; Kay, C. W. M.; Aeppli, G. Potential for spin-based information processing in a thin-film molecular semiconductor. *Nature*, **2013**, *503*, 504–508.

(68) Bode, M. Spin-polarized scanning tunneling microscopy: Breakthroughs and highlights. *Chimia* **2012**, *66*, 56–60.

(69) Loth, S.; Etzkorn, M.; Lutz, C. P.; Eigler, D. M.; Heinrich, A. J. Measurement of fast electron spin relaxation times with atomic resolution. *Science*, **2010**, *329*, 1628–1630.

(70) Baumann, S.; Paul, W.; Choi, T.; Lutz, C. P.; Ardavan, A.; Heinrich, A. J. Electron paramagnetic resonance of individual atoms on a surface. *Science* **2015**, *350*, 417–420.

References for Chapter Two

- (1) (a) Aspuru-Guzik, A.; Dutoi, A. D.; Love, P. J.; Head-Gordon, M. *Science* **2005**, *309*, 1704–1707. (b) Feynman, R. P. *Int. J. Theor. Phys.* **1982**, *21*, 467–488.
- (2) (a) Stolze, J.; Suter, D. *Quantum Computing: A Short Course from Theory to Experiment*; 2nd ed.; Wiley-VCH Verlag GmbH & Co. KGaA: Weinheim, 2008. (b) Vandersypen, L. M. K.; Steffen, M.; Breyta, G.; Yannoni, C. S.; Sherwood, M. H.; Chuang, I. L. *Nature* **2001**, *414*, 883–887.
- (3) Leuenberger, M. N.; Loss, D. *Nature* **2001**, *410*, 789–793.
- (4) Though three of the six transitions depicted in Figure 2.1 are formally forbidden, the frequent observation of forbidden transitions in EPR spectra allows for their consideration as potential qubits.
- (5) Figgis, B. N.; Hitchman, M. A. *Ligand Field Theory and Its Applications*; Wiley-VCH: New York, 2000.
- (6) Kahn, O. *Molecular Magnetism*; VCH Publishers: New York, 1993.
- (7) Stamp, P. C. E.; Gaita-Ariño, A. *J. Mater. Chem.* **2009**, *19*, 1718–1730.
- (8) Wedge, C. J.; Timco, G. A.; Spielberg, E. T.; George, R. E.; Tuna, F.; Rigby, S.; McInnes, E. J. L.; Winpenny, R. E. P.; Blundell, S. J.; Ardavan, A. *Phys. Rev. Lett.* **2012**, *108*, 107204.
- (9) Aromí, G.; Aguilà, D.; Gamez, P.; Luis, F.; Roubeau, O. *Chem. Soc. Rev.* **2012**, *41*, 537–546.
- (10) The phase memory time is also often represented as T_m , e.g. in refs. 20 and 29.
- (11) Ardavan, A.; Rival, O.; Morton, J. J. L.; Blundell, S. J.; Tyryshkin, A. M.; Timco, G. A.; Winpenny, R. E. P. *Phys. Rev. Lett.* **2007**, *98*, 057201.
- (12) Wang, Z.; Datta, S.; Papatrifiantafyllopoulou, C.; Christou, G.; Dalal, N. S.; van Tol, J.; Hill, S. *Polyhedron* **2011**, *30*, 3193–3196.
- (13) Schlegel, C.; van Slageren, J.; Manoli, M.; Brechin, E. K.; Dressel, M. *Phys. Rev. Lett.* **2008**, *101*, 147203.
- (14) Takahashi, S.; Tupitsyn, I. S.; van Tol, J.; Beedle, C. C.; Hendrickson, D. N.; Stamp, P. C. E. *Nature* **2011**, *476*, 76–79.
- (15) (a) Gatteschi, D.; Sessoli, R.; Villain, J. *Molecular Nanomagnets*; Oxford University Press: New York, 2006. (b) Pedersen, K. S.; Bendix, J.; Clérac, R. *Chem. Commun.* **2014**, *50*, 4396–4415. (c) Shatruk, M.; Avendano, C.; Dunbar, K. R. In *Progress in Inorganic Chemistry*; John Wiley & Sons, Inc., 2009; pp. 155–334. (d) Christou, G.; Gatteschi, D.; Hendrickson, D. N.; Sessoli, R. *MRS Bull.* **2000**, *25*, 66–71.

(16) (a) Morello, A.; Stamp, P. C. E.; Tupitsyn, I. S. *Phys. Rev. Lett.* **2006**, *97*, 207206. (b) Stamp, P. C. E.; Tupitsyn, I. S. *Phys. Rev. B* **2004**, *69*, 014401.

(17) (a) Wolf, S. A.; Awschalom, D. D.; Buhrman, R. A.; Daughton, J. M.; von Molnár, S.; Roukes, M. L.; Chtchelkanova, A. Y.; Treger, D. M. *Science* **2001**, *294*, 1488–1495. (b) Zheng, Y.; Wudl, F. *J. Mater. Chem. A* **2014**, *2*, 48–57. (c) Lee, E. C.; Choi, Y. C.; Kim, W. Y.; Singh, N. J.; Lee, S.; Shim, J. H.; Kim, K. S. *Chem.—Eur. J.* **2010**, *16*, 12141–12146. (d) Nuccio, L.; Willis, M.; Schulz, L.; Fratini, S.; Messina, F.; D’Amico, M.; Pratt, F. L.; Lord, J. S.; McKenzie, I.; Loth, M.; Purushothaman, B.; Anthony, J.; Heeney, M.; Wilson, R. M.; Hernández, I.; Cannas, M.; Sedlak, K.; Kreouzis, T.; Gillin, W. P.; Bernhard, C.; Drew, A. J. *Phys. Rev. Lett.* **2013**, *110*, 216602.

(18) Warner, M.; Din, S.; Tupitsyn, I. S.; Morley, G. W.; Stoneham, A. M.; Gardener, J. A.; Wu, Z.; Fisher, A. J.; Heutz, S.; Kay, C. W. M.; Aeppli, G. *Nature* **2013**, *503*, 504–508.

(19) Bertaina, S.; Gambarelli, S.; Mitra, T.; Tsukerblat, B.; Müller, A.; Barbara, B. *Nature* **2008**, *453*, 203–206.

(20) Eaton, S. S.; Eaton, G. R. In *Biological Magnetic Resonance, Volume 19: Distance Measurements in Biological Systems by EPR*; Berliner, L. J.; Eaton, S. S.; Eaton, G. R., Eds.; Kluwer Academic/Plenum Publishers: New York, 2000; pp. 29–154.

(21) (a) Kaziro, R.; Hambley, T. W.; Binstead, R. A.; Beattie, J. K. *Inorg. Chim. Acta* **1989**, *164*, 85–91. (b) Larionova, J.; Mombelli, B.; Sanchiz, J.; Kahn, O. *Inorg. Chem.* **1998**, *37*, 679–684.

(22) Bailar Jr., J. C.; Jones, E. M.; Booth, H. S.; Grennert, M. *Inorg. Synth.* **1939**, *1*, 35–38.

(23) (a) Schmidtke, H.-H.; Eyring, G. *Z. Phys. Chem.* **1974**, *92*, 211–222. (b) Bendix, J.; Brorson, M.; Schäffer, C. E. *Inorg. Chem.* **1993**, *32*, 2838–2849.

(24) (a) Bendix, J.; Steenberg, P.; Søtofte, I. *Inorg. Chem.* **2003**, *42*, 4510–4512. (b) Vostrikova, K. E.; Peresyphkina, E. V. *Eur. J. Inorg. Chem.* **2011**, 811–815.

(25) Albores, P.; Slep, L. D.; Baraldo, L. M.; Baggio, R.; Garland, M. T.; Rentschler, E. *Inorg. Chem.* **2006**, *45*, 2361–2363.

(26) Ochsenbein, S. T.; Gamelin, D. R. *Nat. Nanotechnol.* **2011**, *6*, 112–115.

(27) Although measurement of T_2 in a protiated solvent matrix likely nullifies much of the effect of removing nuclear spins from the system, this consideration was still taken due to the ease of changing solvent systems and the comparative difficulty of ligand substitution.

(28) (a) Eaton, G. R.; Eaton, S. S. *J. Magn. Reson.* **1999**, *136*, 63–68. (b) Fielding, A. J.; Fox, S.; Millhauser, G. L.; Chattopadhyay, M.; Kroneck, P. M. H.; Fritz, G.; Eaton, G. R.; Eaton, S. S. *J. Magn. Reson.* **2006**, *179*, 92–104. (c) Krupskaya, Y.; Zaripov, R.; Vavilova, E.; Miluykov, V.; Bezkishko, I.; Krivolapov, D.; Kataeva, O.; Sinyashin, O.; Hey-Hawkins, E.; Voronkova, V.; Salikhov, K.; Kataev, V.; Büchner, B. *Phys. Rev. B* **2011**, *84*, 092402.

(29) Schweiger, A.; Jeschke, G. *Principles of Pulse Electron Paramagnetic Resonance*; Oxford University Press: New York, 2001.

(30) (a) Yang, J.; Wang, Y.; Wang, Z.; Rong, X.; Duan, C.-K.; Su, J.-H.; Du, J. *Phys. Rev. Lett.* **2012**, *108*, 230501. (b) Moro, F.; Kaminski, D.; Tuna, F.; Whitehead, G. F. S.; Timco, G. A.; Collison, D.; Winpenny, R. E. P.; Ardavan, A.; McInnes, E. J. L. *Chem. Commun.* **2014**, *50*, 91–93. (c) Baldoví, J. J.; Cardona-Serra, S.; Clemente-Juan, J. M.; Coronado, E.; Gaita-Ariño, A.; Prima-García, H. *Chem. Commun.* **2013**, *49*, 8922–8924. (d) Mitrikas, G.; Sanakis, Y.; Raptopoulou, C. P.; Kordas, G.; Papavassiliou, G. *Phys. Chem. Chem. Phys.* **2008**, *10*, 743–748.

References for Chapter Three

- (1) Feynman, R. P. *Int. J. Theor. Phys.* **1982**, *21*, 467–488.
- (2) Lloyd, S. *Science* **1996**, *273*, 1073–1078.
- (3) Aspuru-Guzik, A.; Dutoi, A. D.; Love, P. J.; Head-Gordon, M. *Science* **1996**, *273*, 1073–1078.
- (4) Lambert, N.; Chen, Y.-N.; Cheng, Y.-C.; Li, C.-M.; Chen, G.-Y.; Nori, F. *Nat. Phys.* **2012**, *9*, 10–18.
- (5) Nielsen, M. A.; Chuang, I. L. *Quantum Information and Quantum Computation*, 10th anniversary ed.; Cambridge University Press: Cambridge, 2000.
- (6) Leuenberger, M. N.; Loss, D. *Nature* **2001**, *410*, 789–793.
- (7) Aromí, G.; Aguilà, D.; Gamez, P.; Luis, F.; Roubeau, O. *Chem. Soc. Rev.* **2012**, *41*, 537–546.
- (8) Troiani, F.; Affronte, M. *Chem. Soc. Rev.* **2011**, *40*, 3119–3129.
- (9) Ardavan, A.; Blundell, S. J. *J. Mater. Chem.* **2009**, *19*, 1754–1760.
- (10) Sato, K.; Nakazawa, S.; Rahimi, R.; Ise, T.; Nishida, S.; Yoshino, T.; Mori, N.; Toyota, K.; Shiomi, D.; Yakiyama, Y.; Morita, Y.; Kitagawa, M.; Nakasuji, K.; Nakahara, M.; Hara, H.; Carl, P.; Höfer, P.; Takui, T. *J. Mater. Chem.* **2009**, *19*, 3739–3754.
- (11) Stamp, P. C. E.; Gaita-Ariño, A. *J. Mater. Chem.* **2009**, *19*, 1718–1730.
- (12) Timco, G. A.; Carretta, S.; Troiani, F.; Tuna, F.; Pritchard, R. J.; Muryn, C. A.; McInnes, E. J. L.; Ghirri, A.; Candini, A.; Santini, P.; Amoretti, G.; Affronte, M.; Winpenny, R. E. P. *Nat. Nanotechnol.* **2009**, *4*, 173–178.
- (13) Ferrando-Soria, J.; Moreno Pineda, E.; Chiesa, A.; Fernandez, A.; Magee, S. A.; Carretta, S.; Santini, P.; Vitorica-Yrezabal, I. J.; Tuna, F.; Timco, G. A.; McInnes, E. J. L.; Winpenny, R. E. P. *Nat. Commun.* **2016**, *7*, 11377.
- (14) Hill, S.; Edwards, R. S.; Aliaga-Alcalde, N.; Christou, G. *Science* **2003**, *302*, 1015–1018.
- (15) Troiani, F.; Affronte, M.; Carretta, S.; Santini, P.; Amoretti, G. *Phys. Rev. Lett.* **2005**, *94*, 190501.
- (16) Fataftah, M. S.; Zadrozny, J. M.; Coste, S. C.; Graham, M. J.; Rogers, D. M.; Freedman, D. E. *J. Am. Chem. Soc.* **2016**, *138*, 1344–1348.
- (17) Zadrozny, J. M.; Niklas, J.; Poluektov, O. G.; Freedman, D. E. *J. Am. Chem. Soc.* **2014**, *136*, 15841–15844.

- (18) Ghirri, A.; Chiesa, A.; Carretta, S.; Troiani, F.; van Tol, J.; Hill, S.; Vitorica-Yrezabal, I.; Timco, G. A.; Winpenny, R. E. P.; Affronte, M. *J. Phys. Chem. Lett.* **2015**, *6*, 5062–5066.
- (19) Eaton, S. S.; Eaton, G. R. In *Biological Magnetic Resonance*; Berliner, L. J., Eaton, S. S.; Eaton, G. R., Eds.; Distance Measurements in Biological Systems by EPR; Kluwer Academic/Plenum Publishers: New York, 2000; Vol. 19, pp 29–154.
- (20) Nellutla, S.; Morley, G. W.; van Tol, J.; Pati, M.; Dalal, N. S. *Phys. Rev. B* **2008**, *78*, 054426.
- (21) Graham, M. J.; Zadrozny, J. M.; Shiddiq, M.; Anderson, J. S.; Fataftah, M. S.; Hill, S.; Freedman, D. E. *J. Am. Chem. Soc.* **2014**, *136*, 7623–7626.
- (22) Tesi, L.; Lucaccini, E.; Cimatti, I.; Perfetti, M.; Mannini, M.; Atzori, M.; Morra, E.; Chiesa, M.; Caneschi, A.; Sorace, L.; Sessoli, R. *Chem. Sci.* **2016**, *7*, 2074–2083.
- (23) Shiddiq, M.; Komijani, D.; Duan, Y.; Gaita-Ariño, A.; Coronado, E.; Hill, S. *Nature* **2016**, *531*, 348–351.
- (24) Bader, K.; Winkler, M.; van Slageren, J. *Chem. Commun.* **2016**, *52*, 3623–3626.
- (25) Wedge, C. J.; Timco, G. A.; Spielberg, E. T.; George, R. E.; Tuna, F.; Rigby, S.; McInnes, E. J. L.; Winpenny, R. E. P.; Blundell, S. J.; Ardavan, A. *Phys. Rev. Lett.* **2012**, *108*, 107204.
- (26) Tesi, L.; Lunghi, A.; Atzori, M.; Lucaccini, E.; Sorace, L.; Totti, F.; Sessoli, R. *Dalton Trans.* [Online early access]. DOI: 10.1039/C6DT02559E. Published Online: July 20, 2016.
- (27) Zadrozny, J. M.; Greer, S. M.; Hill, S.; Freedman, D. E. *Chem. Sci.* **2015**, *7*, 416–423.
- (28) Atzori, M.; Morra, E.; Tesi, L.; Albino, A.; Chiesa, M.; Sorace, L.; Sessoli, R. *J. Am. Chem. Soc.* **2016**, *138*, 11234–11244.
- (29) Hamstra, B. J.; Andrew L. P. Houseman; Colpas, G. J.; Kampf, J. W.; LoBrutto, R.; Frasch, W. D.; Pecoraro, V. L. *Inorg. Chem.* **1997**, *36*, 4866–4874.
- (30) Grant, C. V.; Geiser-Bush, K. M.; Cornman, C. R.; Britt, R. D. *Inorg. Chem.* **1999**, *38*, 6285–6288.
- (31) Dikanov, S. A.; Samoilova, R. I.; Smieja, J. A.; Bowman, M. K. *J. Am. Chem. Soc.* **1995**, *117*, 10579–10580.
- (32) Zadrozny, J. M.; Niklas, J.; Poluektov, O. G.; Freedman, D. E. *ACS Cent. Sci.* **2015**, *1*, 488–492.
- (33) Atzori, M.; Tesi, L.; Morra, E.; Chiesa, M.; Sorace, L.; Sessoli, R. *J. Am. Chem. Soc.* **2016**, *138*, 2154–2157.
- (34) Bertaina, S.; Gambarelli, S.; Mitra, T.; Tsukerblat, B.; Müller, A.; Barbara, B. *Nature* **2008**, *453*, 203–206.

- (35) Stanwix, P. L.; Pham, L. M.; Maze, J. R.; Le Sage, D.; Yeung, T. K.; Cappellaro, P.; Hemmer, P. R.; Yacoby, A.; Lukin, M. D.; Walsworth, R. L. *Phys. Rev. B* **2010**, *82*, 201201(R).
- (36) Takahashi, S.; Hanson, R.; van Tol, J.; Sherwin, M. S.; Awschalom, D. D. *Phys. Rev. Lett.* **2008**, *101*, 047601.
- (37) Koehl, W. F.; Buckley, B. B.; Heremans, F. J.; Calusine, G.; Awschalom, D. D. *Nature* **2011**, *479*, 84–87.
- (38) Bertaina, S.; Gambarelli, S.; Tkachuk, A.; Kurkin, I. N.; Malkin, B.; Stepanov, A.; Barbara, B. *Nat. Nanotechnol.* **2007**, *2*, 39–42.
- (39) Zadrozny, J. M.; Graham, M. J.; Krzyaniak, M. D.; Wasielewski, M. R.; Freedman, D. E. *Chem. Commun.* **2016**, *52*, 10175–10178.
- (40) Ardavan, A.; Rival, O.; Morton, J. J. L.; Blundell, S. J.; Tyryshkin, A. M.; Timco, G. A.; Winpenny, R. E. P. *Phys. Rev. Lett.* **2007**, *98*, 057201.
- (41) The assignment of a $d_{x^2-y^2}$ ground state assumes a coordinate system with the x- and y-axes bisecting the angles defined by the S–V–S bonds.
- (42) Kwik, W. L.; Stiefel, E. I. *Inorg. Chem.* **1973**, *12*, 2337–2342.
- (43) Diamantis, A. A.; Raynor, J. B.; Rieger, P. H. *J. Chem. Soc., Dalton Trans.* **1980**, 1731–1733.
- (44) Cooney, J. J. A.; Carducci, M. D.; McElhaney, A. E.; Selby, H. D.; Enemark, J. H. *Inorg. Chem.* **2002**, *41*, 7086–7093.
- (45) Collison, D.; Gahan, B.; Garner, C. D.; Mabbs, F. E. *J. Chem. Soc., Dalton Trans.* **1980**, 667–674.
- (46) Bryant, L. H.; Hodges, M. W.; Bryant, R. G. *Inorg. Chem.* **1999**, *38*, 1002–1005.
- (47) Collison, D.; Mabbs, F. E.; Temperley, J.; Christou, G.; Huffman, J. C. *J. Chem. Soc., Dalton Trans.* **1988**, 309–314.
- (48) Suzuki, T.; Ueda, K.; Kita, R.; Kokado, S.; Harigaya, K. *Polyhedron* **2005**, *24*, 2491–2496.
- (49) Kirmse, R.; Dietzsch, W.; Stach, J.; Olk, R. M.; Hoyer, E. *Z. Anorg. Allg. Chem.* **1987**, *548*, 133–140.
- (50) Wenzel, B.; Strauch, P. *Z. Naturforsch., B: J. Chem. Sci* **1999**, *54*, 165–170.
- (51) Olk, R. M.; Dietzsch, W.; Kirmse, R.; Stach, J.; Hoyer, E. *Inorg. Chim. Acta* **1987**, *128*, 251–259.
- (52) Welch, J. H.; Bereman, R. D.; Singh, P. *Inorg. Chem.* **1988**, *27*, 2862–2868.

- (53) Matsubayashi, G.; Akiba, K.; Tanaka, T. *Inorg. Chem.* **1988**, *27*, 4744–4749.
- (54) Money, J. K.; Huffman, J. C.; Christou, G. *Inorg. Chem.* **1985**, *24*, 3297–3302.
- (55) Henrick, K.; Raston, C. L.; White, A. H. *J. Chem. Soc., Dalton Trans.* **1976**, 26–28.
- (56) Stoll, S.; Schweiger, A. *J. Magn. Reson.* **2006**, *178*, 42–55.
- (57) Moro, F.; Kaminski, D.; Tuna, F.; Whitehead, G. F. S.; Timco, G. A.; Collison, D.; Winpenny, R. E. P.; Ardavan, A.; McInnes, E. J. L. *Chem. Commun.* **2014**, *50*, 91–93.
- (58) Schlegel, C.; van Slageren, J.; Manoli, M.; Brechin, E. K.; Dressel, M. *Phys. Rev. Lett.* **2008**, *101*, 147203.
- (59) Yang, J.; Wang, Y.; Wang, Z.; Rong, X.; Duan, C.-K.; Su, J.-H.; Du, J. *Phys. Rev. Lett.* **2012**, *108*, 230501.
- (60) McGuinness, L. P.; Yan, Y.; Stacey, A.; Simpson, D. A.; Hall, L. T.; Maclaurin, D.; Praver, S.; Mulvaney, P.; Wrachtrup, J.; Caruso, F.; Scholten, R. E.; Hollenberg, L. C. L. *Nat. Nanotechnol.* **2011**, *6*, 358–363.
- (61) Du, J. L.; Eaton, G. R.; Eaton, S. S. *J. Magn. Reson., Ser. A* **1995**, *115*, 213–221.
- (62) Fielding, A. J.; Back, D. B.; Engler, M.; Baruah, B.; Crans, D. C.; Eaton, G. R.; Eaton, S. S. In *Vanadium: The Versatile Metal*; Kustin, K., Pessoa, J. C., Crans, D. C., Eds.; Electron Spin Lattice Relaxation of V(IV) Complexes in Glassy Solutions between 15 and 70 K; American Chemical Society: Washington, DC, 2007; Vol. 974, pp 364–375.
- (63) Zhou, Y.; Bowler, B. E.; Eaton, G. R.; Eaton, S. S. *J. Magn. Reson.* **1999**, *139*, 165–174.
- (64) Sato, H.; Kathirvelu, V.; Fielding, A.; Blinco, J. P.; Micallef, A. S.; Bottle, S. E.; Eaton, S. S.; Eaton, G. R. *Mol. Phys.* **2007**, *105*, 2137–2151.
- (65) Fielding, A. J.; Fox, S.; Millhauser, G. L.; Chattopadhyay, M.; Kroneck, P. M. H.; Fritz, G.; Eaton, G. R.; Eaton, S. S. *J. Magn. Reson.* **2006**, *179*, 92–104.
- (66) Zecevic, A.; Eaton, G. R.; Eaton, S. S.; Lindgren, M. *Mol. Phys.* **1998**, *95*, 1255–1263.

References for Chapter Four

- (1) Sahu, I. D.; McCarrick, R. M.; Lorigan, G. A. *Biochemistry* **2013**, *52*, 5967–5984.
- (2) Spatzal, T.; Aksoyoglu, M.; Zhang, L.; Andrade, S. L. A.; Schleicher, E.; Weber, S.; Rees, D. C.; Emsle, O. *Science* **2011**, *334*, 940.
- (3) Falk, A. L.; Klimov, P. V.; Ivády, V.; Szász, K.; Christle, D. J.; Koehl, W. F.; Gali, Á.; Awschalom, D. D. *Phys. Rev. Lett.* **2015**, *114*, 247603.
- (4) Winpenny, R. E. P. *Angew. Chem. Int. Ed.* **2008**, *47*, 7992–7994.
- (5) Feynman, R. P. *Int. J. Theor. Phys.* **1982**, *21*, 467–488.
- (6) Nielsen, M. A.; Chuang, I. L. *Quantum Information and Quantum Computation*, 10th anniversary ed.; Cambridge University Press: Cambridge, 2000.
- (7) Stolze, J.; Suter, D. *Quantum Computing: A Short Course from Theory to Experiment*, 2nd ed.; Wiley-VCH Verlag GmbH & Co. KGaA: Weinheim, 2008.
- (8) Ladd, T. D.; Jelezko, F.; Laflamme, R.; Nakamura, Y.; Monroe, C.; O’Brien, J. L. *Nature* **2010**, *464*, 45–53.
- (9) Affronte, M.; Troiani, F.; Ghirri, A.; Candini, A.; Evangelisti, M.; Corradini, V.; Carretta, S.; Santini, P.; Amoretti, G.; Tuna, F.; Timco, G.; Winpenny, R. E. P. *J. Phys. D: Appl. Phys.* **2007**, *40*, 2999–3004.
- (10) Ardavan, A.; Blundell, S. J. *J. Mater. Chem.* **2009**, *19*, 1754–1760.
- (11) Stamp, P. C. E.; Gaita-Ariño, A. *J. Mater. Chem.* **2009**, *19*, 1718–1730.
- (12) Troiani, F.; Affronte, M. *Chem. Soc. Rev.* **2011**, *40*, 3119–3129.
- (13) Aromí, G.; Aguilà, D.; Gamez, P.; Luis, F.; Roubeau, O. *Chem. Soc. Rev.* **2012**, *41*, 537–546.
- (14) DiVincenzo, D. P. *Fortschr. Phys.* **2000**, *48*, 771–783.
- (15) Zdrozny, J. M.; Niklas, J.; Poluektov, O. G.; Freedman, D. E. *ACS Cent. Sci.* **2015**, *1*, 488–492.
- (16) Takahashi, S.; Hanson, R.; van Tol, J.; Sherwin, M. S.; Awschalom, D. D. *Phys. Rev. Lett.* **2008**, *101*, 047601.
- (17) Stanwix, P. L.; Pham, L. M.; Maze, J. R.; Le Sage, D.; Yeung, T. K.; Cappellaro, P.; Hemmer, P. R.; Yacoby, A.; Lukin, M. D.; Walsworth, R. L. *Phys. Rev. B* **2010**, *82*, 201201(R).
- (18) Koehl, W. F.; Buckley, B. B.; Heremans, F. J.; Calusine, G.; Awschalom, D. D. *Nature*

2011, 479, 84–87.

(19) Tyryshkin, A. M.; Lyon, S. A.; Astashkin, A. V.; Raitsimring, A. M. *Phys. Rev. B* **2003**, 68, 193207.

(20) Morton, J. J. L.; Tyryshkin, A. M.; Ardavan, A.; Porfyrakis, K.; Lyon, S. A.; Briggs, G. A. *D. J. Chem. Phys.* **2006**, 124, 014508.

(21) Morton, J. J. L.; Tyryshkin, A. M.; Ardavan, A.; Porfyrakis, K.; Lyon, S. A.; Briggs, G. A. *D. Phys. Rev. B* **2007**, 76, 085418.

(22) Brown, R. M.; Ito, Y.; Warner, J. H.; Ardavan, A.; Shinohara, H.; Briggs, G. A. D.; Morton, J. J. L. *Phys. Rev. B* **2010**, 82, 033410.

(23) Eaton, S. S.; Eaton, G. R. In *Biological Magnetic Resonance*; Berliner, L. J., Eaton, S. S., Eaton, G. R., Eds.; Kluwer Academic/ Plenum Publishers: New York, 2000; Vol. 19, Distance Measurements in Biological Systems by EPR, pp 29–154.

(24) Ishikawa, T.; Fu, K.-M. C.; Santori, C.; Acosta, V. M.; Beausoleil, R. G.; Watanabe, H.; Shikata, S.; Itoh, K. M. *Nano Lett.* **2012**, 12, 2083–2087.

(25) Wald, L. L.; Hahn, E. L.; Lukac, M. *J. Opt. Soc. Am. B* **1992**, 9, 789–793.

(26) Bloembergen, N. *Physica (Utrecht)* **1949**, 15, 386–426.

(27) Wolfe, J. P. *Phys. Rev. Lett.* **1973**, 31, 907–910.

(28) Milov, A. D.; Salikhov, K. M.; Tsvetkov, Yu. D. *Sov. Phys. Solid State* **1973**, 15, 802–806.

(29) Hurrell, J. P.; Davies, E. R. *Solid State Commun.* **1971**, 9, 461–463.

(30) Hansen, A. D. A.; Wolfe, J. P. *Phys. Lett.* **1978**, 66A, 320–322.

(31) Guichard, R.; Balian, S. J.; Wolfowicz, G.; Mortemousque, P. A.; Monteiro, T. S. *Phys. Rev. B* **2015**, 91, 214303.

(32) Stuhmann, H. B. *J. Optoelectron. Adv. Mater.* **2015**, 17, 1417–1424.

(33) Zecevic, A.; Eaton, G. R.; Eaton, S. S.; Lindgren, M. *Mol. Phys.* **1998**, 95, 1255–1263.

(34) Ramanathan, C. *Appl. Magn. Reson.* **2008**, 34, 409–421.

(35) Smith, A. A.; Corzilius, B.; Barnes, A. B.; Maly, T.; Griffin, R. G. *J. Chem. Phys.* **2012**, 136, 015101.

(36) Zadrozny, J. M.; Niklas, J.; Poluektov, O. G.; Freedman, D. E. *J. Am. Chem. Soc.* **2014**, 136, 15841–15844.

- (37) Tesi, L.; Lucaccini, E.; Cimatti, I.; Perfetti, M.; Mannini, M.; Atzori, M.; Morra, E.; Chiesa, M.; Caneschi, A.; Sorace, L.; Sessoli, R. *Chem. Sci.* **2016**, *7*, 2074–2083.
- (38) Bader, K.; Winkler, M.; van Slageren, J. *Chem. Commun.* **2016**, *52*, 3623–3626.
- (39) Tesi, L.; Lunghi, A.; Atzori, M.; Lucaccini, E.; Sorace, L.; Totti, F.; Sessoli, R. *Dalton Trans.* **2016**, *45*, 16635–16642.
- (40) Atzori, M.; Morra, E.; Tesi, L.; Albino, A.; Chiesa, M.; Sorace, L.; Sessoli, R. *J. Am. Chem. Soc.*, **2016**, *138*, 11234–11244.
- (41) Atzori, M.; Tesi, L.; Morra, E.; Chiesa, M.; Sorace, L.; Sessoli, R. *J. Am. Chem. Soc.* **2016**, *138*, 2154–2157.
- (42) Bertaina, S.; Gambarelli, S.; Mitra, T.; Tsukerblat, B.; Müller, A.; Barbara, B. *Nature* **2008**, *453*, 203–206.
- (43) Yu, C.-J.; Graham, M. J.; Zadrozny, J. M.; Niklas, J.; Krzyaniak, M.; Wasielewski, M. R.; Poluektov O. G.; Freedman, D. E. *J. Am. Chem. Soc.* **2016**, *138*, 14678–14685.
- (44) Coronado, E.; Galán-Mascarós, J. R.; Gómez García, C. J.; Laukhin, V. *Nature* **2000**, *408*, 447–449.
- (45) Coronado, E.; Day, P. *Chem. Rev.* **2004**, *104*, 5419–5448.
- (46) Kumasaki, M.; Tanaka, H.; Kobayashi, A. *J. Mater. Chem.* **1998**, *8*, 301–307.
- (47) *CRC Handbook of Chemistry and Physics*, 97th Ed.; Haynes, W. M., Ed.; CRC Press: Boca Raton, FL, 2016; Section 11-2.
- (48) Steimecke, G.; Kirmse, R.; Hoyer, E. *Z. Chem.* **1975**, *15*, 28–29.
- (49) Hansen, T. K.; Becher, J.; Jørgensen, T.; Varma, K. S.; Khedekar, R.; Cava, M. P. *Org. Synth.* **1996**, *73*, 270.
- (50) Kumasaki, M.; Tanaka, H.; Kobayashi, A. *J. Mater. Chem.* **1998**, *8*, 301–307.
- (51) Hartke, K.; Kissel, T.; Quante, J.; Matusch, R. *Chem. Ber.* **1980**, *113*, 1898–1906.
- (52) Schumaker, R. R.; Lee, V. Y.; Engler, E. M. *J. Org. Chem.* **1983**, *49*, 564–566.
- (53) Yamada, J.; Satoki, S.; Mishima, S.; Akashi, N.; Takahashi, K.; Masuda, N.; Nishimoto, Y.; Takasaki, S.; Anzai, H. *J. Org. Chem.* **1996**, *61*, 3987–3995.
- (54) Cooney, J. J. A.; Carducci, M. D.; McElhaney, A. E.; Selby, H. D.; Enemark, J. H. *Inorg. Chem.* **2002**, *41*, 7086–7093.
- (55) Wenzel, B.; Strauch, P. *Z. Naturforsch., B: J. Chem. Sci.* **1999**, *54*, 165–170.

- (56) Kirmse, R.; Dietzsch, W.; Stach, J.; Olk, R. M.; Hoyer, E. *Z. Anorg. Allg. Chem.* **1987**, *548*, 133–140.
- (57) Schweiger, A.; Jeschke, G. *Principles of pulse electron paramagnetic resonance*; Oxford University Press: Oxford, 2001.
- (58) Wiggins, R. W.; Huffman, J. C.; Christou, G. *J. Chem. Soc., Chem. Commun.* **1983**, 1313–1315.
- (59) Collison, D.; Mabbs, F. E.; Temperley, J.; Christou, G.; Huffman, J. C. *J. Chem. Soc., Dalton Trans.* **1988**, 309–314.
- (60) Nellutla, S.; Morley, G. W.; van Tol, J.; Pati, M.; Dalal, N. S. *Phys. Rev. B* **2008**, *78*, 054426.
- (61) Zhou, Y.; Bowler, B. E.; Eaton, G. R.; Eaton, S. S. *J. Magn. Reson.* **1999**, *139*, 165–174.
- (62) Wedge, C. J.; Timco, G. A.; Spielberg, E. T.; George, R. E.; Tuna, F.; Rigby, S.; McInnes, E. J. L.; Winpenny, R. E. P.; Blundell, S. J.; Ardavan, A. *Phys. Rev. Lett.* **2012**, *108*, 107204.
- (63) Eaton, G. R.; Eaton, S. S. *J. Magn. Reson.* **1999**, *136*, 63–68.
- (64) Ni, Q. Z.; Daviso, E.; Can, T. V.; Markhasin, E.; Jawla, S. K.; Swager, T. M.; Temkin, R. J.; Herzfeld, J.; Griffin, R. G. *Acc. Chem. Res.* **2013**, *46*, 1933–1941.
- (65) Wu, Y.; Jelezko, F.; Plenio, M. B.; Weil, T. *Angew. Chem. Int. Ed.* **2016**, *55*, 6586–6598.
- (66) Lovchinsky, I.; Sushkov, A. O.; Urbach, E.; de Leon, N. P.; Choi, S.; De Greve, K.; Evans, R.; Gertner, R.; Bersin, E.; Muller, C.; McGuinness, L.; Jelezko, F.; Walsworth, R. L.; Park, H.; Lukin, M. D. *Science* **2016**, *351*, 836–841.

References for Chapter Five

- (1) Nielsen, M. A.; Chuang, I. L. *Quantum Computation and Quantum Information*; 10th anniversary edition; Cambridge University Press: Cambridge, 2010.
- (2) Stolze, J.; Suter, D. *Quantum Computing: A Short Course from Theory to Experiment*, 2nd ed.; Wiley-VCH Verlag GmbH & Co. KGaA: Weinheim, 2008.
- (3) Feynman, R. P. Simulating Physics with Computers. *Int. J. Theor. Phys.* **1982**, *21*, 467–488.
- (4) Ladd, T. D.; Jelezko, F.; Laflamme, R.; Nakamura, Y.; Monroe, C.; O’Brien, J. L. Quantum computers. *Nature* **2010**, *464*, 45–53.
- (5) Graham, M. J.; Zadrozny, J. M.; Fataftah, M. S.; Freedman, D. E. Forging Solid-State Qubit Design Principles in a Molecular Furnace. *Chem. Mater.* **2017**, *29*, 1885–1897.
- (6) Aromí, G.; Aguilà, D.; Gamez, P.; Luis, F.; Roubeau, O. Design of magnetic coordination complexes for quantum computing. *Chem. Soc. Rev.* **2012**, *41*, 537–546.
- (7) Troiani, F.; Affronte, M. Molecular spins for quantum information technologies. *Chem. Soc. Rev.* **2011**, *40*, 3119–3129.
- (8) Stamp, P. C. E.; Gaita-Ariño, A. Spin-based quantum computers made by chemistry: hows and whys. *J. Mater. Chem.* **2009**, *19*, 1718–1730.
- (9) DiVincenzo, D. P. The Physical Implementation of Quantum Computation. *Fortschr. Phys.* **2000**, *48*, 771–783.
- (10) Zadrozny, J. M.; Niklas, J.; Poluektov, O. G.; Freedman, D. E. Millisecond Coherence Time in a Tunable Molecular Electronic Spin Qubit. *ACS Cent. Sci.* **2015**, *1*, 488–492.
- (11) Yu, C.-J.; Graham, M. J.; Zadrozny, J. M.; Niklas, J.; Krzyaniak, M.; Wasielewski, M. R.; Poluektov, O. G.; Freedman, D. E. Long Coherence Times in Nuclear Spin-Free Vanadyl Qubits. *J. Am. Chem. Soc.* **2016**, *138*, 14678–14685.
- (12) Takahashi, S.; Hanson, R.; van Tol, J.; Sherwin, M. S.; Awschalom, D. D. Quenching Spin Decoherence in Diamond through Spin Bath Polarization. *Phys. Rev. Lett.* **2008**, *101*, 047601.
- (13) Stanwix, P. L.; Pham, L. M.; Maze, J. R.; Le Sage, D.; Yeung, T. K.; Cappellaro, P.; Hemmer, P. R.; Yacoby, A.; Lukin, M. D.; Walsworth, R. L. Coherence of nitrogen-vacancy electronic spin ensembles in diamond. *Phys. Rev. B: Condens. Matter Mater. Phys.* **2010**, *82*, 201201.
- (14) Koehl, W. F.; Buckley, B. B.; Heremans, F. J.; Calusine, G.; Awschalom, D. D. Room temperature coherent control of defect spin qubits in silicon carbide. *Nature* **2011**, *479*, 84–87.
- (15) Tyryshkin, A. M.; Lyon, S. A.; Astashkin, A. V.; Raitsimring, A. M. Electron spin

relaxation times of phosphorus donors in silicon. *Phys. Rev. B: Condens. Matter Mater. Phys.* **2003**, *68*, 193207.

(16) Morton, J. J. L.; Tyryshkin, A. M.; Ardavan, A.; Porfyrakis, K.; Lyon, S. A.; Briggs, G. A. D. Electron spin relaxation of N@C₆₀ in CS₂. *J. Chem. Phys.* **2006**, *124*, 014508.

(17) Morton, J. J. L.; Tyryshkin, A. M.; Ardavan, A.; Porfyrakis, K.; Lyon, S. A.; Briggs, G. A. D. Environmental effects on electron spin relaxation in N@C₆₀. *Phys. Rev. B: Condens. Matter Mater. Phys.* **2007**, *76*, 085418.

(18) Brown, R. M.; Ito, Y.; Warner, J. H.; Ardavan, A.; Shinohara, H.; Briggs, G. A. D.; Morton, J. J. L. Electron spin coherence in metallofullerenes: Y, Sc, and La@C₈₂. *Phys. Rev. B: Condens. Matter Mater. Phys.* **2010**, *82*, 033410.

(19) Shiddiq, M.; Komijani, D.; Duan, Y.; Gaita-Ariño, A.; Coronado, E.; Hill, S. Enhancing coherence in molecular spin qubits via atomic clock transitions. *Nature* **2016**, *531*, 348–351.

(20) Atzori, M.; Tesi, L.; Morra, E.; Chiesa, M.; Sorace, L.; Sessoli, R. Room-Temperature Quantum Coherence and Rabi Oscillations in Vanadyl Phthalocyanine: Toward Multifunctional Molecular Spin Qubits. *J. Am. Chem. Soc.* **2016**, *138*, 2154–2157.

(21) Atzori, M.; Morra, E.; Tesi, L.; Albino, A.; Chiesa, M.; Sorace, L.; Sessoli, R. Quantum Coherence Times Enhancement in Vanadium(IV)-based Potential Molecular Qubits: the Key Role of the Vanadyl Moiety. *J. Am. Chem. Soc.*, **2016**, *138*, 11234–11244.

(22) Tesi, L.; Lucaccini, E.; Cimatti, I.; Perfetti, M.; Mannini, M.; Atzori, M.; Morra, E.; Chiesa, M.; Caneschi, A.; Sorace, L.; Sessoli, R. Quantum coherence in a processable vanadyl complex: new tools for the search of molecular spin qubits. *Chem. Sci.* **2016**, *7*, 2074–2083.

(23) Tesi, L.; Lunghi, A.; Atzori, M.; Lucaccini, E.; Sorace, L.; Totti, F.; Sessoli, R. Giant spin-phonon bottleneck effects in evaporable vanadyl-based molecules with long spin coherence. *Dalton Trans.* **2016**, *45*, 16635–16642.

(24) Zadrozny, J. M.; Niklas, J.; Poluektov, O. G.; Freedman, D. E. Multiple Quantum Coherences from Hyperfine Transitions in a Vanadium(IV) Complex. *J. Am. Chem. Soc.* **2014**, *136*, 15841–15844.

(25) Graham, M. J.; Yu, C.-J.; Krzyaniak, M. D.; Wasielewski, M. R.; Freedman, D. E. Synthetic Approach To Determine the Effect of Nuclear Spin Distance on Electronic Spin Decoherence. *J. Am. Chem. Soc.* **2017**, *139*, 3196–3201.

(26) Eaton, S. S.; Eaton, G. R. Distance Measurements in Biological Systems by EPR. In *Biological Magnetic Resonance*; Berliner, L. J., Eaton, S. S., Eaton, G. R., Eds.; Kluwer Academic/Plenum Publishers: New York, 2000; Vol. 19, pp 29–154.

(27) Hartke, K.; Kissel, T.; Quante, J.; Matusch, R. Thion- und Dithioester, XXIV. Synthese von Tetrathiooxalestern. *Chem. Ber.* **1980**, *113*, 1898–1906.

(28) Yamada, J.; Satoki, S.; Mishima, S.; Akashi, N.; Takahashi, K.; Masuda, N.; Nishimoto, Y.; Takasaki, S.; Anzai, H. Synthesis of Unsymmetrical Tetrathiafulvalene Derivatives via Me_3Al -Promoted Reactions of Organotin Compounds with Esters. *J. Org. Chem.* **1996**, *61*, 3987–3995.

(29) Bereman, R. D.; Lu, H. Synthesis and characterization of the nickel and copper complexes of the new dithiolene, 1,3-propanediylthioethylene-1,2-dithiolate (PDDT). *Inorg. Chim. Acta* **1993**, *204*, 53–61.

(30) Kumasaki, M.; Tanaka, H.; Kobayashi, A. Preparation and characterization of metal complexes with an extended TTF dithiolato ligand, bis(propylenedithiotetrathiafulvalenedithiolato)-nickelate and -cuprate *J. Mater. Chem.* **1998**, *8*, 301–307.

(31) (a) Dorfman, J. R.; Holm, R. H. Tetrakis(ethane-1,2-dithiolato)divanadate(III): a binuclear complex with a quadruple bridge, a metal-metal bond, and nonoctahedral stereochemistry. *Inorg. Chem.* **1983**, *22*, 3179–3181. (b) Szymies, D.; Krebs, B.; Henkel, G. $[\text{Ph}_4\text{P}]_2[\text{V}_2(\text{SC}_2\text{H}_4\text{S})_4]\cdot 4\text{MeOH}$: The First Polynuclear Vanadium-Sulfur Complex with Pure Sulfur Coordination. *Angew. Chem. Int. Ed.* **1983**, *22*, 885–886. (c) Wiggans, R. W.; Huffman, J. C.; Christou, G. Vanadium thiolate chemistry: preparation and structures of $[\text{NMe}_4]\text{Na}[\text{VO}(\text{SCH}_2\text{CH}_2\text{S})_2]\cdot 2\text{EtOH}$ and $[\text{Ph}_4\text{P}]_2[\text{V}_2(\text{SCH}_2\text{CH}_2\text{S})_4]$ *J. Chem. Soc., Chem. Commun.* **1983**, 1313–1315.

(32) *CRC Handbook of Chemistry and Physics*, 97th ed.; Haynes, W. M., Ed.; CRC Press: Boca Raton, FL, 2016; Section 11-2.

(33) Schweiger, A.; Jeschke, G. *Principles of pulse electron paramagnetic resonance*; Oxford University Press: New York, 2001.

(34) Olk, R. M.; Dietzsch, W.; Kirmse, R.; Stach, J.; Hoyer, E. In(III), Tl(III) and V(IV) trischelates of the heterocyclic dithiolene and diselenolene ligands 1,3-dithiole-2-thione-4,5-dithiolate (dmit), 1,2-dithiole-3-thione-4,5-dithiolate (dmt) and 1,3-diselenole-2-selone-4,5-diselenolate (dsis). Crystal and molecular structure of $(\text{Bu}_4\text{N})_2[\text{V}(\text{dmt})_3]$ *Inorg. Chim. Acta* **1987**, *128*, 251–259.

(35) Kondo, M.; Minakoshi, S.; Iwata, K.; Shimizu, T.; Matsuzaka, H.; Kamigata, N.; Kitagawa, S. Crystal Structure of a Tris(dithiolene) Vanadium(IV) Complex Having Unprecedented D_{3h} Symmetry. *Chem. Lett.* **1996**, *25*, 489–490.

(36) Sproules, S.; Weyhermüller, T.; DeBeer, S.; Wieghardt, K. Six-Membered Electron Transfer Series $[\text{V}(\text{dithiolene})_3]^{z-}$ ($z = 1+, 0, 1-, 2-, 3-, 4-$). An X-ray Absorption Spectroscopic and Density Functional Theoretical Study. *Inorg. Chem.* **2010**, *49*, 5241–5261.

(37) All coupling values given here are absolute values. Mims ENDOR only allows for determination of the relative sign of the isotropic and dipolar couplings – it does not allow for the determination of their absolute signs.

- (38) Zecevic, A.; Eaton, G. R.; Eaton, S. S.; Lindgren, M. Dephasing of electron spin echoes for nitroxyl radicals in glassy solvents by non-methyl and methyl protons. *Mol. Phys.* **1998**, *95*, 1255–1263.
- (39) Du, J. L.; Eaton, G. R.; Eaton, S. S. Temperature, Orientation, and Solvent Dependence of Electron Spin-Lattice Relaxation Rates for Nitroxyl Radicals in Glassy Solvents and Doped Solids. *J. Magn. Reson., Ser. A* **1995**, *115*, 213–221.
- (40) Sato, H.; Kathirvelu, V.; Fielding, A.; Blinco, J. P.; Micallef, A. S.; Bottle, S. E.; Eaton, S. S.; Eaton, G. R. Impact of molecular size on electron spin relaxation rates of nitroxyl radicals in glassy solvents between 100 and 300 K. *Mol. Phys.* **2007**, *105*, 2137–2151.
- (41) The average stretch factor for **2** was only calculated for the 10–80 K data for consistency with the other two complexes, as the stretch factor decreases with increasing temperature.
- (42) Eaton, G. R.; Eaton, S. S. Solvent and Temperature Dependence of Spin Echo Dephasing for Chromium(V) and Vanadyl Complexes in Glassy Solution. *J. Magn. Reson.* **1999**, *136*, 63–68.
- (43) Zens, A. P.; Ellis, P. D. Measurement of methyl barriers to rotation from carbon-13 spin-rotation relaxation times. *J. Am. Chem. Soc.* **1975**, *97*, 5685–5688.
- (44) Gamlen, P. H.; Stead, W. J.; Tomkinson, J.; White, J. W. Dynamics of Acetonitrile Crystals and Clusters. *J. Chem. Soc., Faraday Trans.* **1991**, *87*, 539–545.
- (45) Cavagnat, D.; Mager, A.; Vettier, C.; Clough, S. Methyl tunnelling in α -crystallised toluene by inelastic neutron scattering: temperature and pressure effects. *J. Phys. C: Solid State Phys.* **1986**, *19*, 6665–6672.
- (46) Hoffmann, S. K.; Goslar, J.; Lijewski, S.; Zalewska, A. EPR and ESE of CuS₄ complex in Cu(dmit)₂: *g*-Factor and hyperfine splitting correlation in tetrahedral Cu–sulfur complexes. *J. Magn. Reson.* **2013**, *236*, 7–14.
- (47) Hoch, M. J. R.; Bovey, F. A.; Davis, D. D.; Douglass, D. C.; Falcone, D. R.; McCall, D. W.; Slichter, W. P. Nuclear Magnetic Resonance in Poly(vinyl acetate). *Macromolecules*, **1971**, *4*, 712–715.

References for Chapter Six

- (1) Ardavan, A.; Bowen, A. M.; Fernandez, A.; Fielding, A. J.; Kaminski, D.; Moro, F.; Muryn, C. A.; Wise, M. D.; Ruggi, A.; McInnes, E. J. L.; Severin, K.; Timco, G. A.; Timmel, C. R.; Tuna, F.; Whitehead, G. F. S.; Winpenny, R. E. P. Engineering coherent interactions in molecular nanomagnet dimers. *NPJ Quantum Inf.* **2015**, *1*, 15012.
- (2) Chow, J. M.; Gambetta, J. M.; Magesan, E.; Abraham, D. W.; Cross, A. W.; Johnson, B. R.; Masluk, N. A.; Ryan, C. A.; Smolin, J. A.; Srinivasan, S. J.; Steffen, M. Implementing a strand of a scalable fault-tolerant quantum computing fabric. *Nat. Commun.* **2014**, *5*, 4015
- (3) Gambetta, J. M.; Chow, J. M.; Steffen, M. Building logical qubits in a superconducting quantum computing system. *NPJ. Quantum Inf.* **2017**, *3*, 2.
- (4) Lodahl, P.; Mahmoodian, S.; Stobbe, S. Interfacing single photons and single quantum dots with photonic nanostructures. *Rev. Mod. Phys.* **2015**, *87*, 347–400.
- (5) Bristow, J. K.; Skelton, J. M.; Svane, K. L.; Walsh, A.; Gale, J. D. A general forcefield for accurate phonon properties of metal-organic frameworks. *Phys. Chem. Chem. Phys.* **2016**, *18*, 29316–29329.
- (6) Hua, C.; Baldansuren, A.; Tuna, F.; Collison, D.; D'Alessandro, D. M. In situ spectroelectrochemical investigations of the redox-active Tris[4-(pyridin-4-yl)phenyl]amine ligand and a Zn²⁺ coordination framework. *Inorg. Chem.* **2016**, *55*, 7270–7280.
- (7) (a) Šimėnas, M.; Ciupa, A.; Maćzka, M.; Pöpl, A.; Banys, J. EPR Study of Structural Phase Transition in Manganese-Doped [(CH₃)₂NH₂][Zn(HCOO)₃] Metal-Organic Framework. *J. Phys. Chem. C* **2015**, *119*, 24522–24528. (b) Šimėnas, M.; Ciupa, A.; Maćzka, M.; Völkel, G.; Pöpl, A.; Banys, J. EPR of Structural Phase Transition in Manganese- and Copper-Doped Formate Framework of [NH₃(CH₂)₄NH₃][Zn(HCOO)₃]₂. *J. Phys. Chem. C* **2016**, *120*, 19751–19758.
- (8) Jee, B.; Hartmann, M.; Pöpl, A. H, D, and HD adsorption upon the metal-organic framework [CuZn(btc)] studied by pulsed ENDOR and HYSCORE spectroscopy. *Mol. Phys.* **2013**, *111*, 2950–2966. (b) Šimėnas, M.; Jee, B.; Hartmann, M.; Banys, J.; Pöpl, A. Adsorption and Desorption of HD on the Metal-Organic Framework Cu_{2.97}Zn_{0.03}(Btc)₂ Studied by Three-Pulse ESEEM Spectroscopy. *J. Phys. Chem. C* **2015**, *119*, 28530–28535.
- (9) Jee, B.; St. Petkov, P.; Vayssilov, G. N.; Heine, T.; Hartmann, M.; Pöpl, A. A Combined Pulsed Electron Paramagnetic Resonance Spectroscopic and DFT Analysis of the ¹³CO₂ and ¹³CO adsorption on the Metal-Organic Framework Cu_{2.97}Zn_{0.03}(btc)₂. *J. Phys. Chem. C* **2013**, *117*, 8231–8240.
- (10) Dobrovitski, V. V.; Fuchs, G. D.; Falk, A. L.; Santori, C.; Awschalom, D. D. Quantum control over single spins in diamond. *Annu. Rev. Cond. Mat. Phys.* **2013**, *4*, 23–50.
- (11) Falk, A. L.; Klimov, P. V.; Ivády, V.; Szász, K.; Christle, D. J.; Koehl, W. F.; Gali, Á.; Awschalom, D. D. Optical polarization of nuclear spins in silicon carbide. *Phys. Rev. Lett.* **2015**,

114, 247603.

(12) Hanson, R.; Mendoza, F. M.; Epstein, R. J.; Awschalom, D. D. Polarization and readout of coupled single spins in diamond. *Phys. Rev. Lett.* **2006**, *97*, 087601.

(13) Robledo, L.; Bernien, H.; van der Sar, T.; Hanson, R. Spin dynamics in the optical cycle of single nitrogen-vacancy centres in diamond *New J. Phys.* **2011**, *13*, 025013.

(14) Koehl, W. F.; Diler, B.; Whiteley, S. J.; Bourassa, A.; Son, N. T.; Janzén, E.; Awschalom, D. D. Resonant optical spectroscopy and coherent control of Cr⁴⁺ spin ensembles in SiC and GaN. *Phys. Rev. B* **2017**, *95*, 035207.

(15) Dreher, L.; Hoehne, F.; Morishita, H.; Huebl, H.; Stutzmann, M.; Itoh, K. M.; Brandt, M. S. Pulsed low-field electrically detected magnetic resonance. *Phys. Rev. B* **2015**, *91*, 075314.

(16) Lauffer, R. B. Paramagnetic metal complexes as water proton relaxation agents for NMR imaging: theory and design. *Chem. Rev.* **1987**, *87*, 901–927.

(17) Heffern, M. C.; Matosziuk, L. M.; Meade, T. J. Lanthanide Probes for Bioresponsive Imaging. *Chem. Rev.* **2014**, *114*, 4496–4539.

(18) Que, E. L.; Chang, C. J. Responsive magnetic resonance imaging contrast agents as chemical sensors for metals in biology and medicine. *Chem. Soc. Rev.* **2010**, *39*, 51–60.

(19) Lurie, D. J. Proton-Electron Double-Resonance Imaging (PEDRI). in *In Vivo EPR (ESR) Theory and Applications*, Berliner, L. J., Ed. *Biol. Magn. Reson.* **2003**, *18*, 547–578.

(20) (a) Bennati, M.; Tkach, I.; Tüerke, M.-T. Dynamic nuclear polarization in liquids. *Electron Paramag. Reson.* **2011**, *22*, 155–182. (b) van Bentum, J.; van Meerten, B.; Sharma, M.; Kentgens, A. Perspectives on DNP-enhanced NMR spectroscopy in solutions. *J. Magn. Reson.* **2016**, *264*, 59–67.

(21) Wu, Y.; Jelezko, F.; Plenio, M. B.; Weil, T. Diamond Quantum Devices in Biology. *Angew. Chem. Int. Ed.* **2016**, *55*, 6586–6598.

(22) Toyli, D. M.; de las Casas, C. F.; Christle, D. J.; Dobrovitski, V. V.; Awschalom, D. D. Fluorescence thermometry enhanced by the quantum coherence of single spins in diamond. *Proc. Natl. Acad. Sci. U. S. A.* **2013**, *110*, 8417–8421.

(23) Kucsko, G.; Maurer, P. C.; Yao, N. Y.; Kubo, M.; Noh, H. J.; Lo, P. K.; Park, H.; Lukin, M. D. Nanometre-scale thermometry in a living cell. *Nature* **2013**, *500*, 54–58.

(24) Lovchinsky, I.; Sushkov, A. O.; Urbach, E.; de Leon, N. P.; Choi, S.; De Greve, K.; Evans, R.; Gertner, R.; Bersin, E.; Müller, C.; McGuinness, L.; Jelezko, F.; Walsworth, R. L.; Park, H.; Lukin, M. D. Nuclear magnetic resonance detection and spectroscopy of single proteins using quantum logic. *Science* **2016**, *351*, 836–841.

(25) Ermakova, A.; Pramanik, G.; Cai, J.-M.; Algara-Siller, G.; Kaiser, U.; Weil, T.; Tzeng, Y.-K.; Chang, H. C.; McGuinness, L. P.; Plenio, M. B.; Naydenov, B.; Jelezko, F. Detection of a Few Metallo-Protein Molecules Using Color Centers in Nanodiamonds. *Nano Lett.* **2013**, *13*, 3305–3309.

(26) Barry, J. F.; Turner, M. J.; Schloss, J. M.; Glenn, D. R.; Song, Y.; Lukin, M. D.; Park, H.; Walsworth, R. L. Optical magnetic detection of single-neuron action potentials using quantum defects in diamond. *Proc. Natl. Acad. Sci. U. S. A.* **2016**, *113*, 14133–14138.

(27) Chen, B.; Xiang, S.; Qian, G. Metal-Organic Frameworks with Functional Pores for Recognition of Small Molecules. *Acc. Chem. Res.* **2010**, *43*, 1115–1124.

(28) Wolfowicz, G.; Tyryshkin, A. M.; George, R. E.; Riemann, H.; Abrosimov, N. V.; Becker, P.; Pohl, H.-J.; Thewalt, M. L. W.; Lyon, S. A.; Morton, J. J. L. Atomic clock transitions in silicon-based spin qubits. *Nat. Nanotech.* **2013**, *8*, 561–564.

(29) Shiddiq, M.; Komijani, D.; Duan, Y.; Gaita-Ariño, A.; Coronado, E.; Hill, S. Enhancing coherence in molecular spin qubits via atomic clock transitions. *Nature* **2016**, *531*, 348–351.

(30) *CRC Handbook of Chemistry and Physics*, 97th Ed.; Haynes, W. M., Ed.; CRC Press: Boca Raton, FL, 2016; Section 11-2.

Michael Graham

Northwestern University, Department of Chemistry
2145 Sheridan Road, Evanston, IL, 60208

EDUCATION

Northwestern University, Evanston, IL August 2017
PhD in Chemistry, GPA: 3.97

Harvard University, Cambridge, MA March 2011
A.B. Magna Cum Laude with High Honors in Chemistry, GPA: 3.75

RESEARCH EXPERIENCE

Northwestern University, Evanston, IL 2012 – 2017
Advisor: *Assistant Prof. Danna Freedman*

- Established the quantum computation subgroup within the Freedman group, published the first journal article within the subgroup, and taught the scientific underpinnings of research in the subgroup to all subsequent members.
- Initiated and led weekly discussion-based quantum computation subgroup meetings.
- Maintained and repaired multiple lab instruments including a SQUID magnetometer and a solvent purification system for 4 years.
- Synthesized novel air- and moisture-sensitive coordination complexes and characterized their suitability for quantum computation via electron paramagnetic resonance spectroscopy.
- Wrote 1 national lab proposal (accepted) and assisted in writing and editing 4 research grant proposals, of which 1 was funded (\$600,000) and 1 is pending.
- Mentored 4 undergraduate researchers and 1 graduate student researcher.
- Collaborated with condensed matter physicists to understand the decoherence properties of synthesized qubit species.

Physical Sciences Inc., Andover, MA 2007 – 2011

- Coordinated with supervisors and coworkers to define research directions and ensure project completion within budget and on schedule.
- Developed microencapsulated chemiluminescent tagging agent for battlefield applications.
- Synthesized hybrid polymer/metal-organic framework water desalination membranes.
- Optimized formulation of lithium-ion battery cathodes and tested their performance.

Harvard University, Cambridge, MA 2008 – 2011
Advisor: *Prof. Tobias Ritter*

- Synthesized air-, moisture-, and temperature-sensitive organometallic molecular wires for applications as switchable conductors.
- Characterized the chains by X-ray crystallography, UV-vis spectroscopy, and DOSY-NMR.

PUBLICATIONS

9. **Graham, M. J.**; Krzyaniak, M. D.; Wasielewski, M. R.; Freedman, D. E. Probing Nuclear Spin Effects on Electronic Spin Coherence via EPR Measurements of Vanadium (IV) Complexes. *Inorg. Chem.* **2017**, DOI: 10.1021/acs.inorgchem.7b00794.
8. **Graham, M. J.**; Zadrozny, J. M.; Fataftah, M. S.; Freedman, D. E. Forging Solid-State Qubit Design Principles in a Molecular Furnace. *Chem. Mater.* **2017**, *29*, 1885–1897.
7. **Graham, M. J.**; Yu, C.-J.; Krzyaniak, M. D.; Wasielewski, M. R.; Freedman, D. E. Synthetic Approach to Determine the Effect of Nuclear Spin Distance on Electronic Spin Decoherence. *J. Am. Chem. Soc.* **2017**, *139*, 3196–3201.
6. Yu, C.-J.; **Graham, M. J.**; Zadrozny, J. M.; Niklas, J.; Krzyaniak, M. D.; Wasielewski, M. R.; Poluektov, O. G.; Freedman, D. E. Long Coherence Times in Nuclear Spin-Free Vanadyl Qubits. *J. Am. Chem. Soc.* 2016, *138*, 14678–14685.
5. Johnson, B. J.; Antholine, W. E.; Lindeman, S. V.; **Graham, M. J.**; Mankad, N. P. A 1-hole Cu₄S Cluster with N₂O Reductase Activity: A Structural and Functional Model for CuZ*. *J. Am. Chem. Soc.* 2016, *138*, 13107–13110.
4. Zadrozny, J. M.; **Graham, M. J.**; Krzyaniak, M. D.; Wasielewski, M. R.; Freedman, D. E. Unexpected Suppression of Spin-Lattice Relaxation via High Magnetic Field in a High-Spin Iron(III) Complex. *Chem. Commun.* 2016, *52*, 10175–10178.
3. Fataftah, M. S.; Zadrozny, J. M.; Coste, S. C.; **Graham, M. J.**; Rogers, D. M.; Freedman, D. E. Employing Forbidden Transitions as Qubits in a Nuclear Spin-Free Chromium Complex. *J. Am. Chem. Soc.* 2016, *138*, 1344–1348.
2. **Graham, M. J.**; Zadrozny, J. M.; Shiddiq, M.; Anderson, J. S.; Fataftah, M. S.; Hill, S.; Freedman, D. E. Influence of Electronic Spin and Spin-Orbit Coupling on Decoherence in Mononuclear Transition Metal Complexes. *J. Am. Chem. Soc.*, 2014, *136*, 7623–7626.
***JACS Article Spotlight on this work:** *J. Am. Chem. Soc.*, 2014, *136*, 7783–7784.
1. Campbell, M. G.; Powers, D. C.; Raynaud, J.; **Graham, M. J.**; Xie, P.; Lee, E.; Ritter, T. Synthesis and Structure of Solution-Stable One-Dimensional Palladium Wires. *Nature Chem.* 2011, *3*, 949–953.

PRESENTATIONS

- Gordon Research Seminar/Conference: Inorganic Chemistry, Biddeford, ME 2016
Poster presentation
- Northwestern BIP Inorganic Seminar Series, Evanston, IL 2014, 2015, 2016
Three oral presentations

American Chemical Society Fall Meeting, Boston, MA 130
2015
Two oral presentations

Chicago Regional Inorganic Colloquium, Chicago, IL 2014, 2015
Two poster presentations

HONORS AND AWARDS

American Chemical Society Inorganic Division Student Travel Award (\$450) 2015
Selective award to enable travel to ACS conference to deliver an oral presentation.

National Science Foundation Graduate Research Fellowship (\$102,000) 2014
Prestigious, nationally competitive 5-year fellowship which provides full funding of graduate study.

Northwestern University Ryan Fellowship (\$15,000) 2011
Highly selective 2-year fellowship dedicated to the study of fundamental nanoscale science.

TEACHING EXPERIENCE

General Chemistry Course Teaching Assistant 2012 – 2013
Northwestern University, Evanston, IL

- Served as one of three “Super TAs” for Chemistry 101 (two quarters, 400+ students each quarter) and one of two for Chemistry 103 (one quarter, 200+ students).
- Wrote homework, quizzes, and exams; tutored students one-on-one during office hours and via email; and delivered weekly review lectures for each course.
- Earned student ratings of 5.1/6.0 (Chem 101, 2012), 5.0/6.0 (Chem 101, 2013), and 5.0/6.0 (Chem 103, 2013).

General Chemistry Laboratory Teaching Assistant 2013
Northwestern University, Evanston, IL

- Supervised 30 students during laboratory section, answered questions, and graded lab reports.
- Earned student ratings of 2.83/3.00.

SCIENCE OUTREACH

BIP Seminar Series Coordinator 2015 – 2016
Northwestern University, Evanston, IL

- Led a weekly inorganic-focused departmental seminar series focused on the work of graduate students and post-doctoral scholars for one year.
- Increased seminar attendance by 10% over previous year by obtaining departmental funding for food and coffee. Worked with co-coordinator to enlist speakers, arrange logistics and focus discussion.

Science Club Mentor

2013 – 2014

McCormick Boys and Girls Club, Chicago, IL

- Mentored 4 middle school students in planning, implementing, and drawing conclusions from projects in an afterschool science enrichment program focused on minority and impoverished students.

Lincolnwood Afterschool Science Program

2012

Lincolnwood Elementary School, Evanston, IL

- Taught miniature science lessons to elementary school students in a weekly afterschool program.

PROFESSIONAL MEMBERSHIPS

American Chemical Society

2015 – Present

PROFICIENCY AND SKILLS

Synthesis: Air-free techniques; inert-atmosphere glovebox;* organic, solid-state, and hydrothermal synthesis

Spectroscopy: NMR, EPR,* UV-vis, IR, Raman, nuclear resonant vibrational spectroscopy (NRVS)

Other techniques: SQUID magnetometry,* X-ray diffractometry (powder and single-crystal), mass spectrometry, cyclic voltammetry, scanning electron microscopy, solvent purification system*

Software: Microsoft Office Suite, Origin, Matlab, ChemDraw, Mendeley, CSD Suite, SciFinder, Reaxys

Language: Spanish (limited working proficiency)

*Maintained and/or trained others on these instruments